

Electronic Transport in 2D Materials with Strong Spin-orbit Coupling

THÈSE N° 7390 (2017)

PRÉSENTÉE LE 10 MARS 2017

À LA FACULTÉ SCIENCES DE BASE

CHAIRE DE PHYSIQUE NUMÉRIQUE DE LA MATIÈRE CONDENSÉE

PROGRAMME DOCTORAL EN PHYSIQUE

ÉCOLE POLYTECHNIQUE FÉDÉRALE DE LAUSANNE

POUR L'OBTENTION DU GRADE DE DOCTEUR ÈS SCIENCES

PAR

Artem PULKIN

acceptée sur proposition du jury:

Prof. R. Houdré, président du jury
Prof. O. Yazyev, directeur de thèse
Dr J. Fernández-Rossier, rapporteur
Prof. J. Fabian, rapporteur
Prof. A. Kis, rapporteur



ÉCOLE POLYTECHNIQUE
FÉDÉRALE DE LAUSANNE

Suisse
2017

Abstract

The thesis describes the computational study of structural, electronic and transport properties of monolayer transition metal dichalcogenides (TMDs) in the stable 2H and the metastable 1T' phases. Several aspects have been covered by the study including the electronic properties of the topological quantum spin Hall (QSH) state in the 1T' monolayer phase as well as the effects of strain, periodic line defects, interfaces and edges of monolayer TMDs. The electronic properties of the bulk monolayer phases were described by the *ab-initio* density functional theory (DFT) framework while the electronic and transport properties of 1D defects were calculated using the non-equilibrium Green's function (NEGF) formalism and its extensions. A specific focus was made on the transport of spin-polarized charge carriers across line defects in the monolayer 2H phase. Subject to energy, pseudomomentum and spin conservation, the size of the transport gap is governed by both bulk properties of a material and symmetries of a line defect. Outside the transport gap energy region, the charge carriers are discriminated with respect to their spin resulting in the spin polarization of the transmitted current.

Next, the properties of the metastable monolayer 1T' phase, its edges and interfaces with the 2H structural phase were studied. The presence of a sufficiently large band gap is important for the observation of the QSH phase in the family of materials by probing the topologically protected boundary states. The meV-order band gaps of the 1T' phase of monolayer TMDs were found to be sensitive to materials' lattice constants suggesting the control of the band gap size by strain. In particular, the electronic band structure and the size of the band gap in monolayer 1T'-WSe₂ were found to be in agreement with experimental spectroscopy studies. The topologically protected states at the edges of the monolayer 1T' phase as well as at the boundaries between the topological 1T' phase and the trivial 2H phase of monolayer TMDs were studied. The dispersion of edge bands depends on the atomic structure of the boundary/termination. Specific atomic structure configurations were suggested to observe experimentally the topological protection of the charge carrier transport against back-scattering.

Finally, in the context of lateral semiconducting device engineering, the electronic and transverse transport properties of phase boundaries between the 2H and the 1T' phases as well as the dimerization defects in the 1T' phase were investigated. Both kinds of defects considered exhibit a relatively large transmission probability for the charge carriers crossing the defects. However, the differences between the shapes of bulk bands of the two phases open a sizeable transport gap for charge carriers crossing periodic domain boundaries between the monolayer 2H and 1T' phases. The calculated formation energies of dimerization defects were found to be relatively low suggesting their high concentration in real samples of monolayer 1T'-TMDs.

Additionally, the thesis includes studies of magnetic dopants on the surface of Bi_2Te_3 and atomic vacancies in monolayer 2H-MoSe₂ where the electronic properties of point defects were calculated and compared to experimental results. The two possible adsorption sites of Fe on the surface of Bi_2Te_3 both show a large out-of-plane magnetic anisotropy in agreement with experiments. The calculated local electronic properties of Se vacancies in monolayer 2H-MoSe₂ show the presence of in-gap states which are not observed in experiment. Nevertheless, the combination of theoretical and experimental scanning tunneling microscopy images allowed the unambiguous identification of the vacancy defect.

Keywords: 2D materials, transition metal dichalcogenides, TMDs, line defects, domain boundaries, spin-orbit coupling, density functional theory, ballistic transport, non-equilibrium Green's function, NEGF, spin current, quantum spin Hall effect, QSH, topological insulators.

Résumé

Cette thèse décrit l'étude computationnelle des propriétés structurales, électroniques et de transport des dichalcogénures de métaux de transition (TMDs) monocouches, tant dans la phase stable 2H que dans la phase métastable 1T'. Plusieurs aspects ont été couverts en étudiant les propriétés électroniques dans l'état topologique de l'effet Hall quantique de spin (QSH) dans la phase 1T' monocouche, ainsi que l'effet de la pression, de défauts de ligne périodiques, d'interfaces et d'effets de bord. Les propriétés électroniques des phases immaculées ont été décrites par la théorie *ab-initio* de la fonctionnelle de la densité (DFT), alors que les propriétés électroniques et de transport des défauts 1D ont été calculées à l'aide du formalisme des fonctions de Green hors équilibre (NEGF) et ses extensions.

Une attention particulière a été portée au transport de porteurs de charge polarisés de spin au travers de défauts de ligne dans la phase 2H monocouche. Sujette à la conservation de l'énergie, du pseudo-moment et du spin, la taille du gap de transport est gouvernée à la fois par les propriétés de la phase immaculée que par les symétries du défaut de ligne. En-dehors de la région d'énergie du gap de transport, les porteurs de charge sont discriminés par rapport à leur spin, résultant en une polarisation de spin du courant transmis.

Ensuite, les propriétés de la phase métastable 1T', ses bords et interfaces avec la phase structurale 2H ont été étudiées. La présence d'une bande interdite suffisamment large est importante pour l'observation de la phase QSH dans cette famille de matériaux en sondant les états de bord topologiquement protégés. Les bandes interdites de l'ordre de quelques meV de la phase 1T' des TMDs monocouches se sont révélés être sensibles aux constantes de réseau des matériaux, suggérant un contrôle de la taille de la bande interdite par des effets de pression. En particulier, la structure de bandes électronique et la taille de la bande interdite dans la monocouche du matériau 1T'-WSe₂ calculés sont en bonne correspondance avec des études expérimentales de spectroscopie. Les états topologiquement protégés localisés sur les bords dans la phase 1T' monocouche, ainsi qu'à l'interface avec la phase triviale 2H, ont été étudiés. La dispersion des bandes de bord dépend de la structure atomique à la terminaison et l'interface, respectivement. Des configurations atomiques spécifiques ont été suggérées afin d'observer expérimentalement la protection topologique des porteurs de charge contre la rétrodiffusion.

Finalement, dans le contexte d'ingénierie de dispositif latéraux semi-conducteurs, les propriétés électroniques et de transport de frontières entre les phases 2H et 1T', ainsi que des effets de défaut de dimérisation dans la phase 1T', ont été étudiées. Les deux types de défaut considérés ont révélé comporter une haute probabilité de transmission pour les porteurs de charge à

travers les défauts. Cependant, les différences entre les formes des bandes dans les deux phases ouvre un gap de transport de taille pour les porteurs de charge traversant les frontières de phase périodiques entre les phases 2H et 1T' monocouches. Les énergies de formation calculées des défauts de dimérisation se sont révélées relativement petites, suggérant une forte concentration dans des échantillons réels de monocouches de TMDs dans la phase 1T'. En plus, cette thèse comporte des études de dopants magnétiques sur la surface du Bi_2Te_3 et de vacances atomiques dans le 2H-MoS₂ monocouche, où les propriétés de défauts ponctuels ont été calculées et comparées avec des résultats expérimentaux. Les deux sites d'absorption possible du Fe sur la surface de Bi_2Te_3 révèlent une forte anisotropie magnétique hors du plan, en accord avec les expériences. Les propriétés électroniques locales de vacance de Se dans le 2H-MoS₂ monocouche révèlent la présence d'états dans la bande interdite qui ne sont pas observés expérimentalement. Néanmoins, la combinaison théorique et expérimentale d'images de microscopie à effet tunnel ont permis une identification non-ambiguë de la vacance.

Mot clés : matériaux 2D, dichalcogénures de métaux de transition, TMDs, défauts de ligne, limites de domaines, couplage spin-orbite, théorie de la fonctionnelle de la densité, transport ballistique, fonctions de Green hors équilibre, NEGF, effet Hall quantique de spin, QSH, isolants topologiques.

Contents

Abstract (English/Français)	i
List of figures	vii
List of tables	ix
1 Introduction	1
1.1 Modern electronics: successes and problems	1
1.2 Electron spin	2
1.3 Novel materials for applications in electronics	4
1.3.1 2D materials	5
1.3.2 Topological insulators	7
1.3.3 Defects in materials	11
1.3.4 Charge carrier transport in solid state	13
2 Methodology	17
2.1 Density functional theory (DFT)	17
2.1.1 Kohn-Sham equations	17
2.1.2 Limitations of DFT	18
2.1.3 DFT in crystals, the Bloch theorem and the Brillouin zone	19
2.1.4 Core electrons and pseudopotentials	23
2.1.5 Electron spin and spin-orbit coupling in DFT	24
2.1.6 Single-electron basis in DFT	26
2.2 Ballistic transport at nanoscale with DFT	28
2.2.1 Green's function formalism	29
2.2.2 Transport of electron spin	44
2.2.3 Optimizing computational costs with the Green's function method	45
2.3 Simulating scanning tunneling microscopy (STM) images	47
3 Spin and valley transport across regular line defects in semiconducting TMDs	51
3.1 Bulk properties of monolayer 2H-TMDs	52
3.2 Line defects in monolayer 2H-MoS ₂ and other TMDs	55
3.3 Ballistic transport across periodic line defects in a monolayer 2H-MoS ₂	57
3.3.1 The transport gap	57

Contents

3.3.2	Transport simulations and the spin polarization of charge carrier current	60
3.4	Ballistic transport across inversion domain boundary in monolayer 2H-MoSe ₂	63
3.5	Conclusions	65
4	Electronic properties of the distorted 1T structural phase in monolayer TMDs	67
4.1	Bulk properties of the monolayer 1T' phase	68
4.1.1	Electronic structure properties of monolayer 1T'-WSe ₂	70
4.1.2	Properties of monolayer 1T'-TMDs under strain	72
4.1.3	Summary	76
4.2	Edges of monolayer 1T'-TMDs	77
4.2.1	Summary	80
4.3	Electronic properties of structural phase boundaries in monolayer WSe ₂	81
4.3.1	Summary	85
4.4	Electronic properties of dimerization defects in monolayer 1T'-WSe ₂	86
4.4.1	Summary	89
4.5	Conclusions	90
5	Simulating STM images of point defects in spin-orbit systems	91
5.1	Magnetic adatoms on the surface of Bi ₂ Te ₃	91
5.1.1	Thermodynamical properties of adatoms	93
5.1.2	Electronic and magnetic properties of adatoms	93
5.1.3	Conclusions	95
5.2	Selenium vacancies in monolayer 2H-MoSe ₂	95
5.2.1	Electronic properties of Se vacancies	97
5.2.2	Conclusions	97
6	Outlook	101
A	Appendix	103
A.1	On left and right eigenvalues	103
A.2	Valley filtering with line defects	104
A.3	Simulation details: charge carrier transport in monolayer 2H-MoS ₂	106
A.4	Simulation details: spin polarization of the transmission probability in monolayer 2H-MoS ₂	107
A.5	Projected band structure in MoS ₂ and other TMDs	110
A.6	Simulation details: periodic zigzag terminations of monolayer 1T'-TMDs	112
A.7	Local densities of states at the zigzag terminations of monolayer 1T'-TMDs	113
A.8	Simulation details: Fe adatoms on the surface of Bi ₂ Te ₃	113
A.9	Simulation details: point defects in MoSe ₂	113
	Bibliography	124
	Curriculum Vitae	125

List of Figures

1.1	An example of an integrated circuit: TL431 voltage regulator	3
1.2	A next-generation integrated circuit prepared from a bilayer MoS_2	4
1.3	Atomic and electronic structures of 2D materials	6
1.4	Representatives of 2D materials	7
1.5	Band structures of the quantum spin Hall phase and the topologically trivial phase of the Kane-Mele model	8
1.6	Torus enclosing the origin point (black) as an illustration to topologically non-trivial Bloch Hamiltonian	10
1.7	Models of line defects in MoS_2	13
1.8	Defects observed in MoS_2	14
2.1	The periodic reciprocal space for a 2D hexagonal lattice	22
2.2	A sketch of a pseudopotential used in density functional theory simulations . .	25
2.3	A schematic illustration of a two-terminal ballistic transport setup	28
2.4	Ideal and defective 2D systems	30
2.5	Structure of a nanowire device Hamiltonian	32
2.6	Boundary conditions and unknown amplitudes in the transport setup	36
2.7	A supercell model for the transport calculations	46
3.1	The crystal structure and symmetries of monolayer 2H-TMDs	53
3.2	Electronic band structures of 6 2D TMDs. The electronic band gap E_g and the largest spin-orbit splitting in the valence band Δ are indicated in each case. . .	54
3.3	Fermi surfaces in monolayer 2H- MoS_2	55
3.4	Atomic structures of periodic line defects in monolayer 2H- MoS_2	56
3.5	The transport gap in a monolayer 2H- MoS_2	58
3.6	A schematic illustration of bulk states of a monolayer 2H- MoS_2 in the leads projected onto the 1D BZ of the defect	59
3.7	Transport properties across line defects in monolayer 2H- MoS_2	61
3.8	The single-particle Hartree potential of monolayer 2H- MoS_2 defects	62
3.9	Atomic microscopy images of defective monolayer 2H- MoSe_2	64
3.10	Electronic and transport properties of an inversion domain boundary in MoSe_2 .	64
4.1	Structural phases of 2D TMDs: 2H, 1T and 1T'	68
4.2	Electronic band structures of monolayer 1T'-TMDs	69

List of Figures

4.3	Electron and hole pockets in semimetallic monolayer 1T'-TMDs	70
4.4	Experimental observation of the monolayer 1T' phase in WSe ₂	71
4.5	Evolution of the electronic properties of monolayer 1T'-TMDs upon the change of lattice parameters	74
4.6	The location of the conduction band minimum (CBM) in the Brillouin zone of monolayer 1T'-TMDs as a function of lattice parameters	75
4.7	The topological invariant phase in strained monolayer 1T'-TMDs	76
4.8	Atomic structures of zigzag terminations in monolayer 1T'-TMDs and their formation energies	78
4.9	The k -resolved density of states localized at the energetically preferred zigzag terminations of monolayer 1T'-TMDs	79
4.10	Momentum-resolved localized density of electronic states of zigzag terminations suitable for the protected charge carrier ballistic transport experiment	80
4.11	Atomic structures of the 2H-1T' phase boundaries along the zigzag direction of monolayer WSe ₂	82
4.12	Electronic structure of phase boundaries in monolayer WSe ₂	83
4.13	Charge carrier transmission function of the 2H-1T' phase boundaries in monolayer WSe ₂	85
4.14	Relative transmissions of phase boundaries in WSe ₂	86
4.15	Atomic structures of 1T' periodic dimerization defects in monolayer WSe ₂ . . .	87
4.16	Electronic structure properties of dimerization defects in monolayer 1T'-WSe ₂ .	89
5.1	Fe dopants on the surface of Bi ₂ Te ₃	92
5.2	Electronic properties of Fe adatoms on the surface of Bi ₂ Te ₃	94
5.3	Atomic structure and electronic properties of point defects in monolayer 2H-MoSe ₂	96
5.4	Density of electronic states for the selenium vacancy defect in monolayer 2H-MoSe ₂	98
5.5	STM images of the selenium vacancy in monolayer 2H-MoSe ₂ : theory vs experiment	99
A.1	A mirror-symmetric line defect in graphene	105
A.2	An illustration of Fermi surfaces, branches and bulk states used in the calculation of angle-dependent properties	109
A.3	The local density of states of the six zigzag terminations presented in Fig. 4.8 . .	114

List of Tables

2.1	Basis sets: pros and cons	27
3.1	Equilibrium lattice parameters a and h of monolayer 2H-TMDs (PBE-DFT level of theory).	52
4.1	Properties of a band gap in monolayer 1T'-TMDs	69
4.2	The magnitude of the transport gap for charge carriers propagating across phase boundaries in monolayer WSe ₂	84
4.3	Formation energies of dimerization defects in monolayer 1T'-WSe ₂	88
5.1	Magnetic properties of Fe adatoms on the surface of Bi ₂ Te ₃ : magnetic moments and anisotropies calculated by projecting occupied Bloch states onto atomic orbitals.	95

1 Introduction

1.1 Modern electronics: successes and problems

Advances in modern technology are sometimes associated with the development of electronic devices. They are built of electric circuits where currents serve a particular purpose: supply a power for mechanical motion, light sources, heaters, etc. In the digital era a very simple idea was developed: an electric current may carry information. The information is simply encoded in the fact of the presence of the current: [switch is on = current flows = the bulb is lighted = 1] versus [switch is off = no current = the bulb is not lighted = 0]. The transfer of information requires constantly switching circuits on and off done by electronic logic devices. Higher switching speeds are reached by minimizing the power consumption of devices. The most straightforward way to do it is to reduce the device size increasing resistances and reducing currents according to Ohm's law,

$$\text{Resistance} \sim \frac{\text{device length}}{\text{section area}}.$$

Such approach and above law work well for 'classical' devices larger than several nanometers (nm, $1 \text{ nm} = 10^{-9} \text{ m}$) where electron is a classical particle (ball) having position and velocity. At the time of writing this thesis (2016) this approach is almost depleted: the most advanced consumer devices hit a feature size of 14 nm[1]. Thus, qualitatively new developments with deeper understanding of electron properties are demanded.

Soon after discovering the electron particle (1897) it was realized that it behaves differently in different materials. This led to a concept of an electronic structure of a solid material. Not only the material itself but it's temperature, impurities and defects influence the electronic structure. This fact is widely used in modern silicon electronics where a single material (Si) acts as a conductor (conducts electrons), an insulator (blocks electron transport) and a semiconductor (switchable conductor). An example of a Si-based device is presented in Fig. 1.1. There, different regions of Si have different roles resulting in a rather complicated

device consisting of multiple (up to 10^{10}) blocks.

The bulk Si is, probably, the most studied material so far where the most important electronic structure properties (the band gap magnitude and the charge carrier concentration) can be varied precisely within certain ranges. On the other hand, the Si approaching 1 nm thickness (or atomically thin Si) demonstrates completely different electronic properties[2] because electrons become extremely confined along one of the dimensions. Thus, to be able to compete with Si an insight is required into material properties in 2D.

While novel materials promise quantitative performance boost, the qualitative changes are preferred. The last breakthrough in this field happened in 1947 with the invention of a solid-state transistor[4] used till now. Researchers, however, discuss various possibilities to operate information by using light or electron spin. This would not only raise existing performance limits but also re-think of what information actually is: from binary representation (on/off) one would have a quantum *superposition* of “on” and “off” states. Thus, existing algorithmic problems can be solved in a completely different manner commonly referred to as “quantum computing”. The basic building block of a quantum computer, electron spin, is introduced in the following chapter.

1.2 Electron spin

While it is a well-known fact for the general public that an electron carries the electric charge, it is a little bit less known about what electron spin is. Conventionally, spin is presented as an arrow attached to electron and pointing upward or downward. Unlike charge, spin is an additional degree of freedom of elementary particles: it creates a magnetic moment, thus, it can be changed by magnetic field. A rigid definition is given in Ref. [5], for example:

Spin is an intrinsic form of angular momentum (vector) carried by elementary particles, composite particles (hadrons), and atomic nuclei.

The size of the spin is the same across all particles of a given kind. Thus, elementary particles are classified by the magnitude of spin: fermions have half-integer spins ($1/2$ for electron) while integer values of spin are attributed to bosons (1 for a photon). Fermions and bosons have fundamentally different properties in terms of particle statistics and commutation relations in quantum physics.

The most intriguing fact about spin is that it cannot be measured completely: quantum mechanics prohibits such experiment. It is possible to project the spin onto arbitrary direction and obtain its value ($+1/2$ or $-1/2$ for electron) with a well-defined quantum mechanical probability. Such measurement necessarily changes the spin and destroys the initial quantum mechanical state of an electron. This fact is widely used in quantum cryptography providing a way to track eavesdropping.

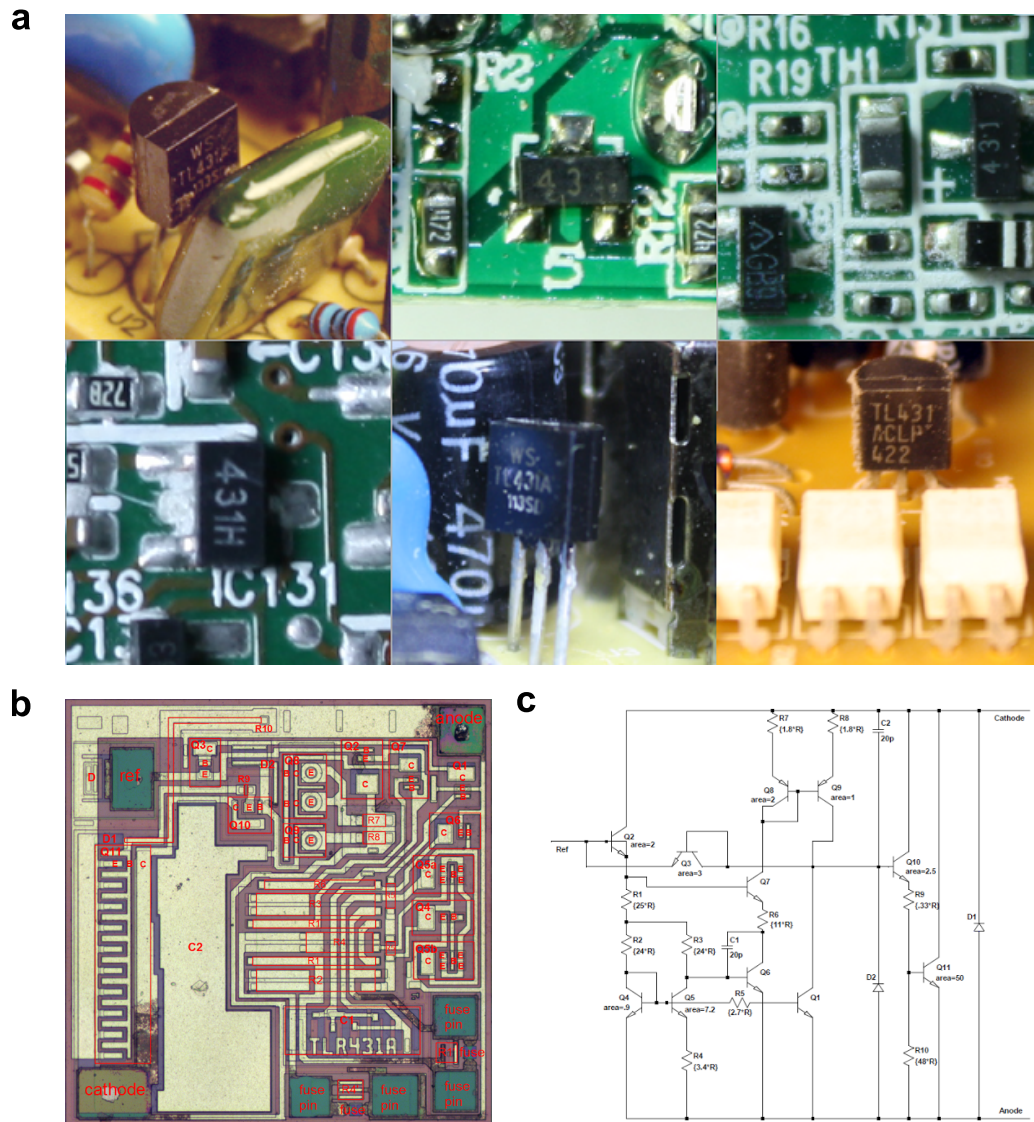


Figure 1.1 – An example of an integrated circuit (IC): TL431 voltage regulator. (a) Photographs of IC inside a package as it appears in consumer electronic devices reproduced with permission from Ref. [3]. (b) IC under microscope. The different tones of pink/purple denote silicon with different doping. The light colors correspond to metallic coating acting as connector wires. The red labels specify basic building blocks of an IC: resistors, capacitors and transistors. (c) An equivalent scheme of the TL431 with the corresponding elements from (b).

As it is evident from the above, the idea of a spin (or, more general, a quantum mechanical state) carrying information attracted a lot of attention and evolved into quantum computing[6]. There, primitive data types (integers, floats) and operations (sums, products) are replaced by vectors and linear operators. Interestingly, quantum informatics already has its own applications without any proof of a sizeable “quantum computer” have been built. For example,

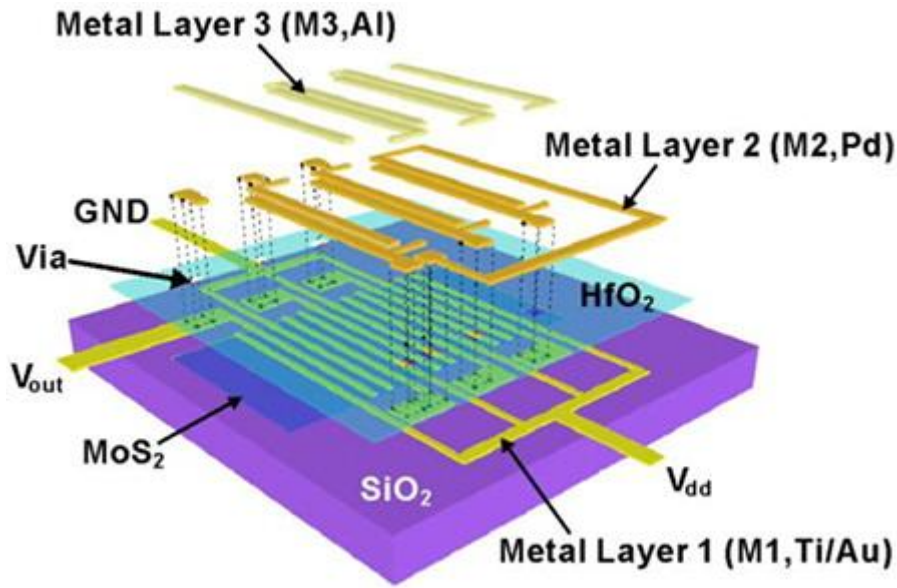


Figure 1.2 – A next-generation integrated circuit prepared from a bilayer MoS_2 . The charge carrier channel thickness approaches 1 nm. The image is reproduced with permission from Ref. [8].

the Shor's algorithm for factorization of numbers[7] demonstrated weaknesses of existing cryptographic protocols and stimulated development of different algorithms.

The spin is being used in conventional electronics since 1951: the information stored on magnetic tapes, floppy disks and hard disc drives is essentially a macroscopic magnetization formed by electron spins. From the performance point of view it is more efficient to use a single spin instead of magnetization. To be able to operate spin by all-electric means under normal conditions suitable materials are desired.

1.3 Novel materials for applications in electronics

There is no simple answer to the question whether 2D or any other novel material are *better* than the well-established silicon framework for electronics applications. It has been pointed out, however, that Si is used to the maximum of its possibilities, thus, it has to be replaced by another material. 2D materials are promising candidates which can be prepared relatively easily and stacked on top of each other to form an electronic device (Fig. 1.2) similarly to existing industrial protocols for Si.

1.3.1 2D materials

The term “2D material” was introduced in 2005[9] and now approximately 100 materials are known to exist in 2D. Graphene is the first material isolated from its bulk counterpart (graphite) by Novoselov and Geim in 2004 (Nobel prize in physics 2010) using the Scotch tape exfoliation[10]. Graphene is also similar to other 2D materials from multiple perspectives so it is worth reviewing it briefly.

Graphene is formed by carbon atoms arranged into a hexagonal lattice, Fig. 1.3(a). In graphite the 2D graphene flakes interact weakly by Van der Waals forces. In contrast, the in-plane sp^2 bonding between carbon atoms is stronger than sp^3 in diamond making graphene one of the most stable materials so far.

The charge carriers in 2D materials and, particularly, graphene are confined to the material plane. The fundamental interest in graphene is due to its electronic properties: the low-energy charge carriers in graphene have a linear dispersion law:

$$E(\vec{k}) = \pm \hbar k v_F ,$$

where E is the charge carrier energy, \vec{k} is the wave vector of a charge carrier and v_F is a material constant (Fermi velocity). This has several important consequences. First, graphene is a semimetal: it has no band gap but the density of electronic states at the Fermi level vanishes[11]. Second, the charge carriers in graphene behave similarly to photons, the light particles. They travel with no mass at a constant speed (group velocity) v_F . The particles sharing such property are referred to as massless Dirac fermions: in graphene they are located at K and K' valleys of the hexagonal Brillouin zone forming two “Dirac cones” in the electronic band structure Fig. 1.3(b). Being convenient to study, graphene demonstrates a number of unique properties and presents interest for fundamental research. On the other hand, graphene faces criticism with regard to its applications in electronics: it is a semimetal with no sizeable band gap possible. Thus, electron transport in graphene cannot be switched off completely which is a major difficulty for constructing a logic device. Nevertheless, the discovery of graphene gave rise to interest in other *layered* materials which may be exfoliated similarly.

Molybdenum disulfide (MoS_2) is one of the materials where monolayers can be produced by similar exfoliation techniques[12]. Both MoS_2 and graphene are hexagonal materials though the atoms in MoS_2 are arranged into 3 parallel planes, Fig. 1.3(c). Unlike graphene, MoS_2 is a semiconductor with a band gap of around 2 eV[13] and is readily suitable for devices[14, 15, 8]. The direct band gap in MoS_2 is located at K and K' valleys as schematically illustrated in Fig. 1.3(d) which builds one more parallel with graphene. Unlike in graphene, though, the spin degeneracy in non-centrosymmetric MoS_2 is lifted due to spin-orbit coupling. The hole charge carriers at the top of the valence band in MoS_2 are spin polarized depending on the pseudomomentum (spin-valley coupling in MoS_2 [16]). This interesting feature of an

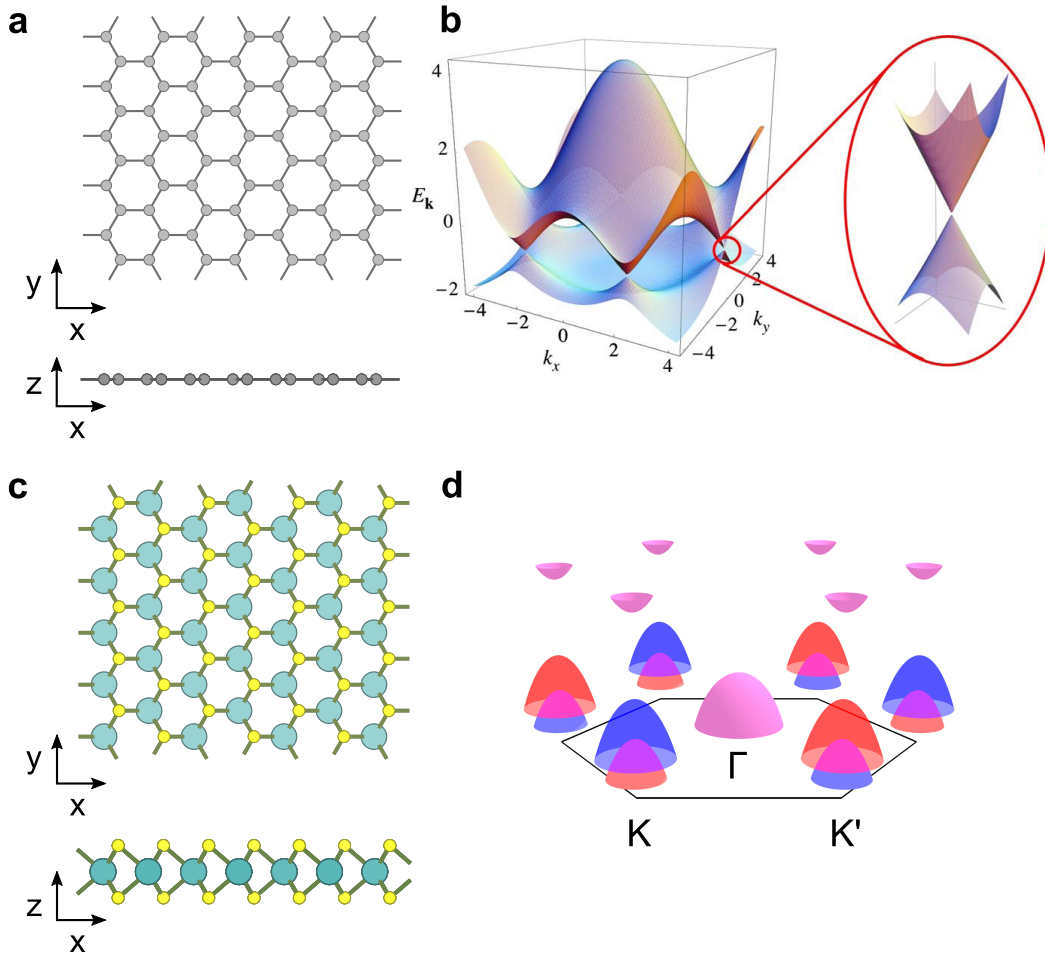


Figure 1.3 – Atomic and electronic structures of 2D materials. (a) Atomic structure of graphene. (b) Electronic band structure of graphene from Ref. [11]. The Dirac cones are located in the corners of the hexagonal Brillouin zone. (c) Atomic structure of a monolayer molybdenum disulfide. (d) Schematic illustration of the electronic band structure of a monolayer MoS_2 . The hexagon represents the Brillouin zone of MoS_2 . The color represents spin polarization of electrons (spin-up blue and spin-down red).

electronic band structure of MoS_2 was confirmed by several optical experiments[17, 18, 19].

More 2D materials can be derived by using elements of the same atomic group. For example, carbon, silicon and germanium belonging to group 14 form graphene, silicene and germanene in Fig. 1.4. Similarly, molybdenum and tungsten from group 6 together with sulfur, selenium and tellurium from group 16 form six transition metal dichalcogenides (TMDs). Inside each group of materials the electronic properties differ mostly quantitatively. Apart from graphene and MoS_2 , many other 2D materials have already been found suitable for electronic devices, for example, WSe_2 [20] and silicene[21]. Further developments in 2D material applications are associated with conceptually new ways to encode information in the charge carrier quantum

1.3. Novel materials for applications in electronics

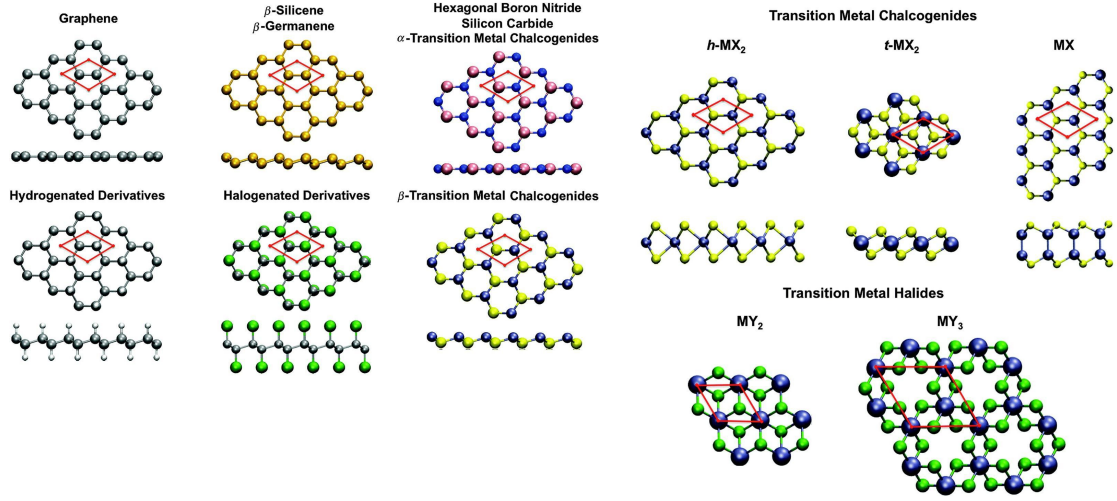


Figure 1.4 – Representatives of 2D materials family reproduced with permission from Ref. [22] including graphene, silicene, germanene, boron nitride, transition metal dichalcogenides and halides and functionalized versions of above. All materials presented here have a hexagonal lattice structure.

numbers such as switching from electron charge to electron spin or valley.

1.3.2 Topological insulators

Massless Dirac fermions and the Dirac cone in the electronic band structure are not particular to graphene. They also appear on surfaces or 2D interfaces of topological insulators[23, 24, 25, 26, 27, 28, 29, 30] (TIs). There are many other reasons to study topological insulators due to unique electronic properties such as protection of surface/interface states, perfect charge carrier transmission along boundaries, spin texture of edge states, Majorana fermions, superconducting effects. The 2016 Nobel Prize in Physics was awarded to David Thouless, Duncan Haldane and Michael Kosterlitz “for theoretical discoveries of topological phase transitions and topological phases of matter”.

As it is evident from the naming, TIs are insulators, i.e. they have a finite positive band gap. Historically, the first topological insulator phase observed was named as the quantum Hall effect (QHE). There, a 2D electronic system subject to low temperatures and high normal magnetic fields demonstrates quantization of the Hall conductance

$$\sigma_{xy} = \frac{I_x}{V_y} = \nu \frac{e^2}{h},$$

where I_x is the current along x direction, V_y is the voltage measured along y direction, e^2/h is the quantum of conductance and ν is an integer often referred to as the Chern number. The topological origin of this quantization was not emphasized until the discovery of the

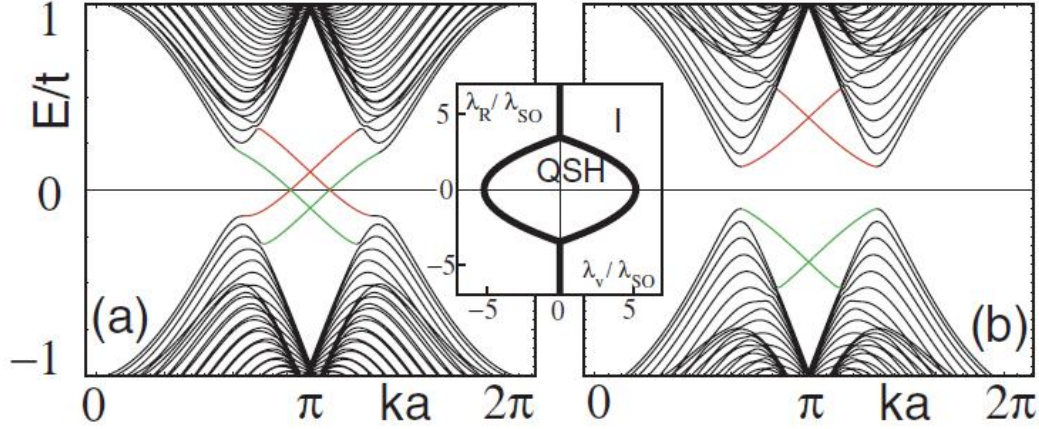


Figure 1.5 – Band structures of the QSH phase (left) and the topologically trivial phase (right) of the Kane-Mele model reproduced with permission from Ref. [23]. The QSH phase (left) hosts gapless states: one per spin and per edge (the model contains 2 edges). In contrast, the trivial phase (right) does not host any in-gap states. The middle inset shows the parameter space of possible phases.

quantum *spin* Hall effect (QSHE) in 2005[23] by Charles Kane and Eugene Mele. Specifically, the authors considered a simple model of graphene with spin-orbit interactions. Depending on the model parameters it has been shown that the system can be driven into two distinct topological phases. In the paper, the authors emphasized the importance of the bulk-boundary correspondence. Particularly, both Chern number in the QHE and the \mathbb{Z}_2 topological index¹ in the QSHE are bulk properties of a material that define the number of *gapless* states localized at the boundary (surface, interface) as illustrated in Fig. 1.5. The detailed considerations show that in the QHE the number of “protected” boundary modes may be arbitrary (i.e. integer Z) whereas QSHE supports 0 or 1 protected boundary modes per electron spin. Unlike any other interface or boundary mode, the existence of “protected” modes is guaranteed by the topology of the bulk electronic structure.

QHE and QSHE have a different physical origin. Nevertheless, both these effects can be viewed as particular cases of a more general problem: topology of the electronic structure of a solid subject to a set of symmetries. As such, the most common physical symmetries (time reversal, particle-hole and chiral) can be combined into a periodic table of topological insulators[31] where for each set of symmetries a topological index (Z , Z_2 or none) is assigned. It is more instructive to show it under a single-particle approximation where a solid is described by Bloch Hamiltonian $H(\mathbf{k})$ in the Brillouin zone. Provided $\{H\}$ is a topological space of Hermitian matrices, the Bloch Hamiltonian $H(\mathbf{k})$ becomes a 1D, 2D or 3D loop. Two Bloch Hamiltonians $H_1(\mathbf{k})$, $H_2(\mathbf{k})$ are *homotopic* if the 2 corresponding loops can be deformed into each other continuously. Homotopy yields equivalence classes in the topological space where all elements

¹ $\mathbb{Z}_2 = \{0, 1\}$ means integer modulo 2

of the same class are topologically equivalent. Thus, it is possible to define a topological invariant (Chern number, \mathbf{Z}_2 index, winding number, etc.) which is same for topologically equivalent Hamiltonians and different for inequivalent ones. The number of classes roughly characterizes the topological space: for example, only two classes exist for QSH Hamiltonians: a trivial one and a non-trivial one. Conventionally, all Hamiltonians similar to the vacuum² are assigned a trivial class.

As an instructive example of the topological characterization of Bloch Hamiltonians consider a two-band tight-binding model. The most general way to write it is to use Pauli matrices $\sigma_{x,y,z}$:

$$\mathbf{H}(\vec{k}) = E_0(\vec{k}) + \sum_{i=x,y,z} h_i(\vec{k}) \cdot \sigma_i. \quad (1.1)$$

For simplicity, let's assume that the energy origin $E_0(\vec{k}) = 0$. With this condition it becomes possible to perform a one-to-one mapping of a 2x2 Hermitian matrix $\mathbf{H}(\vec{k})$ onto the 3D space where each point has real coordinates $\{h_i\}$. The two eigenvalues of the matrix are simply distances from the origin to a particular point:

$$E(\vec{k}) = \pm \sqrt{h_x^2(\vec{k}) + h_y^2(\vec{k}) + h_z^2(\vec{k})} \quad (1.2)$$

At this point one usually states the intention to characterize topology of *gapped* Hamiltonians. Here, we assume that the system has a single electron per unit cell, thus, out of the two bands $E_{1,2}(\vec{k})$ only one is occupied. Without any loss of generality, the Fermi level is set at zero. All of the above is expressed in a single condition $E(\vec{k}) \neq 0$ for any \vec{k} . It excludes origin from the mapped 3D space.

Provided \mathbf{H} is equivalent to a single point in the 3D space, the multitude of $\mathbf{H}(\vec{k})$ for all possible \vec{k} defines some shape. Being a point in the Brillouin zone, \vec{k} is a cyclic coordinate in all its dimensions. Thus³, $\mathbf{H}(\vec{k})$ is a 1D loop if \vec{k} has a single component (1D Brillouin zone) and the surface of a torus if it has 2 components (2D Brillouin zone).

Let's now consider the classification of Hamiltonians in a 1D Brillouin zone represented by loops in a 3D space. The loops cannot go through the origin, still, it is intuitively clear that any loop can be deformed into another one continuously without "crossing" the origin. Thus, all 1D Hamiltonians are topologically equivalent.

To demonstrate the case of a non-trivial topology let's consider 2D Hamiltonians $\vec{k} = (k_x, k_y)$ represented by tori. It appears that not every torus can be continuously deformed into another one without crossing the origin. Thus, there are topologically nonequivalent 2D Hamiltonians. An illustration is given in Fig. 1.6 where the origin point is enclosed by the torus. The topological invariant for the 2D Hamiltonian (winding number) is equivalent to the

²Vacuum may be viewed as a solid with an infinite band gap

³Provided $\mathbf{H}(\vec{k})$ is continuous

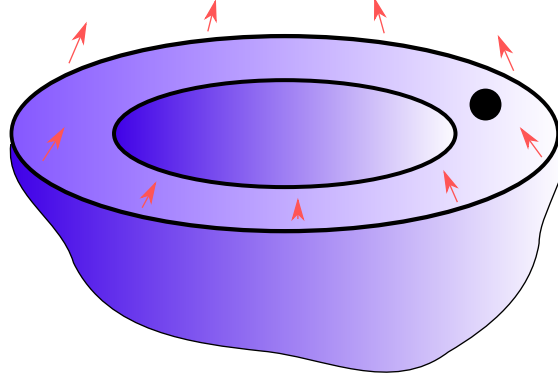


Figure 1.6 – Torus enclosing the origin point (black) as an illustration to topologically non-trivial Bloch Hamiltonian. The origin points representing the gap closing cannot be continuously transferred outside the torus without pinning it. It is equivalent to the statement that topologically non-trivial Hamiltonian cannot become topologically trivial without closing the gap.

number of times the torus wraps the origin⁴. Since no Hamiltonian symmetries have been considered this picture corresponds to the QHE where the winding number is Chern number.

The Kane-Mele model is a model of a band insulator. Practically, to understand whether a band insulator is in its trivial state or not one calculates the corresponding topological invariant as it was done by Kane and Mele. The vast majority of real insulating materials, however, are trivial in terms of the band topology. Thus, one has to make an intelligent choice to discover TIs, such as focusing on compounds with large relativistic effects. There, reordering of atomic orbitals caused by the interaction with heavy atomic nuclei may induce a topological phase. Upon leaving the topological insulator phase and entering the trivial one the band order has to be restored such that the gap closes and reopens again. Thus, there exist boundary gapless modes. These states are decoupled from the bulk states by a bulk band gap. In the case of a 2D \mathbb{Z}_2 topological insulator there is a single spin-up and a single spin-down in-gap mode, Fig. 1.5(left). They have opposite group velocities, the fact known as spin-momentum locking. Provided there are no spin-flip processes, the edge of a TI acts as an ideal nanowire: most scattering processes become prohibited due to the lack of a counter-propagating mode.

The first transport experiment confirming the edge states was preformed with 2D HgTe quantum wells where a quantized conductance was observed[24]. It was shown that above certain thickness $d_c \sim 60\text{\AA}$ the quantum well is driven into topologically non-trivial state yielding edge states.

While 2D topological insulators host edge modes, 3D topological insulators host 2D surface states. Among the first candidates to host the 3D TI phase are bismuth calcogenides Bi_2Se_3 and Bi_2Te_3 showing gapless modes in angle-resolved photoemission spectroscopy (ARPES) experiments reported in Refs. [32, 33, 34, 35, 36, 37] where electronic structure of TI surface

⁴Provided self-crossings are allowed, a torus may wrap a particular point an arbitrary number of times.

was probed. The states are located at the Γ point and behave similarly to the ones in graphene: they form a Dirac cone with a linear dispersion law. Unlike in graphene, though, the states lack spin degeneracy and are *helical* meaning that the direction of spin polarization is locked to the group velocity[38] of the charge carrier as in 2D TIs.

Overall, TIs are materials with unique electronic properties suitable for electronic applications. The TIs are characterized by band inversions caused by relativistic effects and the appearance of edge modes. The transport with boundary modes may find applications in both conventional and next-generation electronics where the scattering processes limit device performance otherwise. The spin polarization of the states may also be useful for spintronics or quantum computing.

1.3.3 Defects in materials

The materials presented on Figs. 1.3,1.4 are crystals: the atoms forming materials are arranged in a lattice with a long-range translational order. The order may be complemented by a local structural disorder known as crystal defects. Defects modify electronic properties of a material in various ways: scatter charge carriers, absorb or donate electrons, change electronic structure of the material. Thus, it is important to understand how the defects are formed and what is their role in structural and electronic properties of a material.

An infinitely large number of possible defects can be characterized by two key parameters: defect type (intrinsic or impurity defect) and dimensionality (0D, 1D or 2D). Intrinsic defects may be atomic vacancies, antisites, domain boundaries while impurities come from environment, for example, oxidation and hydrogenation. Point, line and planar defects refer to dimensionality.

Each defect has an energy associated with its formation. This energy has to be introduced to the system for the defect to be formed: for example, to form a vacancy one breaks several atomic bonds. The sources of such energy are perturbations: thermal, chemical or induced by the light or an electric current. If it appears that the formation energy is negative than the existing atomic structure of the material is globally unstable. To derive formation energy one usually calculates potential energy of a system with a defect E_1 and compares it to the one without E_0

$$E_{\text{defect}} = E_1 - E_0 .$$

While the definition is very simple, calculating E_1 and E_0 is sometimes associated with a number of difficulties. To be meaningful, the formation energy implicitly assumes an underlying process where the number of atoms does not change. For the hydrogen adatom on graphene, for example, this means taking H_2 molecule from a gas, breaking the hydrogen bond and attaching both atoms to carbon. Alternatively, the source of H atom may be liquid (such as acid

solution) with different energies E_0 and E_1 . Thus, E_{defect} is not universal. The solution here is to introduce the chemical potential of particles [39] μ which depends on the environmental conditions. In the example of hydrogenated graphene one writes the following definition instead

$$E_{\text{defect}} = E_1 - N_C \mu_C - N_H \mu_H ,$$

where μ and N are the chemical potential and the particle number of corresponding (carbon, hydrogen) atoms. The advantage of such definition is that it does not involve initial state energy E_0 explicitly. However, provided such state is known, one may write additional conditions for chemical potentials. For example, if all carbon atoms come from graphene, then the chemical potential is equilibrated to the total energy of graphene E_{graphene} :

$$E_{\text{graphene}} = N_C \mu_C .$$

Similarly, if all hydrogen atoms come from H_2 molecule then

$$E_{\text{H}_2} = 2\mu_H .$$

The formation energy of defects is important for the *thermodynamic* description of material equilibrium with the surrounding environment. There are defects, however, which are rather described by *kinetics* than thermodynamics. The formation energy of line and plane defects is roughly proportional to the size of the defect and may reach arbitrarily high values. These defects are usually formed during material growth which is typically a non-equilibrium process.

For example, a grain boundary in 2D is a line defect. In chemical vapor deposited (CVD) MoS_2 line defects originate from crystallographic misalignment of bulk MoS_2 grains. There, multiple MoS_2 crystals start growing on same substrate. A crystallographic orientation of each grain, however, is chosen at the beginning of the process randomly. Once two grains extend towards each other the mismatch in the initial orientation is compensated by a line defect. A model of such defect is presented in Fig. 1.7(a). Since crystallographic orientations are bulk properties, this defect cannot be removed without destroying one of the bulk domains completely. In contrast, the sulfur vacancy line can be avoided by adding missing sulfurs locally, Fig. 1.7(b). There, bulk crystal orientations coincide.

In experiments, the defects in 2D are identified using microscopy techniques such as scanning tunneling microscopy (STM), transmission electron microscopy (TEM), atomic force microscopy (AFM). An example of resulting images is given in Fig. 1.8 where different kinds of defects (point and line) in a monolayer MoS_2 are presented.

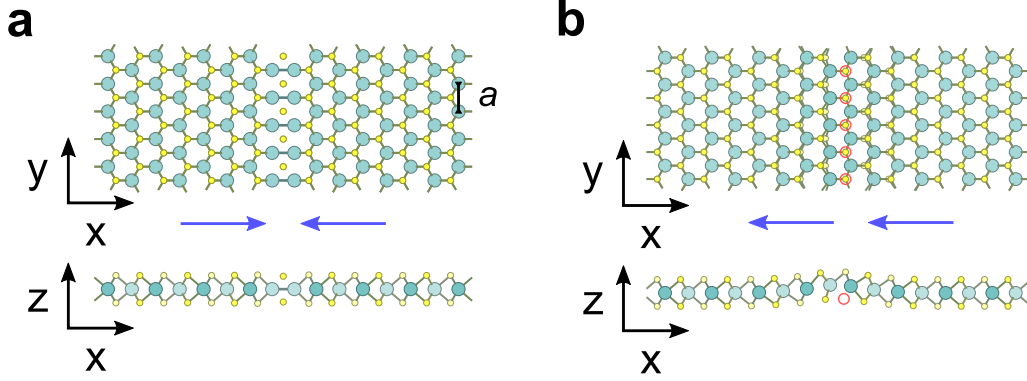


Figure 1.7 – Models of line defects in MoS₂, top and side views. (a) The inversion domain boundary is formed on the boundary between two MoS₂ crystals with opposite crystallographic orientations, blue arrows. Lattice constant of the bulk material a is indicated. (b) The sulfur vacancy line defect is formed by sulfur vacancies arranged into a line. The crystallographic orientation of the leads is same in this case.

Other extended defects in 2D and 3D include terminations (surfaces, edges), dislocations, disclinations and stacking faults. Defects and their properties are widely used in modern electronics: defects dope semiconductors with electrons or holes, act as light emitting centers in solid-state lasers and sense gases[42, 43]. Each of the above applications boils down to interactions of charge carriers with a defect. Understanding such interactions is of particular importance.

1.3.4 Charge carrier transport in solid state

Charge carriers moving through a solid form electric current $I = dQ/dt$ where the right hand side is a time change of an electric charge in the reservoirs. Current is an averaged quantity directed along the bias V , $I = G \cdot V$, where conductance G is a constant representing transparency of the media for the charge carriers. Conductance G is reduced if charge carriers scatter on defects and various quasi-particles populating a material such as phonons and magnons. Usually, under normal conditions, the scattering dominates in charge carrier transport: electrons propagate in arbitrary directions while the applied voltage causes drift of electron gas as a whole. This transport regime is called diffusive: charge carriers diffuse and scatter inside the material similarly to Brownian particles. Electrons are assumed to propagate freely between scattering events. This defines the charge carrier mean free path λ . Thus, for diffusive transport λ is small: $\lambda \ll l$ where l is the device size (distance between the leads).

In the Ohmic regime conductance is proportional to the mean free path, $G \propto \lambda$. Thus, to increase conductance G one improves mean free path λ , thus, making electron scattering less frequent. It can be done by several means: reducing the temperature, producing cleaner materials and decreasing a device size. At some point electrons start travelling between leads without scattering $\lambda > l$ and transmission G saturates. This transport regime is called ballistic.

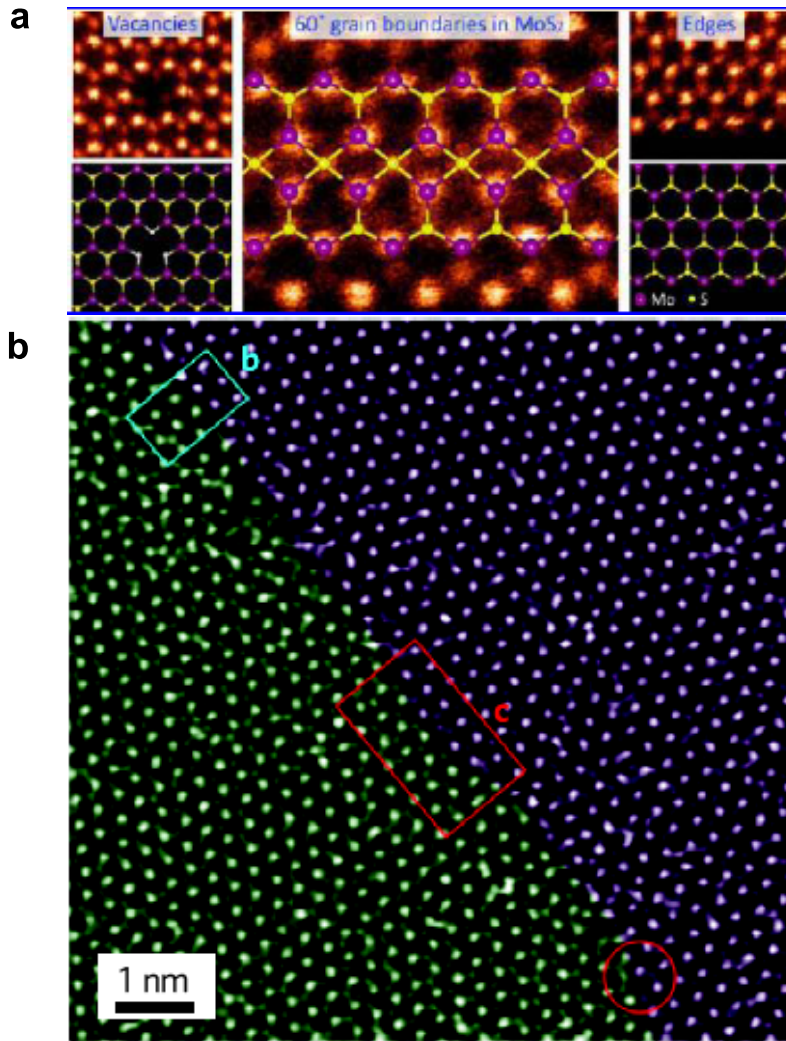


Figure 1.8 – Defects observed in MoS₂. (a) Point defects (left), periodic line defects (middle) and regular edges (right) from Ref. [40]. (b) Grain boundary from Ref. [41].

For example, ballistic transport occurs in superconductors where scattering is prohibited by energy conservation (superconducting energy gap). In the ballistic transport regime wave properties of electrons can be exploited. Provided a small amount of disorder, an electron becomes delocalized between electrodes. Thus, it becomes a purely quantum mechanical object with all relevant attributes such as abilities to tunnel, carry phase and interfere.

Ballistic transport is one of the exciting charge carrier transport phenomena in solid-state physics. In 2D the ballistic transport regime can be achieved in graphene[44] where charge carriers have a mean free path of the order of micrometers even at room temperature. Other charge carrier transport phenomena include superconductivity, sub-barrier tunneling, magnetoresistance, spin-polarized transport, non-linear current-voltage dependence in semiconductors, skin effect, transport in systems with smaller dimensionality (such as a 2D free electron

1.3. Novel materials for applications in electronics

gas or a 1D nanowire transport), transport through quantum dots, Coulomb blockade, Kondo effects and many more. Most of these phenomena are already implemented in real devices making the study of electron transport one of the most important topics in the solid-state physics and materials science.

2 Methodology

2.1 Density functional theory (DFT)

Density functional theory (DFT) is a tool to describe and calculate electronic, mechanical and optical properties of materials and molecules. It is usually referred to as *ab-initio* (Latin “from the beginning”) to make contrast with empirical approaches relying on experimental data¹. DFT starts from properties of individual elementary particles (electrons, protons) to form a complete description of a material. This section is dedicated to key points about DFT and the role of charge density in description of materials’ electronic properties.

2.1.1 Kohn-Sham equations

Electronic properties include different aspects of behavior of electrons: motion, interaction, correlations. In solid state, electrons are found only in the vicinity of positively charged atomic nuclei of the solid forming a Coulomb potential well. The mass of a single atomic nucleus is 3-4 magnitudes larger than the mass of an electron. Thus, any kind of excitation will cause electrons to reach equilibrium much faster than heavy atomic nuclei. This means that above certain time scale (femtoseconds), electrons are in equilibrium with an underlying atomic structure which may be considered to be “pinned” to the surrounding space. Thus, the atomic nuclei can be simplified to classical point objects with mass and charge, the Born-Oppenheimer approximation. The quantum mechanical nature of the atomic nucleus is completely neglected. This allows to write the following electronic Hamiltonian:

$$H = T + V + U = \sum_i^N \left(-\frac{\hbar^2}{2m_i} \nabla_i^2 \right) + \sum_i^N V(\vec{r}_i) + \sum_{i<j}^N U(\vec{r}_i, \vec{r}_j), \quad (2.1)$$

where T is the kinetic energy of electrons, V is the external potential created by nuclei and U is the interaction between electrons. Above equation works well in solid state but still too difficult to solve unless a very special case occurs (such as $U = 0$). The reason for that lies in

¹Modern DFT, however, often includes empirical constants in approximate exchange-correlation functionals

the quantum mechanical nature of electrons: each of them exists in a dedicated space such that for N electrons one has a $3N$ -dimensional wavefunction to be found: $\psi(\mathbf{r}_1, \mathbf{r}_2, \dots, \mathbf{r}_N)$. The complexity to solve Eq. 2.1 grows exponentially with the number of electrons and is commonly believed to be too high. A rather obvious simplification here is to limit consideration from $3N$ -dimensional space to 3D with a single-particle picture of electron interactions. Two of the three terms in Eq. 2.1 are single-particle terms: both kinetic energy and external potential are defined for a single electron. In contrast, the third term U representing electron-electron interaction is meaningless for a single electron. The mean-field approximation overcomes this issue.

The mean-field approximation takes different forms in different solid-state problems but the idea is always the same: replace the two-particle potential by interaction of a particle with a particle density. The mean field captures all classical aspects of interaction and is a starting point for more advanced methods (such as the configuration interaction approach). Under the mean-field approach, the Coulomb interaction U in Eq. 2.1 becomes an interaction with a charge density, a spin exchange interaction becomes an interaction with magnetic moments and so on. The mean-field approximation is usually designed in a way to be able to reproduce exact interaction in non-correlated systems which can be solved exactly.

In DFT, the mean field is presented by the exchange-correlation functional replacing the electron-electron interaction term and depending on the charge density $\rho(\mathbf{r})$ in the most general way[45]. The Hamiltonian becomes a functional of the charge density $\rho(\mathbf{r})$:

$$H_{\text{KS}}(\rho(\mathbf{r}))\psi_i = \left(-\frac{\hbar^2}{2m}\nabla^2 + V(\mathbf{r}) + \mu_{\text{xc}}[\rho(\mathbf{r})] \right) \psi_i = E_i \psi_i, \quad (2.2)$$

where μ_{xc} is the exchange-correlation functional of the charge density ρ . This Hamiltonian is a Kohn-Sham Hamiltonian introduced in 1965[46]. It is complemented by the corresponding charge density in the real space

$$\rho(\mathbf{r}) = \sum_i f(E_i) |\psi_i(\mathbf{r})|^2 \quad (2.3)$$

where $f(E)$ is the Fermi-Dirac energy distribution function. Above two equations are Kohn-Sham equations to be solved self-consistently. Resulting solution minimizes the Kohn-Sham total energy functional $E_{\text{tot}}(\rho)$ and is an exact ground state charge density with an exact total energy E_{tot} according to Hohenberg-Kohn theorems.

2.1.2 Limitations of DFT

So does DFT solve the many-body problem in general? The answer is “no” because the exact exchange-correlation functional and, thus, the Hamiltonian are unknown². However, there

²Knowing exact exchange-correlation functional makes no sense anyway: computing it will likely involve as much resources as the original problem Eq. 2.1 does.

are reasonable approximations to the contribution E_{xc} of electron exchange and correlation effects to the total energy called local density[46] and generalized gradient[47] approximations (LDA and GGA):

$$E_{xc}^{LDA} = \int \epsilon^{LDA}(\rho(\mathbf{r})) \rho(\mathbf{r}) d\mathbf{r}, \quad (2.4)$$

$$E_{xc}^{GGA} = \int \epsilon^{GGA}(\rho(\mathbf{r}), \nabla \rho(\mathbf{r})) \rho(\mathbf{r}) d\mathbf{r}. \quad (2.5)$$

The symbol $\epsilon(\dots)$ is a simple function, thus, both approximations are *local*. These approximations provide a reasonable description of an overwhelmingly large number of experimentally available systems. Otherwise more advanced techniques can be used, such as hybrid functional approaches, the GW approximation, DFT+U schemes, etc. Some of these techniques include empirical terms to fit experimental data. Moreover, the sole fact of the *choice* between approximations makes DFT empiric as reflected in several studies[48, 49].

Without knowing an exact exchange-correlation functional DFT is rather an empiric model than a formally valid approximation: it is difficult to estimate and systematically reduce errors of the total energy or any other quantity computed by DFT. In other words, it is impossible to know how good LDA, GGA or any other approximation solves the electronic Hamiltonian Eq. 2.1.

The Hohenberg-Kohn theorems stating existence of an exact total energy functional $E_{tot}(\rho(\mathbf{r}))$ are not practical either: they refer to the ground state only and do not guarantee existence of expressions for other important quantities to compute (such as excited states of a solid, for example). Thus, the single-particle states ψ_i in Eqs. 2.2, 2.3 lack physical meaning, especially for strongly-correlated systems.

Nevertheless, DFT describes well most nanoscale systems without strong correlations. This includes crystals and isolated systems, conductors and insulators, systems with magnetic order, disordered systems including liquid, amorphous materials and alloys, materials with defects and many more. The success of DFT may be attributed to the fact that it is relatively simple to understand and undemanding; the solutions of Eq. 2.2 can be predicted and reproduced. This makes DFT a leading computational tool and a gold standard in material science, solid-state physics and chemistry fields.

2.1.3 DFT in crystals, the Bloch theorem and the Brillouin zone

Crystal is a solid material extending infinitely in one or more directions with atoms preserving long-range translational order. Inside a crystal, a lattice can be defined where atoms occupy well-defined positions, such as a hexagonal lattice in graphene, Fig. 1.4. Crystalline lattices are periodic: the atoms occupying lattice sites can be exchanged by simply shifting the whole

Chapter 2. Methodology

lattice by some vector \vec{d} . All such possible vectors are called *translation vectors* referring to the translational symmetry of the lattice. Depending on whether a lattice is 1D, 2D or 3D there exist $D = 1, 2$ or 3 linearly independent lattice vectors \vec{a}_i forming a basis set for possible translations:

$$\vec{d} = \{n_i\} = \sum_{i=1..D} n_i \vec{a}_i, \quad (2.6)$$

where n_i are integers. The vectors \vec{a}_i form a *unit cell* of the lattice while various sets of vectors \vec{d} form *supercells*. However, the choice of vectors \vec{a}_i and a unit cell is not unique. For example, negative vectors $-\vec{a}_i$ also satisfy Eq. 2.6, thus, they form another unit cell having the same volume.

A unit cell of a crystal contains a finite amount of atoms, for example, 2 carbon atoms in graphene and a single molybdenum atom together with 2 sulfur atoms in MoS_2 . Thus, a periodic crystal is described by a single unit cell with a few atoms inside it. For the quantum mechanical treatment, it is possible to replace an infinite crystalline solid by a single unit cell by using the Bloch theorem. It gives an integral of motion, the *pseudomomentum* k , for an electronic wavefunction in a periodic environment. Mathematically, the Bloch theorem allows to diagonalize an infinite matrix with a periodic structure. For example, consider following tridiagonal matrix H which may be viewed as a single-band model Hamiltonian of an infinite atomic chain where each atom with the energy ϵ interacts with nearest neighbors only through the hopping integral λ :

$$H = \begin{bmatrix} \dots & \dots & \dots & \dots & \dots & \dots \\ \dots & \epsilon & \lambda & 0 & 0 & \dots \\ \dots & \lambda^* & \epsilon & \lambda & 0 & \dots \\ \dots & 0 & \lambda^* & \epsilon & \lambda & \dots \\ \dots & 0 & 0 & \lambda^* & \epsilon & \dots \\ \dots & \dots & \dots & \dots & \dots & \dots \end{bmatrix}. \quad (2.7)$$

Hamiltonian H is Hermitian though it is not important for the Bloch theorem. The eigenvalue equation $H\psi = E\psi$ results in the following equation for the wavefunction element ψ_i

$$\lambda\psi_{i-1} + \epsilon\psi_i + \lambda^*\psi_{i+1} = E\psi_i, \quad (2.8)$$

where i is the index of an atom, an arbitrary integer. Generally, to solve the above system of equations one needs to fix 2 arbitrary values of ψ (boundary conditions) as well as the energy E . Or the other way, for each energy E the wavefunction ψ is a linear combination of two orthogonal functions, i.e. all states are doubly degenerate. To find both states a Fourier transform is performed such that

$$\psi_{i+1} = c\psi_i, \quad (2.9)$$

yielding following quadratic equation

$$\lambda c^{-1} + \epsilon + \lambda^* c = E . \quad (2.10)$$

The above quadratic equation has two solutions in general³. Thus the ansatz, Eq. 2.9 diagonalizes the Hamiltonian Eq. 2.7. The eigenstates are simply $\psi_i = c^i \psi_0$, the fact known as Bloch theorem for $|c| = 1$. In the latter case, a complex phase κ is gained for the wavefunction in each cosequative unit cell

$$\psi_n = \psi_0 e^{in\kappa} . \quad (2.11)$$

Finally, if $|c| \neq 1$ the state ψ cannot be normalized: it grows to infinity in positive or negative direction. Such states may exist in a finite system but they are usually irrelevant for bulk crystals. By substituting Eq. 2.11 into Eq. 2.8 it is possible to derive the energy dispersion as a function of κ

$$E(\kappa) = \epsilon + 2\text{Re}\lambda \cdot \cos \kappa + 2\text{Im}\lambda \cdot \sin \kappa . \quad (2.12)$$

The quantity κ is a Bloch wave number, the integral of motion of Hamiltonian Eq. 2.7.

To complete the picture of the Bloch approach, consider a real space periodic Hamiltonian originating from, for example, DFT description of a crystalline solid. There, the translational invariance is expressed as $H(\vec{r}) = H(\vec{r} + \vec{d})$ where \vec{d} is a lattice vector. The shifted wavefunction gains phase

$$\psi(\vec{r} + \vec{d}) = \psi(\vec{r}) \cdot e^{i\vec{k} \cdot \vec{d}} . \quad (2.13)$$

Re-writing above gives

$$\psi(\vec{r}_2) = \psi(\vec{r}_1) \cdot e^{i\vec{k} \cdot (\vec{r}_2 - \vec{r}_1)} , \quad (2.14)$$

where $\vec{r}_{1,2}$ correspond to same point in different unit cells of the crystal. Finally, the Bloch function ϕ is defined as

$$\psi(\vec{r}_2) e^{-i\vec{k} \cdot \vec{r}_2} = \psi(\vec{r}_1) \cdot e^{-i\vec{k} \cdot \vec{r}_1} = \phi(\vec{r}_2) = \phi(\vec{r}_1) . \quad (2.15)$$

As it is evident, it is periodic in solid and differs from the wavefunction by a Bloch factor $e^{i\vec{k} \cdot \vec{r}}$

$$\psi(\vec{r}) = \phi(\vec{r}) e^{i\vec{k} \cdot \vec{r}} . \quad (2.16)$$

The Bloch function is an eigenstate of the Bloch Hamiltonian defined as a Fourier transform

³Including infinitely large solutions. Cases with coinciding solutions $(\epsilon - E)^2 = 4|\lambda|^2$ correspond to band edges and are not considered.

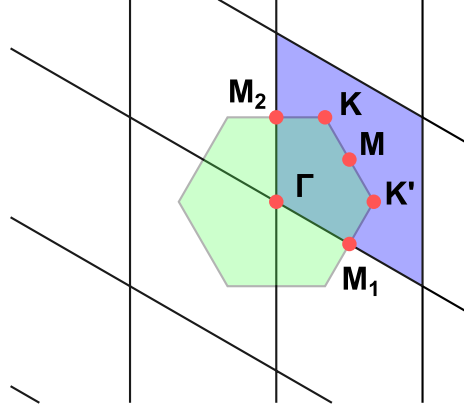


Figure 2.1 – The periodic reciprocal space for a 2D hexagonal lattice such as graphene. The reciprocal unit cell is highlighted in blue while the (first) Brillouin zone is a green hexagon. The high-symmetry points Γ , M , $M_{1,2}$, K , K' are indicated.

of the periodic Hamiltonian inside the unit cell (U.C.):

$$H(\vec{k}) = \int_{\text{U.C.}} d\vec{r} e^{i\vec{k} \cdot \vec{r}} \cdot H(\vec{r}) . \quad (2.17)$$

Calculating the Hamiltonian in *real* \vec{r} -space and transforming it into *reciprocal* \vec{k} -space is often a part of self-consistent procedure to solve DFT Eqs. 2.2,2.3.

Diagonalizing $H(\vec{k})$ yields energy eigenvalues $E_n(\vec{k})$ depending on the wave vector \vec{k} and the band index n . $E_n(\vec{k})$ is usually referred to as electronic band structure, examples are given in Fig. 1.3 (b,d). Since $H(\vec{k})$ is periodic in reciprocal space it is possible to define the reciprocal unit cell. The (first) Brillouin zone is defined on the basis of the reciprocal unit cell, see Fig. 2.1 as an example. The Brillouin zone has its center $\vec{k} = 0$ and contains locus of points that are closer to the origin than to any other periodic replica of Γ . Though both the reciprocal unit cell and the Brillouin zone can be used to describe reciprocal space, the former one usually contains more relevant symmetries such as the hexagonal symmetry in the example in Fig. 2.1.

The Bloch description is essentially a Fourier transform of the Hamiltonian given in Eq. 2.17. It simplifies the eigenvalue equation, however, many more problems have to be solved during the self-consistent cycle. One more example where the Fourier transform gives unbeatable performance is the calculation of a Coulomb potential $V_c(\vec{r})$ from periodic charge density $\rho(\vec{r})$. The Laplace equation connecting both has the following form

$$\Delta V_c(\vec{r}) = \rho(\vec{r}) , \quad (2.18)$$

where Δ is the Laplace second derivative operator. Depending on the boundary conditions, different methods can be used to solve it. The simplest case, however, is when periodic

boundary conditions are assumed. In this case, it is possible to transform the above equation into reciprocal space where it becomes a trivial expression

$$\frac{V_c(\vec{k})}{k^2} = \rho(\vec{k}). \quad (2.19)$$

In 3D, the time needed to perform the Fourier transform scales with the number of grid points along one of the dimensions N as $N^3 \log N$ which is much better than if boundary conditions would have been located at infinity with time scaling of N^6 . Thus, even isolated systems without PBC are usually considered to be periodic within large enough unit cell to avoid interaction between replicas.

2.1.4 Core electrons and pseudopotentials

As it was described in the previous section, a typical subject of the DFT is a periodic unit of a solid – the unit cell containing several atoms. The number of electrons in a unit cell is a sum of atomic numbers of all unit cell atoms Z_i . Sometimes this number is small (there are 24 electrons per unit cell of graphene for example), but may also grow to thousands if a more complex problem is considered. A further simplification was developed to reduce the number of electrons considered called the pseudopotential approximation.

To understand the pseudopotential approximation, consider an atomic nucleus with Z protons creating a Coulomb potential $V(\vec{r}) = -Z/|r|$. It is known since Niels Bohr (1913) that such potential hosts discrete electronic orbitals with energies varying from tens to fractions of eV. Electrons with smaller energies form the valence shell of an atom while the rest of electrons are localized around the nucleus (core electrons). The size of the corresponding orbitals is much smaller than the interatomic distance, thus, the core electrons do not participate in most properties such as chemical bonding, low-energy excitations and transport. The idea behind pseudopotential approximation is to remove core electrons from the consideration by replacing Coulomb potential with a pseudopotential.

To construct a pseudopotential one performs the following steps:

1. Choose an atom and perform an all-electron calculation of electronic states ψ_i^{ae} and corresponding energies E_i within selected DFT formalism;
2. Choose an energy threshold $E_{\text{threshold}}$ and assign all states below this energy $E_i < E_{\text{threshold}}$ to be core states:
 - smaller $E_{\text{threshold}}$ includes more electrons in the valence, thus, the pseudopotential becomes more exact and more computationally expensive;
 - larger $E_{\text{threshold}}$ includes more electrons in the core instead: these electrons become “frozen” and the pseudopotential becomes less transferrable but also computationally cheaper;

3. Pick a core radius r_c above which the valence electronic wavefunction of the future pseudopotential ψ_i^{ps} matches exactly the corresponding all-electron wavefunction $\psi_i^{\text{ae}}(r) = \psi_i^{\text{ps}}(r)|_{r>r_c}$. This parameter discards properties of the valence wavefunctions inside the core similarly to the core states being discarded. Thus:
 - the core radius r_c should be smaller than, literally, half of the bond length between atoms in a solid;
 - but it should be larger⁴ than the distance to the outermost radial node of ψ_i^{ae} ;
 - larger r_c gives more freedom to construct a “softer” pseudopotential with smoother wavefunctions and better convergence properties;
 - in contrast, smaller r_c in hard pseudopotentials will reproduce bonding better for the cost of performance. Resulting pseudopotential becomes more universal and transferable between different solids;
 - r_c may be chosen individually for each state ψ_i^{ps} ;
4. Construct pseudowavefunctions ψ_i^{ps} inside the core matching various conditions such as softness, conservation of norm and matching of logarithmic derivatives. This step ensures various physical quantities such as lattice constant, binding energy, etc are reproduced correctly.
5. Restore the pseudopotential by calculating $V_{\text{ps}} = \sum_i |\psi_i^{\text{ps}}\rangle E_i \langle \psi_i^{\text{ps}}| - T$, where T is the kinetic energy operator. For V_{ps} to be local one has to take necessary measures at the previous step.
6. For convenience, one also has to remove Hartree and exchange-correlation contributions which will be taken into account when this pseudopotential is used in a calculation of a solid.

As it was pointed out, the pseudopotential has to be transferable: it should reproduce as many experimentally available quantities as possible. Constructing such pseudopotential, however, is a trial and error process.

2.1.5 Electron spin and spin-orbit coupling in DFT

The physics of an electron spin $\sigma = \uparrow, \downarrow$ in DFT may be presented by spin-dependent charge density $\rho_\sigma(\vec{r})$ and wavefunctions $\psi_\sigma(\vec{r})$. In the simplest case of a scalar-relativistic approximation, the whole Kohn-Sham Hamiltonian is split into two spin-dependent parts H_σ solved separately. In spin-neutral systems the Hamiltonians become equal: $H_\uparrow = H_\downarrow$. In this case, every electronic state is at least doubly degenerate and hosts pairs of electrons with opposite spins. Upon adding magnetic field or spontaneous spin polarization the energy levels become

⁴To make the pseudopotential *local* the nodes $\psi(r)^{\text{ae}} = 0$ cannot be reproduced by the pseudowavefunction ψ_i^{ps} , see Fig. 2.2

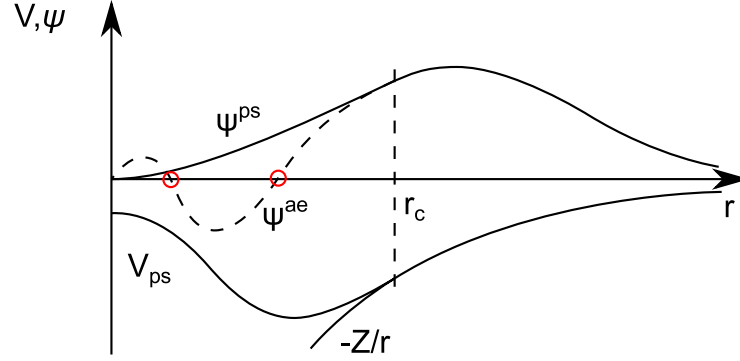


Figure 2.2 – A sketch of a pseudopotential V_{ps} and the corresponding wavefunction ψ^{ps} versus Coulomb potential of the atomic nucleus and the all-electron wavefunction ψ^{ae} (dashes).

split: one of the spin occupies a more energetically favorable configuration while the other one stays at higher energies, the effect named after Dutch physicist P. Zeeman. Corresponding energy gain is

$$\Delta = -\vec{\mu}_B \cdot \vec{B}, \quad (2.20)$$

where \vec{B} is a vector of magnetic field or an exchange field and μ_B is Bohr's magneton: electron magnetic moment. According to the above formula, the vector field causes a non-zero spin polarization.

The Zeeman term, however, is the consequence of a more general relativistic Dirac Hamiltonian for an electron traveling at relativistic speeds. It was proposed in 1928 and has the following form

$$i\hbar \frac{d\psi}{dt} = (c\vec{\alpha} \cdot \vec{p} + \beta m_e c^2) \psi, \quad (2.21)$$

where \hbar is the Planck's constant, ψ is a four-component wavefunction, c is the speed of light, \vec{p} is a momentum of an electron, m_e is electron mass and α, β are 4x4 matrices

$$\alpha_{x,y,z} = \begin{bmatrix} 0 & \sigma_{x,y,z} \\ \sigma_{x,y,z} & 0 \end{bmatrix}, \quad \beta = \begin{bmatrix} 1 & 0 & 0 & 0 \\ 0 & 1 & 0 & 0 \\ 0 & 0 & -1 & 0 \\ 0 & 0 & 0 & -1 \end{bmatrix}, \quad (2.22)$$

σ_i are Pauli spin operators

$$\sigma_x = \begin{bmatrix} 0 & 1 \\ 1 & 0 \end{bmatrix}, \quad \sigma_y = \begin{bmatrix} 0 & -i \\ i & 0 \end{bmatrix}, \quad \sigma_z = \begin{bmatrix} 1 & 0 \\ 0 & -1 \end{bmatrix}. \quad (2.23)$$

Chapter 2. Methodology

The external electromagnetic field is introduced via a scalar potential ϕ and a vector potential \vec{A} interacting with electron charge q

$$i\hbar \frac{d\psi}{dt} = (c\vec{\alpha} \cdot [\vec{p} - q\vec{A}] + \beta m_e c^2 + q\phi) \psi. \quad (2.24)$$

To identify the most important terms, the wavefunction is split into a couple of two-component spinors ψ_1, ψ_2 (electron and positron wavefunctions). It becomes possible to write down the following system

$$\begin{aligned} i\hbar \frac{d\psi_1}{dt} &= c\vec{\sigma} \cdot [\vec{p} - q\vec{A}] \psi_2 + (m_e c^2 + q\phi) \psi_1 \\ i\hbar \frac{d\psi_2}{dt} &= c\vec{\sigma} \cdot [\vec{p} - q\vec{A}] \psi_1 + (-m_e c^2 + q\phi) \psi_2. \end{aligned} \quad (2.25)$$

Its time-independent form is

$$\begin{aligned} 0 &= c\vec{\sigma} \cdot [\vec{p} - q\vec{A}] \psi_2 + (-E + q\phi) \psi_1 \\ 0 &= c\vec{\sigma} \cdot [\vec{p} - q\vec{A}] \psi_1 + (-E - 2m_e c^2 + q\phi) \psi_2. \end{aligned} \quad (2.26)$$

Note that $m_e c^2$ is a constant energy shift. Taking $m_e c^2$ to be the largest energy scale in the problem, it is possible to expand the above two equations in powers of $1/c$. The solution of the system up to the second order is the following

$$\left[\frac{(\vec{p} - q\vec{A})^2}{2m_e} + q\phi - \frac{\hbar q}{2m_e} \vec{\sigma} \cdot \vec{B} - \frac{p^4}{8m_e^3 c^2} + \frac{\hbar^2 q}{8m_e^2 c^2} \Delta - \frac{\hbar q}{4m_e^2 c^2} \vec{\sigma} \cdot [(\vec{p} - q\vec{A}) \times \nabla] \right] \psi_1 = E \psi_1, \quad (2.27)$$

where $\vec{B} = \nabla \times \vec{A}$ - magnetic field, Δ - Laplace operator. The first three terms in the above constitute a non-relativistic Hamiltonian of an electron in electric and magnetic fields. In particular, the third term is the Zeeman term introduced in the beginning of the section. The rest of the terms are known as relativistic corrections to the energy: mass, Darwin and spin-orbit couplings (the last term). The spin-orbit term, in particular, couples electron spin and momentum. It is non-local and, thus, cannot be reduced to magnetic field action. The wavefunction $\psi = \psi_1$ is the spinor wavefunction containing superposition of the electronic spin-up and spin-down states. Thus, the general form of the Kohn-Sham spin-orbit Hamiltonian is non-local in spin $H_{\sigma, \sigma'} \neq 0$. Similarly, the charge density matrix $\rho_{\sigma, \sigma'}$ has spins coupled.

Relativistic treatment is especially important for solids with heavy atoms where electron momentum p is large. There, the spin-orbit coupling causes energy splittings in the band structure and spin polarization of bands like in the case of MoS₂ illustrated in Fig. 1.3(d).

2.1.6 Single-electron basis in DFT

To be able to solve Kohn-Sham equations numerically one has to write every relevant quantum mechanical operator in some basis set. The most popular basis sets used in existing

2.1. Density functional theory (DFT)

	Plane waves	Localized basis sets	Mixed basis sets
Origin	eigenstates of the momentum operator p	atomic or atomic-like (gaussian) wavefunctions	both types of states form the basis
In r -space In k -space	e^{ik_0r} $\delta(k - k_0)$	localized quasi-delocalized	both both
Parameters	cutoff k_{\max} specifying number of plane waves	various parameters describing the number and shapes of wavefunctions	both
Completeness Orthogonality	when $k_{\max} \rightarrow \infty$ ✓	non-systematic ✗	as in plane waves ✗
Pros	Easy to introduce; systematic convergence with respect to k_{\max} ; describes well valence and free electrons; no overhead with respect to the Fourier transform	Compact flexible basis sets for both small and large systems; work well for isolated molecules; natural basis for orbital analysis and all-electron calculations; computationally undemanding	Combines the advantages of both; designed for description of complex systems such as a molecule on a metallic surface
Cons	Impossible to use without pseudopotential approximation; isolated, truncated systems such as surfaces and molecules require significantly larger basis sets	No systematic convergence; free-like electrons require additional basis functions; the number of parameters to tweak is roughly equal to the number of electrons in the system; numerical problems related to non-orthogonality	The steepest learning curve; numerical problems related to non-orthogonality; efficient implementation requires enormous effort; introduction of new features is delayed because of the above

Table 2.1 – Comparison of basis sets used in DFT simulations.

DFT simulation programs in materials science are either *plane waves*, *localized basis sets* or a mixture of both. Table 2.1 contains a short summary on the three options.

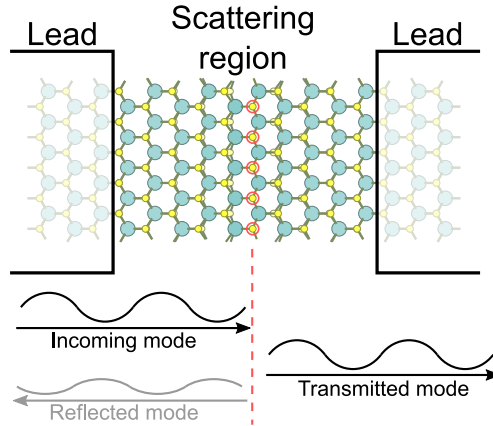


Figure 2.3 – A schematic illustration of a two-terminal ballistic transport setup. The sulfur vacancy line defect in MoS₂ plays a role of a potential barrier for ballistic charge carriers. The incoming mode from one of the leads is split into reflected mode as well as the transmitted mode traveling to another lead.

2.2 Ballistic transport at nanoscale with DFT

While DFT is a study about ground state properties, experimental spectroscopic studies probe materials by driving them into an excited state and reading out the response. A number of extensions to DFT have been developed to simulate different kinds of a non-equilibrium state which also includes particle transport phenomena. As it was already pointed out previously, DFT does not guarantee correctness of any other quantity except total energy and charge density unless exchange and correlation effects can be neglected. It is the case in the ballistic transport regime where two-particle scattering effects are rare. While the concept of ballistic transport was introduced previously in this section practical some aspects are covered.

The ballistic transport regime is defined as a regime where the distance between charge carrier reservoirs (contacts, leads) is smaller than the mean free path (the mean distance between charge carrier two-particle scattering events). The leads host electronic states which are the endpoints for electronic transport. The states in the leads are referred to as *lead modes* in Fig. 2.3. Ballistic charge carriers are transmitted between lead modes via channels in the *scattering region*. The channels define the charge carrier current resistance R which can be measured. Once a voltage is applied the charge carriers will start moving towards negative bias and will soon reach a dynamical equilibrium resulting in a stationary regime for the charge density in the scattering region.

Depending on resistance R , some charge carriers will reflect from the scattering region back to the origin lead. The rest of the charge carriers will transmit further. The probability of being transmitted through the scattering region is called *transmission probability* T . Transmission probability is a function of various parameters such as energy of the charge carrier, shape of the lead modes and electrostatic potential in the scattering region. Transmission probability

has no units and takes values from 0 (no transmission, all charge carriers reflected) to 1 (all charge carriers transmitted). Based on values of T , the scattering region is characterized to be reflective or transparent by analogy with reflection of light. The resistance R is inversely proportional to the sum of transmission probabilities of all channels T_i

$$R = \frac{h}{e^2 \sum_i T_i} . \quad (2.28)$$

The quantity $\frac{2e^2}{h}$ combining electron charge e and Planck's constant h is called conductance quantum: a maximum possible conductance achieved by a single charge carrier transmission channel. The resulting charge carrier current is computed using the Landauer-Buttiker formula

$$I = \frac{e}{h} \int dE T(E) f'(E) , \quad (2.29)$$

where $f'(E)$ is the perturbation to the equilibrium distribution function and T is the sum of transmission probabilities at a given energy.

The total energy E of a ballistic charge carrier is conserved if no inelastic processes are present. For 2D (atomic layers) and 3D (bulk) leads we will also consider conservation of the pseudomomentum \vec{k}_{\parallel} orthogonal to the transport direction provided the entire system is a subject to periodic boundary conditions. For example, the pseudomomentum along the periodic line defect shown in Fig. 2.3 is conserved. After integrating out all conserved quantities the scattering problem becomes a 1D quantum mechanical problem for a particle traveling through the barrier. It can be solved efficiently using the Green's function formalism.

2.2.1 Green's function formalism

The Green's function formalism is widely adopted for calculation of ballistic transport properties, see Refs. [50, 51, 52] for examples. It allows to take into account semi-infinite leads in an exact way via their surface Green's functions and self-energies. This method is general enough: it does not make any assumptions of the underlying structural and electronic properties such as the presence of band gap, magnetic ordering, dimensions of the setup or number of leads. There are several pre-requisites that have to be satisfied, though:

1. The leads are assumed to be ideal: all defects are present in the scattering region only.
2. The setup should be effectively one-dimensional. The treatment of 2D and 3D systems is also possible by introducing conserved projections of the pseudomomentum.
3. The Hamiltonian should be written in a tri-block-diagonal form. Practically, this means that the basis set for the Hamiltonian is localized and Hamiltonian matrix elements are truncated at a finite distance.

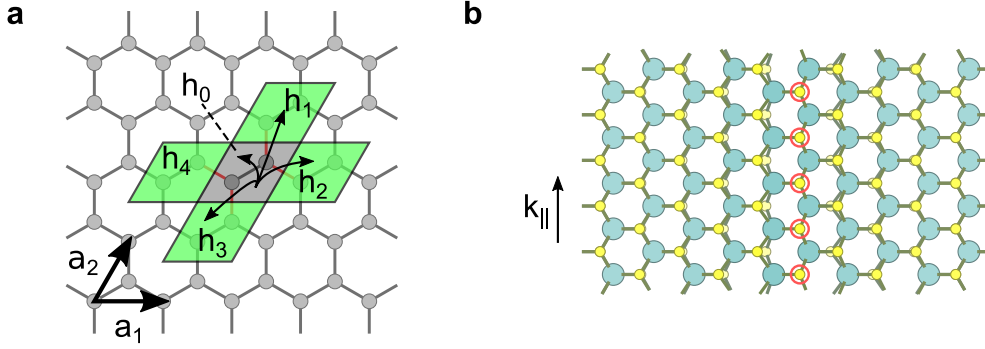


Figure 2.4 – Ideal and defective 2D systems. (a) A pristine graphene monolayer possessing a periodic atomic structure. The nearest neighbor tight-binding Hamiltonian of graphene without spin-orbit coupling $\lambda_{SO} = 0$ from Ref. [23] consists of 5 Hamiltonian matrices \mathbf{h}_i expressed in a localized atomic-like basis set (p orbitals of carbon). Corresponding hopping vectors \vec{R}_i in Eq. 2.30 are expressed in terms of lattice vectors: $\vec{R}_0 = 0$, $\vec{R}_1 = \vec{a}_2$, $\vec{R}_2 = \vec{a}_1$, $\vec{R}_3 = -\vec{a}_2$, $\vec{R}_4 = -\vec{a}_1$. (b) A line defect in monolayer MoS₂. The setup with a regular line defect is periodic only along its line. To describe a periodic line defect in MoS₂ one should consider conservation of pseudomomentum along the defect line $k_{||}$.

Procedure described further follows the mode matching approach from Ref. [53] while certain aspects of it have been simplified, improved and generalized by the author of this thesis. The recipe is outlined below.

Step 0: Integrate out projected pseudomomentum $k_{||}$

Before proceeding to the Green's function approach to electron transport dimensions of the system have to be reduced. This is done by integrating out projection of the pseudomomentum $k_{||}$ commuting with the initial Hamiltonian.

The Bloch form of a bulk periodic Hamiltonian expressed in a localized basis set is a finite sum of blocks with Bloch pre-factors

$$\mathbf{H}(\vec{k}) = \sum_i \mathbf{h}_i e^{i\vec{k}\vec{R}_i}, \quad (2.30)$$

where \mathbf{h}_i are finite-sized Hamiltonian matrices describing interactions between the unit cell at the origin and its displaced replica translated by the vector \vec{R}_i

$$\vec{R}_i = n_i \vec{a}_1 + m_i \vec{a}_2 + k_i \vec{a}_3 = (n, m, k)_i, \quad (2.31)$$

where \vec{a}_i are unit cell vectors, see also Fig. 2.4(a).

In the bulk geometry, Fig. 2.4(a), the pseudomomentum \vec{k} is a conserved quantity. In the device (defect) geometry, Fig. 2.4(b), one of the translation symmetries is no longer present.

It is still possible to apply the Fourier transform expressed in Eq. 2.30 to other dimension(s). The pseudomomentum \vec{k} becomes projection of the pseudomomentum onto the defect $\vec{k}_{||} = (k_2, k_3)$, Fig. 2.4(b). In this way a 2D or a 3D problem is reduced to a 1D problem $\mathbf{H}(k_{||})$. The latter can be viewed as nanowire with a point defect where $\vec{k}_{||}$ is an external parameter. Further in this section dependence on $\vec{k}_{||}$ is omitted.

Step 1: Prepare the 1D device problem

Notation

- i index of the lead
- j index of the unit cell inside the lead; 0 stands for the unit cell in close proximity to the device region; runs to $+\infty$
- r index of the lead mode (eigenstate)
- E energy of the charge carrier
- \mathbf{H} infinite Hamiltonian matrix
- \mathbf{h}_d finite diagonal part of \mathbf{H} corresponding to the device (scattering region)
- \mathbf{h}_i finite diagonal part of \mathbf{H} corresponding to the lead i
- \mathbf{S} infinite right-hand-side overlap matrix of the generalized eigenvalue equation (GEE) for the Hamiltonian written in a non-orthogonal basis set $\mathbf{H}\psi = E\mathbf{S}\psi$
- ψ arbitrary (right) solution of the GEE at energy E
- $\tilde{\psi}$ arbitrary left solution of the GEE at energy E
- ψ_d part of ψ in the device region
- $\psi_{i,j}$ part of ψ in the unit cell j of lead i
- $\phi_{(i,r),j}$ r -th mode of the lead i in the unit cell j
- $c_{(i,r)}$ Bloch factor of the eigenmode r in the lead i
- \mathbf{W} matrix present in the single-side form of GEE $\mathbf{W}\psi = 0$: $\mathbf{W} = \mathbf{H} - E\mathbf{S}$
- \mathbf{w}_d finite diagonal part of \mathbf{W} corresponding to the device
- \mathbf{w}_i finite diagonal part of \mathbf{W} corresponding to the unit cell of the lead i
- \mathbf{a}_i finite upper-diagonal part of \mathbf{W} corresponding to interactions between neighboring unit cells of the lead i
- \mathbf{b}_i finite lower-diagonal part of \mathbf{W} corresponding to interactions between neighboring unit cells of the lead i
- \mathbf{a}_{id} finite upper-diagonal part of \mathbf{W} corresponding to interactions between the device and the closest unit cell $j = 0$ of the lead i

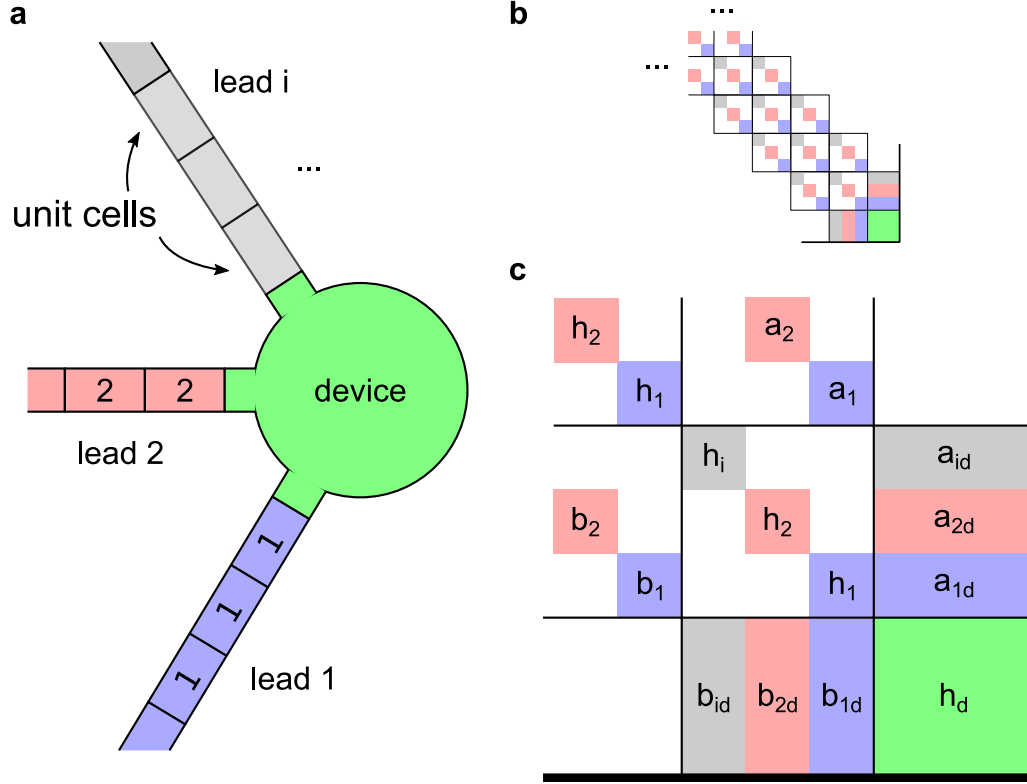


Figure 2.5 – Structure of a nanowire device Hamiltonian. (a) Schematic picture of the transport device setup. Several semi-infinite nanowires (leads) are connected to the same device. (b) A semi-infinite tri-block-diagonal Hamiltonian matrix of the setup is presented in panel (b) with a close-up of the device region in panel (c). The color of Hamiltonian blocks corresponds to leads' and device color on panel (a). The white color represents zeros in the Hamiltonian matrix.

- \mathbf{b}_{id} finite lower-diagonal part of \mathbf{W} corresponding to interactions between the device and the closest unit cell $j = 0$ of the lead i
- \mathbf{F}_i^\pm Bloch matrices for positive and negative modes in the lead i

Consider a ballistic setup where a nanoscale device connected to several semi-infinite periodic leads, Fig. 2.5(a). It is possible to express this setup in a semi-infinite Hamiltonian, Fig. 2.5(b) where ballistic charge carriers are the eigenstates of this Hamiltonian delocalized over multiple leads. Thus, the eigenstates of such Hamiltonian provide transport channels for the charge carriers.

As outlined previously, the Hamiltonian is expected to be in a tri-block-diagonal form where the main diagonal in Fig. 2.5(c) corresponds to interactions within unit cell of the leads \mathbf{h}_i , i is the lead index, and within the device region \mathbf{h}_d . The off-diagonal blocks couple leads and the

device region in the nearest-neighbor manner including “forward” coupling terms between neighboring leads \mathbf{a}_i and coupling of the closest lead unit cell to the device \mathbf{a}_{id} . Similarly, the backward coupling terms \mathbf{b}_i , \mathbf{b}_{id} are defined. Since Hamiltonian is Hermitian, $\mathbf{h} = \mathbf{h}^\dagger$, $\mathbf{a}^\dagger = \mathbf{b}$.

The nanowire device problem is the eigenvalue equation $\mathbf{H}\psi = E\psi$. An alternative way to write it is the following

$$(\mathbf{H} - E)\psi = (\mathbf{H} - E \cdot \mathbf{1})\psi = \mathbf{W}(E)\psi = 0. \quad (2.32)$$

The matrix $\mathbf{W}(E)$ is tri-block-diagonal as well:

$$\mathbf{W}\psi = \begin{bmatrix} \dots & \dots & \dots & \dots & \dots & \dots & \dots & \dots & \dots & \dots & \dots \\ \dots & \mathbf{w}_i & & & \mathbf{a}_i & & & & & & \\ \dots & & \mathbf{w}_2 & & \mathbf{a}_2 & & & & & & \\ \dots & & & \mathbf{w}_1 & & \mathbf{a}_1 & & & & & \\ \dots & \mathbf{b}_i & & & \mathbf{w}_i & & \mathbf{a}_i & & & & \\ \dots & & \mathbf{b}_2 & & \mathbf{w}_2 & & \mathbf{a}_2 & & & & \\ \dots & & & \mathbf{b}_1 & & \mathbf{w}_1 & & \mathbf{a}_1 & & & \\ \dots & & & & \mathbf{b}_i & & \mathbf{w}_i & & \mathbf{a}_{id} & & \\ \dots & & & & & \mathbf{b}_2 & & \mathbf{w}_2 & & \mathbf{a}_{2d} & \\ \dots & & & & & & \mathbf{b}_1 & & \mathbf{w}_1 & \mathbf{a}_{1d} & \\ \dots & & & & & & & \mathbf{b}_{id} & \mathbf{b}_{2d} & \mathbf{b}_{1d} & \mathbf{w}_d \end{bmatrix} \cdot \begin{bmatrix} \dots \\ \psi_{i,2} \\ \psi_{2,2} \\ \psi_{1,2} \\ \psi_{i,1} \\ \psi_{2,1} \\ \psi_{1,1} \\ \psi_{i,0} \\ \psi_{2,0} \\ \psi_{1,0} \\ \psi_d \end{bmatrix} = 0, \quad (2.33)$$

where $\mathbf{w} = \mathbf{h} - E$. The formal symbolic expression of the above equation consists of three types of equations:

$$\sum_i \mathbf{b}_{id}\psi_{i,0} = -\mathbf{w}_d\psi_d, \quad (2.34)$$

$$\mathbf{b}_i\psi_{i,1} + \mathbf{a}_{id}\psi_d = -\mathbf{w}_i\psi_{i,0} \quad (2.35)$$

and

$$\mathbf{b}_i\psi_{i,j+1} + \mathbf{a}_i\psi_{i,j-1} = -\mathbf{w}_i\psi_{i,j}, \quad j > 0. \quad (2.36)$$

The last type of equations correspond to bulk modes of lead i and are of the same form as Eq. 2.8. It is easy to show⁵ that above equations need $\sum_i N_i$ boundary conditions, N_i being number of rows (columns) in h_i . In the transport problems the boundary conditions are amplitudes of the leads' modes. Thus the next step is to consider leads separately.

⁵For example, specify all $\psi_{i,0}$

Step 2: Find the lead modes

The lead modes are modes of an infinite 1D lead subject to periodic boundary conditions. To find them, one writes Eq. 2.36 for arbitrary integer j :

$$\mathbf{b}_i \phi_{i,j+1} + \mathbf{a}_i \phi_{i,j-1} = -\mathbf{w}_i \phi_{i,j}, \quad j \in \mathbb{Z}. \quad (2.37)$$

Then, the Bloch ansatz is written from Eq. 2.9:

$$\phi_{i,j+1} = c_i \phi_{i,j} : \quad (\mathbf{b}_i c_i + \mathbf{a}_i c_i^{-1} + \mathbf{w}_i) \phi_{i,j} = 0 \quad . \quad (2.38)$$

The above is a quadratic eigenvalue equation with eigenvalues $c_{(i,r)}$ and eigenvectors $\phi_{(i,r),j}$. Since several modes are expected to fulfill the above equation index r is used to enumerate the solutions⁶. Eq. 2.38 can be reduced to a generalized eigenvalue equation for double-size matrices written as

$$\begin{bmatrix} 0 & \mathbf{1} \\ \mathbf{a}_i & \mathbf{w}_i \end{bmatrix} \cdot \begin{bmatrix} \phi_{(i,r),j} \\ \phi_{(i,r),j+1} \end{bmatrix} = c_{(i,r)} \begin{bmatrix} \mathbf{1} & 0 \\ 0 & -\mathbf{b}_i \end{bmatrix} \cdot \begin{bmatrix} \phi_{(i,r),j} \\ \phi_{(i,r),j+1} \end{bmatrix}. \quad (2.39)$$

The latter can be solved with standard routines (ZGGEV in LAPACK[54], for example). A right-hand side matrix can be eliminated if \mathbf{b}_i^{-1} exists and finite:

$$\begin{bmatrix} 0 & \mathbf{1} \\ -\mathbf{b}_i^{-1} \mathbf{a}_i & -\mathbf{b}_i^{-1} \mathbf{w}_i \end{bmatrix} \cdot \begin{bmatrix} \phi_{(i,r),j} \\ \phi_{(i,r),j+1} \end{bmatrix} = c_{(i,r)} \begin{bmatrix} \phi_{(i,r),j} \\ \phi_{(i,r),j+1} \end{bmatrix}. \quad (2.40)$$

The matrix on the left of above equation is called the *transfer matrix*, described in Ref. [55].

Provided the size of matrices $\mathbf{w}_i, \mathbf{a}_i, \mathbf{b}_i$ is equal to N_i there will be $2N_i$ possible (right) eigenstates $\phi_{(i,r),j}$ with (right) eigenvalues $c_{(i,r)}$. If either of the matrices $\mathbf{a}_i, \mathbf{b}_i$ has a zero eigenvalue, corresponding eigenstates will also be eigenstates of Eq. 2.38 with diverging $c_{(i,r)} = 0, \infty$ eigenvalues. For a Hermitian matrix W growing and decaying modes are closely related: if c is an eigenvalue of a decaying mode $|c| < 1$ then $(c^*)^{-1}$ is an eigenvalue corresponding to a growing mode⁷ $|(c^*)^{-1}| > 1$. Thus, the number of growing and decaying modes is exactly equal.

The propagating states $|c| = 1$ can also be split into two equal groups: incoming and outgoing. The incoming modes have a positive group velocity and transfer charge carriers to the lead while outgoing modes transfer charge carriers away from the lead. The group velocity $v_{(i,r)}$ (energy units) is defined by the pseudomomentum k , $c_{(i,r)} = e^{ik}$, as

$$v_{(i,r)} = \frac{\partial E_{(i,r)}}{\partial k} = \phi_{(i,r)}^\dagger \frac{\partial \mathbf{H}_i(k)}{\partial k} \phi_{(i,r)} = \phi_{(i,r)}^\dagger \left(-i\mathbf{a}e^{-ik} + i\mathbf{b}e^{ik} \right) \phi_{(i,r)}, \quad (2.41)$$

⁶ The lead index i and the mode index r can be combined into a single index (i, r) : the lead Hamiltonian matrices \mathbf{h}_i in the matrix in Fig. 2.5 can be merged into a single (large) block equivalent to a single lead connected to the device. The brackets are used to emphasize this fact.

⁷ To derive it, apply a Hermitian conjugate to Eq. 2.38 and use the fact that “left” and “right” eigenvalues are same, see appendix A.1.

or,

$$v_{(i,r)} = i\phi_{(i,r)}^\dagger (\mathbf{b}c_{(i,r)} - \mathbf{a}c_{(i,r)}^*) \phi_{(i,r)}. \quad (2.42)$$

The number of incoming modes $v_i < 0$ is equal to the number of outgoing modes $v_i > 0$.

The group velocity calculated using Eq. 2.42 for non-propagating modes is zero. To show it consider ϕ_n , c_n and ϕ_m and c_m is an arbitrary pair of solutions of Eq. 2.38 (the lead index i and the unit cell index j are omitted):

$$\begin{cases} (\mathbf{b}c_n + \mathbf{a}c_n^{-1} + \mathbf{w})\phi_n = 0 \\ (\mathbf{b}c_m + \mathbf{a}c_m^{-1} + \mathbf{w})\phi_m = 0. \end{cases} \quad (2.43)$$

Multiplying the first equation to the left by ϕ_m^\dagger and the second one by ϕ_n^\dagger yields

$$\begin{cases} \phi_m^\dagger (\mathbf{b}c_n + \mathbf{a}c_n^{-1} + \mathbf{w})\phi_n = 0 \\ \phi_n^\dagger (\mathbf{b}c_m + \mathbf{a}c_m^{-1} + \mathbf{w})\phi_m = 0. \end{cases} \quad (2.44)$$

Provided H is Hermitian, the conjugate operation applied to the second equation results in

$$\phi_m^\dagger (\mathbf{b}c_m^{-1*} + \mathbf{a}c_m^* + \mathbf{w})\phi_n = 0. \quad (2.45)$$

Subtracting the first equation in the system from the above eliminates \mathbf{w}

$$\phi_m^\dagger \mathbf{b}\phi_n (c_m^{-1*} - c_n) + \phi_m^\dagger \mathbf{a}\phi_n (c_m^* - c_n^{-1}) = 0. \quad (2.46)$$

Finally, multiplying the above equation by $c_n c_m^*$ yields

$$\begin{aligned} \phi_m^\dagger \mathbf{b}\phi_n \cdot c_n (1 - c_n c_m^*) + \phi_m^\dagger \mathbf{a}\phi_n \cdot c_m^* (c_m^* c_n - 1) &= 0 \Leftrightarrow \\ \left[\phi_m^\dagger \mathbf{b}\phi_n \cdot c_n - \phi_m^\dagger \mathbf{a}\phi_n \cdot c_m^* \right] \cdot (1 - c_n c_m^*) &= 0. \end{aligned} \quad (2.47)$$

For $n = m$ the quantity in square brackets is the group velocity up to i multiplier

$$v_{(i,r)} (1 - |c_{(i,r)}|^2) = 0. \quad (2.48)$$

Thus, all modes having $|c| \neq 1$ do not transmit charge carriers since the corresponding group velocity $v_{(i,r)} = 0$. A generalized velocity v_{nm} will be used further. It is defined as

$$v_{nm} = i\phi_m^\dagger (\mathbf{b} \cdot c_n - \mathbf{a} \cdot c_m^*) \phi_n. \quad (2.49)$$

v_{nm} has a property

$$v_{nm} (1 - c_n c_m^*) = 0, \quad (2.50)$$

where both n and m identify modes, i.e. contain lead i and mode r indices.

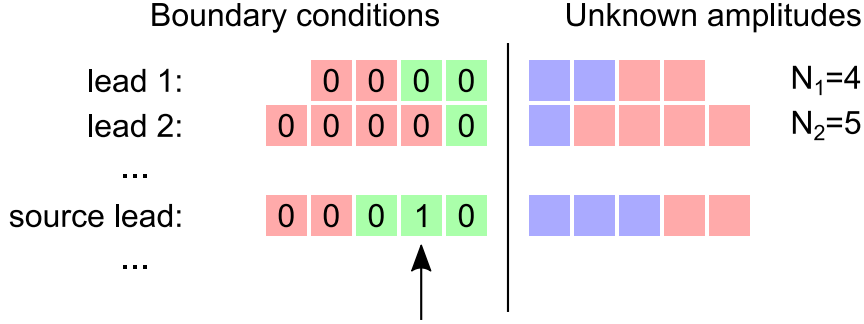


Figure 2.6 – Boundary conditions and unknown amplitudes in the transport setup. Each square represents an amplitude of the mode r in the lead i A_i^r . The entire row represents a wavefunction in one of the leads: it consists of incoming modes (green), outgoing modes (blue) and growing/decaying modes (red). The total number of amplitudes needed to describe the wavefunction in the lead i is equal to $2N_i$. In the transport setup half of all amplitudes are fixed (left-hand side) while the other half is calculated. The source of electrons is represented by a sole incoming mode represented by the unity amplitude indicated by the arrow.

To sum up, a generic wavefunction of the lead i in the unit cell j , $\psi_{i,j}$, is expressed as a sum of $2N_i$ eigenmodes with complex amplitudes $A_{(i,r)}$

$$\psi_{i,j} = \sum_{r=1}^{2N_i} A_{(i,r)} \cdot (c_{(i,r)})^j \cdot \phi_{(i,r),0} = \sum_{\text{growing}, |c|>1} + \sum_{\text{decaying}, |c|<1} + \sum_{\text{incoming}, v>0} + \sum_{\text{outgoing}, v<0} . \quad (2.51)$$

In the transport setup some of the $A_{(i,r)}$ are boundary conditions, while, the other ones are unknown. Specifically, all growing modes are discarded $A_{(i,r)>} = 0$: they diverge in the leads, thus, lack physical meaning. To be able to calculate transmission probabilities, one assumes that there is a single positive mode $(i,r)+_s$ from the source lead with a unity amplitude $A_{(i,r)+_s} = 1$. Otherwise all other positive modes are absent: $A_{(i,r)+} = 0$, $(i,r)+ \neq (i,r)+_s$. It is easy to see that the number of amplitudes defined so far is exactly equal to required number of boundary conditions $\sum_i N_i$, see Fig. 2.6. Thus, it is possible to derive another half of amplitudes for decaying $A_{(i,r)<}$ and outgoing $A_{(i,r)-}$ modes.

Since all amplitudes A_i^r are split into two equal groups, the boundary conditions and the unknown amplitudes in Fig. 2.6, it is also possible to split the wavefunction $\psi_{i,j}$ into two terms

$$\psi_{i,j} = \psi_{i,j}^+ + \psi_{i,j}^- , \quad (2.52)$$

where each term groups half of the sum from Eq. 2.51

$$\psi_{i,j}^+ = \sum_{\text{growing}, |c|>1} + \sum_{\text{incoming}, v>0} = \sum_r c_{(i,r)}^j \phi_{(i,r),0} = (\mathbf{F}_i^+)^j \cdot \psi_{i,0}^+ ,$$

$$\psi_{i,j}^- = \sum_{\text{decaying}, |c| < 1} + \sum_{\text{outgoing}, v < 0} = \sum_r c_{(i,r)}^j \phi_{(i,r),0} = (\mathbf{F}_i^-)^j \cdot \psi_{i,0}^-.$$

The quantities \mathbf{F} are the Bloch matrices having the same combined spectrum as the transfer matrix in Eq. 2.40

$$\mathbf{F}_i^+ = \sum_{r \in \{+, +\}} \phi_{(i,r),j} \cdot c_{(i,r)} \cdot \tilde{\phi}_{(i,r),j}^\dagger, \quad \mathbf{F}_i^- = \sum_{r \in \{<, -\}} \phi_{(i,r),j} \cdot c_{(i,r)} \cdot \tilde{\phi}_{(i,r),j}^\dagger. \quad (2.53)$$

The row vector $\tilde{\phi}_{(i,r),j}^\dagger$ is reciprocal to lead modes $\tilde{\phi}_{(i,r'),j}^\dagger \cdot \phi_{(i,r'),j} = \delta_{r,r'}$ provided the states selected form a complete basis (proof omitted). It is easy to show that the above definitions do not depend on the chosen j . The powers of Bloch matrices are simply

$$(\mathbf{F}_i^\pm)^p = \sum_{r \in \{...\}} \phi_{(i,r),j} \cdot c_{(i,r)}^p \cdot \tilde{\phi}_{(i,r),j}^\dagger. \quad (2.54)$$

The Bloch matrices satisfy the following matrix equation:

$$\mathbf{b}_i \mathbf{F}_i^\pm + \mathbf{a}_i (\mathbf{F}_i^\pm)^{-1} + \mathbf{w}_i = 0, \quad (2.55)$$

A final note on the Bloch matrices is related to the velocity expression in Eq. 2.49 which can be re-written as:

$$v_{nm} = i \phi_m^\dagger \left(\mathbf{b}_i \mathbf{F}_i^+ - (\mathbf{F}_i^+)^{\dagger} \mathbf{a}_i \right) \phi_n, \quad n, m \in \{+\}, \quad (2.56)$$

$$v_{nm} = i \phi_m^\dagger \left(\mathbf{b}_i \mathbf{F}_i^- - (\mathbf{F}_i^-)^{\dagger} \mathbf{a}_i \right) \phi_n, \quad n, m \in \{-\}. \quad (2.57)$$

The expression includes self-energies of the lead i defined as

$$\Sigma_i = \mathbf{b}_i \mathbf{F}_i^-. \quad (2.58)$$

The quantity $i \left(\mathbf{b}_i \mathbf{F}_i^- - (\mathbf{F}_i^-)^{\dagger} \mathbf{a}_i \right) = i \left(\Sigma_i - \Sigma_i^\dagger \right)$ is the gamma-function

$$\Gamma_i = i \left(\Sigma_i - \Sigma_i^\dagger \right), \quad v_{nm} = \phi_m^\dagger \Gamma_i \phi_n. \quad (2.59)$$

Step 3: Solve the nanowire device problem

The next step is to determine all $\psi_{i,j}^-$ for given $\psi_{i,j}^+$ by solving the corresponding system of linear equations. To demonstrate it, Eqs. 2.34,2.35 are written using Eqs. 2.52 for $j = 0$

$$\sum_i \mathbf{b}_{id} \psi_{i,0}^- + \mathbf{w}_d \psi_d = - \sum_i \mathbf{b}_{id} \psi_{i,0}^+, \quad (2.60)$$

$$(\mathbf{b}_i \mathbf{F}_i^- + \mathbf{w}_i) \psi_{i,0}^- + \mathbf{a}_{id} \psi_d = -(\mathbf{b}_i \mathbf{F}_i^+ + \mathbf{w}_i) \psi_{i,0}^+ = \mathbf{a}_i (\mathbf{F}_i^+)^{-1} \psi_{i,0}^+, \quad (2.61)$$

where the right-hand side of the second equation was simplified using Eq. 2.55. Explicitly,

$$\begin{bmatrix} \mathbf{b}_i \mathbf{F}_i^- + \mathbf{w}_i & & & \mathbf{a}_{id} \\ & \mathbf{b}_2 \mathbf{F}_2^- + \mathbf{w}_2 & & \mathbf{a}_{2d} \\ & & \mathbf{b}_1 \mathbf{F}_1^- + \mathbf{w}_1 & \mathbf{a}_{1d} \\ \mathbf{b}_{id} & \mathbf{b}_{2d} & \mathbf{b}_{1d} & \mathbf{w}_d \end{bmatrix} \cdot \begin{bmatrix} \psi_{i,0}^- \\ \psi_{2,0}^- \\ \psi_{1,0}^- \\ \psi_d \end{bmatrix} = \begin{bmatrix} \mathbf{a}_i (\mathbf{F}_i^+)^{-1} \psi_{i,0}^+ \\ \mathbf{a}_2 (\mathbf{F}_2^+)^{-1} \psi_{2,0}^+ \\ \mathbf{a}_1 (\mathbf{F}_1^+)^{-1} \psi_{1,0}^+ \\ - \sum_i \mathbf{b}_{id} \psi_{i,0}^+ \end{bmatrix}. \quad (2.62)$$

The left-hand-side matrix is the inverse of the *Green's function* \mathbf{G} of the scattering region. It includes lead self-energies Σ_i from Eq. 2.58. This result is the same as the one presented in Ref. [53] Eq. 19, except the right-hand-side term $\mathbf{Q}_0 c_0(+)$ with \mathbf{Q}_0 defined in Eq. 14 of the above reference. There, the lead-device matrices \mathbf{a}_{id} , \mathbf{b}_{id} are implicitly assumed to be projected versions of \mathbf{a}_i \mathbf{b}_i such that

$$\mathbf{a}_{id} = \mathbf{a}_i \cdot \mathbf{p}_i, \quad \mathbf{b}_{id} = \mathbf{q}_i \cdot \mathbf{b}_i \quad (2.63)$$

where \mathbf{p}_i , \mathbf{q}_i are rectangular projection matrices, $\mathbf{p}_i = \mathbf{q}_i^\dagger$. Such notation change substituted into Eq. 2.61 yields

$$\mathbf{p}_i \psi_d = (\mathbf{F}_i^+)^{-1} \psi_{i,0}^+ + (\mathbf{F}_i^-)^{-1} \psi_{i,0}^- = \psi_{i,-1}, \quad (2.64)$$

where $\psi_{i,-1}$ is the lead mode as if the lead is continued to $j = -1$. Collecting above two substitutions into Eq. 2.60 or Eq. 2.34 and replacing $\psi_{i,0}$ in favor of $\psi_{i,-1}$ by means of Bloch matrices Eq. 2.52 results in the following

$$\sum_i \mathbf{q}_i \mathbf{b}_i \psi_{i,0} = \dots = \sum_i \mathbf{q}_i \mathbf{b}_i \left[\mathbf{F}_i^+ \psi_{i,-1}^+ - \mathbf{F}_i^- \psi_{i,-1}^+ + \mathbf{F}_i^- \mathbf{p}_i \psi_d \right] = -\mathbf{w}_d \psi_d. \quad (2.65)$$

In the above equation, $\psi_{i,-1}^+$ play the role of boundary conditions, similarly to $\psi_{i,0}^+$ in Eq. 2.62, while ψ_d is an unknown. By moving ψ_d to the left and using self-energies from Eq. 2.58 a simpler form of Eq. 2.62 is recovered

$$\left[\mathbf{w}_d + \sum_i \mathbf{q}_i \Sigma_i \mathbf{p}_i \right] \psi_d = \sum_i \mathbf{q}_i \mathbf{b}_i (\mathbf{F}_i^+ - \mathbf{F}_i^-) \psi_{i,-1}^+. \quad (2.66)$$

Similarly to Eq. 2.62, the left-hand-side matrix is the inverse of the Green's function matrix \mathbf{G}

$$\mathbf{G} = \left[\mathbf{w}_d + \sum_i \mathbf{q}_i \Sigma_i \mathbf{p}_i \right]^{-1} = \left[\mathbf{w}_d + \sum_i \mathbf{b}_{id} \mathbf{b}_i^{-1} \Sigma_i \mathbf{a}_i^{-1} \mathbf{a}_{id} \right]^{-1}. \quad (2.67)$$

Note that usually \mathbf{q}_i , \mathbf{p}_i are dropped from the above expression assuming the former ones are simple matrices consisting of zeros and ones. This creates unnecessary confusion especially when considering real implementations: it usually requires to “include” a unit cell of each lead into the scattering region matrix \mathbf{w}_d and to use special indexing rules.

Step 4: Calculate transmission probabilities

To calculate transmission probabilities one takes a special form of the right-hand-side vector in Eq. 2.62 or Eq. 2.66 in accordance with Fig. 2.6

$$\psi_{i,j}^+ = 0, \quad i \neq i_s; \quad \psi_{i,j}^+ = \phi_{(i,r+)_s,j}, \quad i = i_s, \quad (2.68)$$

where the incoming “+” mode r_s of the lead i_s is taken as a source of electrons. The charge carriers scatter into an outgoing drain mode $(i, r-)_d$ of the lead i_d with an amplitude

$$A_{(i,r+)_s \rightarrow (i,r-)_d} = \tilde{\phi}_{(i,r-)_d,j}^\dagger \psi_{i_d,j}^-. \quad (2.69)$$

For $i_d \neq i_s$, Eq. 2.64 yields $\mathbf{p}_{i_d} \psi_d = \psi_{i_d,-1} = \psi_{i_d,-1}^-$, thus, Eq. 2.66 results in the following amplitude

$$A_{(i,r+)_s \rightarrow (i,r-)_d} = \tilde{\phi}_{(i,r-)_d,-1}^\dagger (\mathbf{p}_{i_d} \mathbf{G} \mathbf{q}_{i_s}) \mathbf{b}_{i_s} (\mathbf{F}_{i_s}^+ - \mathbf{F}_{i_s}^-) \phi_{(i,r+)_s,-1}. \quad (2.70)$$

Note that $j = -1$ is taken: while the amplitude A generally depends on the unit cell j where the above projection is performed, its magnitude is constant for the propagating modes. The amplitude of reflected waves can be found in a similar fashion. Reflected modes belong to the source electrode, thus Eq. 2.64 reads

$$\mathbf{p}_{i_s} \psi_d = \psi_{i_s,-1} = \psi_{i_s,-1}^- + \phi_{(i,r+)_s,-1}. \quad (2.71)$$

To derive the amplitude, the outgoing part of the wavefunction in the source $\psi_{i_s,-1}$ should be projected onto one of the outgoing states $\phi_{(i,r-)_s,-1}$

$$A_{(i,r+)_s \rightarrow (i,r-)_s} = \tilde{\phi}_{(i,r-)_s,-1}^\dagger (\mathbf{p}_{i_d} \mathbf{G} \mathbf{q}_{i_s}) \mathbf{b}_{i_s} (\mathbf{F}_{i_s}^+ - \mathbf{F}_{i_s}^-) \phi_{(i,r+)_s,-1} - \tilde{\phi}_{(i,r-)_s,-1}^\dagger \phi_{(i,r+)_s,-1} \quad (2.72)$$

Chapter 2. Methodology

Transmission and reflection probabilities are proportional to the absolute of the above amplitude squared:

$$t_{n \rightarrow m} = \frac{v_m}{v_n} |A_{n \rightarrow m}|^2 . \quad (2.73)$$

It is normalized by velocity and takes values from 0 to 1. The total transmission from the source to the drain lead includes the sum over incoming and outgoing modes in these leads

$$T_{i_s \rightarrow i_d} = \sum_{\substack{n \in \{(i, r+)\}_s, |c|=1 \\ m \in \{(i, r-)_d, |c|=1\}}} t_{n \rightarrow m} . \quad (2.74)$$

The above formulas together with Eq. 2.28 are sufficient to calculate a two-terminal resistance. It is instructive, however, to recover Caroli expression[56, 57] for the total transmission

$$T_{i_s \rightarrow i_d} = \text{Tr } \Gamma_{i_d} \mathbf{p}_{i_d} \mathbf{G} \mathbf{q}_{i_s} \Gamma_{i_s} \mathbf{p}_{i_s} \mathbf{G}^\dagger \mathbf{q}_{i_d} . \quad (2.75)$$

The above equation and Eq. 2.70 essentially use the same components: the Green's function \mathbf{G} and the gamma-functions Γ in the form of velocities v_n , see Eq. 2.59. The main issue, however, is that Eq. 2.70 together with Eq. 2.73 give a non-zero transmission probability for growing or decaying modes ϕ , $\tilde{\phi}$. Writing transmission probability explicitly yields

$$t_{n \rightarrow m} = \frac{v_m}{v_n} \cdot \tilde{\phi}_m^\dagger (\mathbf{p}_{i_d} \mathbf{G} \mathbf{q}_{i_s}) \mathbf{b}_{i_s} (\mathbf{F}_{i_s}^+ - \mathbf{F}_{i_s}^-) \phi_n \cdot \phi_n^\dagger (\mathbf{b}_{i_s} (\mathbf{F}_{i_s}^+ - \mathbf{F}_{i_s}^-))^\dagger (\mathbf{p}_{i_d} \mathbf{G}^\dagger \mathbf{q}_{i_s}) \tilde{\phi}_m . \quad (2.76)$$

Above expression is zero if m denotes a decaying mode since $v_m = \phi_m^\dagger \Gamma_{i_d} \phi_m = 0$ in this case, see Eq. 2.50. It diverges, however, if ϕ_n is a growing mode: $v_n = 0$. A workaround is to consider a part of the above expression $\mathbf{b}_{i_s} (\mathbf{F}_{i_s}^+ - \mathbf{F}_{i_s}^-) \phi_n$

$$\begin{aligned} \mathbf{b}_{i_s} (\mathbf{F}_{i_s}^+ - \mathbf{F}_{i_s}^-) \phi_n &= (\mathbf{b}_{i_s} \mathbf{F}_{i_s}^+ - \Sigma_{i_s}) \phi_n = (\mathbf{b}_{i_s} \mathbf{F}_{i_s}^+ + i \Gamma_{i_s} - \Sigma_{i_s}^\dagger) \phi_n = \\ i \Gamma_{i_s} \phi_n + (\mathbf{b}_{i_s} \mathbf{F}_{i_s}^+ - \Sigma_{i_s}^\dagger) \phi_n &= i \Gamma_{i_s} \phi_n + (\mathbf{b}_{i_s} \mathbf{F}_{i_s}^+ - (\mathbf{F}_{i_s}^-)^\dagger \mathbf{a}_{i_s}) \phi_n . \end{aligned} \quad (2.77)$$

The operator in brackets multiplied by an incoming mode is always zero

$$\begin{aligned} (\mathbf{b}_{i_s} \mathbf{F}_{i_s}^+ - (\mathbf{F}_{i_s}^-)^\dagger \mathbf{a}_{i_s}) \phi_n &= \mathbf{1} (\mathbf{b}_{i_s} \mathbf{F}_{i_s}^+ - (\mathbf{F}_{i_s}^-)^\dagger \mathbf{a}_{i_s}) \phi_n = \\ \sum_{j \in \{-\}} \phi_j \tilde{\phi}_j^\dagger (\mathbf{b}_{i_s} \mathbf{F}_{i_s}^+ - (\mathbf{F}_{i_s}^-)^\dagger \mathbf{a}_{i_s}) \phi_n &= \sum_{j \in \{-\}} \phi_j \left[\tilde{\phi}_j^\dagger (\mathbf{b}_{i_s} \mathbf{F}_{i_s}^+ - (\mathbf{F}_{i_s}^-)^\dagger \mathbf{a}_{i_s}) \phi_n \right] = \\ \sum_{j \in \{-\}} \phi_j \left[\tilde{\phi}_j^\dagger (\mathbf{b}_{i_s} c_n - c_j^* \mathbf{a}_{i_s}) \phi_n \right] &= \sum_{j \in \{-\}} \phi_j v_{nj} = 0 \end{aligned} \quad (2.78)$$

since n is an incoming mode while j denotes outgoing and decaying modes such that $1 - c_n c_j^* \neq 0$ in Eq. 2.50⁸. Proceeding with Eq. 2.76,

$$t_{n \rightarrow m} = \frac{v_m}{v_n} \cdot \tilde{\phi}_m^\dagger(\mathbf{p}_{i_d} \mathbf{G} \mathbf{q}_{i_s}) \Gamma_{i_s} \phi_n \cdot \phi_n^\dagger \Gamma_{i_s}^\dagger (\mathbf{p}_{i_d} \mathbf{G}^\dagger \mathbf{q}_{i_s}) \tilde{\phi}_m. \quad (2.79)$$

Using Eqs. 2.59, 2.50 it is a rather simple task to prove that $\Gamma_{i_s} \phi_n = v_n \tilde{\phi}_n$. Canceling velocities v_n yields

$$t_{n \rightarrow m} = v_m \cdot \tilde{\phi}_m^\dagger(\mathbf{p}_{i_d} \mathbf{G} \mathbf{q}_{i_s}) \tilde{\phi}_n \cdot \phi_n^\dagger \Gamma_{i_s}^\dagger (\mathbf{p}_{i_d} \mathbf{G}^\dagger \mathbf{q}_{i_s}) \tilde{\phi}_m. \quad (2.80)$$

Also, $\Gamma_{i_d} \phi_m = v_m \tilde{\phi}_m$ such that

$$t_{n \rightarrow m} = \tilde{\phi}_m^\dagger(\mathbf{p}_{i_d} \mathbf{G} \mathbf{q}_{i_s}) \tilde{\phi}_n \cdot \phi_n^\dagger \Gamma_{i_s}^\dagger (\mathbf{p}_{i_d} \mathbf{G}^\dagger \mathbf{q}_{i_s}) \Gamma_{i_d} \phi_m. \quad (2.81)$$

The above expression produces the same exact values for transmission probabilities between propagating modes as Eq. 2.76. However, it has an advantage of all non-physical transmission probabilities between growing and decaying modes being zero:

$$\Gamma \phi = v \tilde{\phi} = 0, |c| \neq 1 \Leftrightarrow v = 0. \quad (2.82)$$

The total transmission becomes

$$\begin{aligned} T_{i_s \rightarrow i_d} &= \sum_{\substack{n \in \{(i, r+)\}_s, |c| = 1 \\ m \in \{(i, r-)_d, |c| = 1\}}} t_{n \rightarrow m} = \sum_{\substack{n \in \{(i, r+)\}_s \\ m \in \{(i, r-)_d\}}} t_{n \rightarrow m} = \\ &= \sum_{m, n} \tilde{\phi}_m^\dagger(\mathbf{p}_{i_d} \mathbf{G} \mathbf{q}_{i_s}) \tilde{\phi}_n \cdot \phi_n^\dagger \Gamma_{i_s}^\dagger (\mathbf{p}_{i_d} \mathbf{G}^\dagger \mathbf{q}_{i_s}) \Gamma_{i_d} \phi_m = \\ &= \sum_m \tilde{\phi}_m^\dagger(\mathbf{p}_{i_d} \mathbf{G} \mathbf{q}_{i_s}) \sum_n \tilde{\phi}_n \cdot \phi_n^\dagger \Gamma_{i_s}^\dagger (\mathbf{p}_{i_d} \mathbf{G}^\dagger \mathbf{q}_{i_s}) \Gamma_{i_d} \phi_m = \\ &= \sum_m \tilde{\phi}_m^\dagger(\mathbf{p}_{i_d} \mathbf{G} \mathbf{q}_{i_s}) \mathbf{1} \Gamma_{i_s}^\dagger (\mathbf{p}_{i_d} \mathbf{G}^\dagger \mathbf{q}_{i_s}) \Gamma_{i_d} \phi_m = \text{Tr} (\mathbf{p}_{i_d} \mathbf{G} \mathbf{q}_{i_s}) \Gamma_{i_s}^\dagger (\mathbf{p}_{i_d} \mathbf{G}^\dagger \mathbf{q}_{i_s}) \Gamma_{i_d}. \end{aligned} \quad (2.83)$$

The above is the Caroli expression from Eq. 2.75 up to $\Gamma_{i_s}^\dagger = \Gamma_{i_s}$ and a circular permutation of a matrix product under the trace operation.

Extension to non-orthogonal basis sets

Using the bracket notation, the Schroedinger equation is

$$\mathbf{H}|\rangle = E|\rangle, \quad (2.84)$$

⁸For a more rigorous proof one has to show that the basis $\{\phi_j\}$ is full and consider possible degeneracies of eigenvalues c in Eq. 2.50. The latter is done in Ref. [53] while the former is also required to construct Bloch matrices in Eq. 2.53

Chapter 2. Methodology

where $|i\rangle$ is an eigenstate, E is its energy. Consider a non-orthogonal basis $\{|i\rangle\}$ with a conjugate basis $\{|\tilde{i}\rangle\}$ such that $\langle \tilde{i} | i \rangle = \delta_{ij}$, δ is the Kronecker symbol. Expressing $|i\rangle$ in the above non-orthogonal basis set yields

$$|i\rangle = \mathbf{1} |i\rangle = \sum_i |i\rangle \langle \tilde{i} | i \rangle = \sum_i \psi_i |i\rangle . \quad (2.85)$$

Substituting it into Eq. 2.84 gives

$$\mathbf{H} \sum_i \psi_i |i\rangle = E \sum_i \psi_i |i\rangle , \quad (2.86)$$

which, in turn, has the matrix form

$$\left\langle j \left| \mathbf{H} \sum_i \psi_i |i\rangle \right| i \right\rangle = \sum_i \mathbf{H}_{ji} \psi_i = E \sum_i \mathbf{S}_{ji} \psi_i , \quad (2.87)$$

where $\mathbf{S}_{ji} = \langle j | i \rangle$ is the overlap matrix of the basis set and $\mathbf{H}_{ji} = \langle j | \mathbf{H} | i \rangle$ are Hamiltonian matrix elements. Both matrices are Hermitian. Looking back at Eq. 2.32 one extends it to include the overlap matrix

$$\mathbf{H}\psi = E\mathbf{S}\psi \Leftrightarrow (\mathbf{H} - E\mathbf{S})\psi = 0 \Rightarrow \boxed{\mathbf{W} = \mathbf{H} - E\mathbf{S}} . \quad (2.88)$$

In the case of $\mathbf{S} = \mathbf{1}$ the basis set is orthogonal. Thus, all quantities expressed in terms of the matrix \mathbf{W} , including the Caroli expression, remain valid.

On iterative algorithms and the imaginary energy

The implementation suggested in the present section consists of several steps:

1. Integrate out the pseudomomentum $k_{||}$ using the Fourier transform
2. For each lead:
 - (a) calculate modes at a given energy E by solving Eq. 2.38 or Eq. 2.39 or Eq. 2.40;
 - (b) calculate mode velocities using Eq. 2.42;
 - (c) group modes into positive and negative according to their velocities and Bloch coefficients;
 - (d) construct Bloch matrices \mathbf{F} , self-energies Σ and Gamma-functions Γ using Eqs. 2.53, 2.58, 2.59.
3. Calculate the Green's function \mathbf{G} using Eq. 2.67 and the total transmission using Eq. 2.75.

Common implementations, however, obtain lead self-energies without preceding steps using iterative solution of the corresponding matrix equation[58, 59, 52] equivalent to Eq. 2.55:

$$\mathbf{F} = (-\mathbf{w} - \mathbf{b}\mathbf{F})^{-1} \mathbf{a} \quad (2.89)$$

While more advanced techniques have been developed for iterative solutions of an above equation the most straightforward way to do it is to calculate the right-hand side iteratively:

$$\mathbf{F}_{i+1} = (-\mathbf{w} - \mathbf{b}\mathbf{F}_i)^{-1} \mathbf{a}, \quad (2.90)$$

where i denotes the iteration step with an arbitrary initial guess \mathbf{F}_0 . The quantity $\lim_{i \rightarrow +\infty} \mathbf{F}_i$ is expected to converge to one of the solutions of Eq. 2.55. The convergence criterion can be derived by considering a small deviation from the solution $\mathbf{F}_i = \mathbf{F}_{\text{sol}} + \Delta_i$ such that

$$\Delta_{i+1} = (-\mathbf{w} - \mathbf{b}[\mathbf{F}_{\text{sol}} + \Delta_i])^{-1} \mathbf{a} - \mathbf{F}_{\text{sol}} = (\mathbf{a}\mathbf{F}_{\text{sol}}^{-1} - \mathbf{b}\Delta_i)^{-1} \mathbf{a} - \mathbf{F}_{\text{sol}}. \quad (2.91)$$

To the first order in Δ it reads

$$\Delta_{i+1} \approx \mathbf{F}_{\text{sol}} \mathbf{a}^{-1} \mathbf{b} \Delta_i \mathbf{F}_{\text{sol}}. \quad (2.92)$$

The above, generally, does not vanish with increasing i unless all eigenvalues of \mathbf{F}_{sol} are less than one by modulus. Thus, there are two important properties of the iterative algorithm described above. First, the iterative algorithm does not converge if there is a single propagating state present at a given energy. Second, the iterative algorithm finds only one⁹ of the solutions \mathbf{F}^- . The convergence problem is solved by introducing an imaginary part to the energy $E - i\eta$ in Eqs. 2.32, 2.88 such that the resulting matrix is no longer Hermitian $\mathbf{W} \neq \mathbf{W}^\dagger$ and propagating states start growing or decaying. To be consistent, however, the perturbation is required to transform outgoing states into decaying ones. To show that it is indeed the case, consider a perturbation to Eq. 2.38

$$([\mathbf{b} + \beta][c + \Delta c] + [\mathbf{a} + \alpha][c + \Delta c]^{-1} + [\mathbf{w} + \omega])[\phi + d\phi] = 0, \quad (2.93)$$

where α, β, ω are small deviations from the corresponding matrix blocks, $\alpha^\dagger = -\beta$, $\omega^\dagger = -\omega$. Δc and $d\phi$ are small perturbations of eigenvalues and eigenvectors respectfully. The above equation in the first order of the small parameter reads

$$(\mathbf{b}c + \mathbf{a}c^{-1} + \mathbf{w})d\phi + \left(\mathbf{b}\Delta c - \mathbf{a}\frac{\Delta c}{c^2}\right)\phi + (\beta c + \alpha c^{-1} + \omega)\phi = 0. \quad (2.94)$$

Following the usual procedure for the development of the perturbation theory one multiplies the above equation by ϕ^\dagger from the left side. Provided ϕ is a propagating state $c^* = c^{-1}$ the first term becomes zero. Thus,

$$\Delta c = -\frac{\phi^\dagger(\beta c + \alpha c^{-1} + \omega)\phi}{\phi^\dagger(\mathbf{b} - \mathbf{a}/c^2)\phi} = -ic\frac{\phi^\dagger(\beta c + \alpha c^{-1} + \omega)\phi}{\nu}, \quad (2.95)$$

⁹To find \mathbf{F}^+ one has to iterate an equivalent (reverse) equation $\mathbf{F} = -\mathbf{b}^{-1}(\mathbf{w} + \mathbf{a}\mathbf{F}^{-1})$

where v is the group velocity defined in Eq. 2.42. For orthogonal basis sets, $\alpha = \beta = 0$ and $\omega = i\eta\mathbf{1}$ such that

$$\Delta c = c \frac{\eta}{v} . \quad (2.96)$$

Provided $\eta > 0$, $v < 0$, the sum $|c + \Delta c| < 1$ i.e. outgoing states become decaying ones. This argument also holds for non-orthogonal basis sets provided all eigenvalues of an overlap matrix \mathbf{S} in Eq. 2.88 are greater than zero.

To summarize this section, the Green's function method allows calculation of transmission probabilities and electrical conductivity in a multi-terminal device configuration provided proper boundary conditions and a tight-binding single-particle Hamiltonian.

2.2.2 Transport of electron spin

The charge carriers in solids carry not only charges but also magnetic moments (spins). The Green's function method described previously can also be applied to calculating spin transport properties and more. To do that, slight modifications of Eq. 2.75 are necessary.

Consider the wavefunction of the outgoing wave in the lead i to be $\psi_{i,j}^-$, j is the index of a unit cell. Provided a spin (or any other quantity) operator is \mathbf{O} , the expectation value of the operator in the unit cell j is

$$o(j) = \psi_{i,j}^{-\dagger} \mathbf{O} \psi_{i,j}^- . \quad (2.97)$$

Does $o(j)$ indeed depend on the unit cell j ? The general answer is yes. To show it, one writes the above expression as an explicit function of j using Eq. 2.53:

$$o(j) = \sum_{r,r'} c_{(i,r)}^{j*} c_{(i,r')}^j \phi_{(i,r),0}^\dagger \mathbf{O} \phi_{(i,r'),0}^- = \sum_{r,r'} \left(c_{(i,r)}^* c_{(i,r')} \right)^j \phi_{(i,r),0}^\dagger \mathbf{O} \phi_{(i,r'),0}^- . \quad (2.98)$$

The complex phase of $c_{(i,r)}^* c_{(i,r')}$ is, generally, arbitrary for $r \neq r'$. Thus, its mean value over j is zero. The mean value of quantity \mathbf{O} becomes

$$\langle o \rangle = \sum_r |c_{(i,r)}|^2 \phi_{(i,r),0}^\dagger \mathbf{O} \phi_{(i,r),0}^- . \quad (2.99)$$

For decaying modes $|c_{(i,r)}| < 1$, thus, $|c_{(i,r)}|^{2j} \rightarrow 0$, $j \rightarrow \infty$. This has a simple physical interpretation: away from the scattering region there are no decaying modes, thus, the summation can be performed over propagating states only. The current of quantity \mathbf{O} transported into the drain lead may be introduced in a fashion similar to Landauer-Buttiker current Eq. 2.29

$$j_O = \frac{1}{h} \int dE \sum_{m,n} t\{O\}_{m \rightarrow n}(E) \cdot f'(E) , \quad (2.100)$$

where

$$t\{O\}_{m \rightarrow n}(E) = t_{m \rightarrow n}(E) \cdot \phi_n^\dagger \mathbf{O} \phi_n, \quad (2.101)$$

with the corresponding notation taken from Eq. 2.81. The quantity in Eq. 2.101 may be viewed as a transmission “colored” by the operator \mathbf{O} in the drain lead. In the case of spin $\mathbf{O} = \frac{1}{2} \mathbf{s}_z$, the above quantity takes values in the interval $[-1/2, 1/2]$ depending both on the transparency of the device and polarization of the spin, thus, having properties of a spin current. Provided the lead Hamiltonian is scalar-relativistic, however, it is more convenient to split the corresponding lead matrices into two non-interacting parts in spin space \mathbf{W}_\uparrow and \mathbf{W}_\downarrow and to use the usual Caroli formula.

The quantity $\phi_n^\dagger \mathbf{O} \phi_n$ does not necessarily need to be an operator in brackets: it can be any kind of a “coloring” function. For example, the valley polarization v_n considered further can be presented as

$$v_n = \text{sgn Arg } \phi_n^\dagger \mathbf{F}^- \phi_n.$$

2.2.3 Optimizing computational costs with the Green’s function method

The device in the previous sections was accounted for via a finite-size matrix \mathbf{w}_d . The most computationally demanding step for calculating transport properties, however, is the inversion in Eq. 2.67 to obtain the Green’s function. The latter has the same shape as \mathbf{w}_d . Thus, to improve the performance of DFT for (non-equilibrium) Green’s functions (NEGF) one has to optimize calculations involving the device matrix \mathbf{w}_d .

The supercell approach

In the simplest case, the device is a defect in otherwise periodic structure: for example, a line defect in Fig. 2.4(b). The defect perturbs the structure locally as can be seen, for example, by calculating deviations from equilibrium atomic positions. The latter typically decays with the distance to the defect but it is never exactly zero. Thus, one has to make a choice and to consider a region in the vicinity of the defect (the scattering region) where lattice deformations are important for a given problem. The lattice outside this region is assumed to be unperturbed. Even if lattice deformations can be neglected completely there are local perturbations of charge and potential distributions affecting charge carrier transport. The scattering region should be large enough to include important perturbations.

The size of the scattering region is a simple numeric parameter which can be converged. Thus, a typical work flow would involve calculations with larger and larger scattering regions until the desired error in quantities of interest is reached. Typically, among the latters are the charge carrier transmission probability, the electronic band structure of the device, relaxed atomic

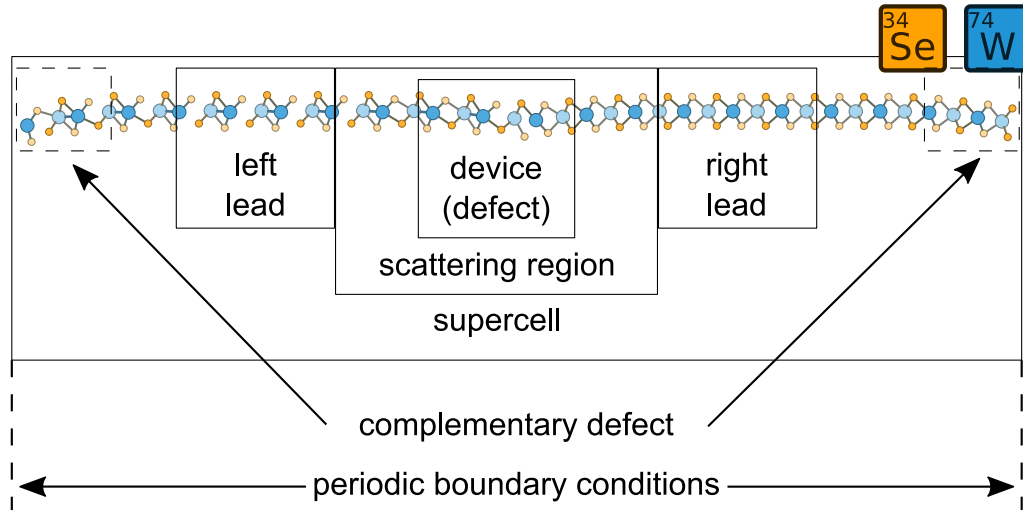


Figure 2.7 – A supercell model for the transport calculations. A line defect in a monolayer 2H-WSe₂ is shown as an example (side view). The key regions in the transport setup are indicated.

positions, or other parameters.

The NEGF DFT generally requires much more computational resources than conventional DFT in periodic boundary conditions (PBC) for the same number of atoms. There are two basic reasons for such behavior:

1. Compared to the conventional DFT, the NEGF DFT treats the energy E as an external parameter and requires a significant amount of resources to perform integrations over the energy.
2. The solution of the Poisson's equation for the electrostatic potential ϕ : $\Delta\phi = \rho$ (ρ is the charge density) is less computationally expensive than the one under fixed boundary conditions corresponding to left and right leads.

Thus, one would prefer to employ PBC DFT for large calculations. It becomes possible through the *supercell* approach.

The supercell is a structure containing the scattering region together with an additional amount of bulk leads. The periodic boundary conditions in this case are satisfied if bulk structures of the leads are exactly the same (it is usually the case for inversion-symmetric materials). Otherwise an additional complementary defect has to be introduced as shown in Fig. 2.7. The size of the supercell is roughly twice that of the scattering region such that the 2 defects do not interact. The supercell should also be large enough to allow the lead material away from the defects to have bulk-like electronic and structural properties.

The supercell approach can be used to replace “expensive” NEGF DFT at various computation

2.3. Simulating scanning tunneling microscopy (STM) images

stages. It is typically used at the first stage when relaxing the atomic structure of the device. The second stage is to calculate the self-consistent Hamiltonian of the defect where the supercell approach can also be applied. Specifically, the large Hamiltonian of the supercell is cut into corresponding matrices related to device \mathbf{h}_d , leads \mathbf{h}_i and their interaction \mathbf{a}_{id} . At the last stage, the above matrices are used to calculate transmission probabilities and currents.

Model Hamiltonians

The model Hamiltonians are constructed in a way to have a minimum possible number of electronic basis functions, yet, to capture the relevant physics in a given system. An example is a tight-binding model of graphene including two π orbitals only. The reduced number of bands allows calculation of charge carrier transport properties in larger systems or systems with a larger periodicity. On the other hand, model Hamiltonians are not universal: they are usually constrained to an atomic structure of a bulk material, thus, they may fail to describe the device region containing surfaces, defects, etc.

One of the most popular ways to create a model Hamiltonian is to express selected bands in terms of maximally localized Wannier functions[60]. The method allows construction of a tight-binding Hamiltonian from the *ab-initio* electronic structure of the material. The tight-binding Hamiltonian is written in localized basis set of orthogonal molecular orbitals of the solid. Provided a good initial guess, the “wannierization” procedure makes the basis set as local as possible, thus, reducing the number of neighbors of each orbital to, ideally, nearest neighbors only.

2.3 Simulating scanning tunneling microscopy (STM) images

STM is a very common atomic microscopy technique where the surface of a material is probed by an atomic-sized tip in the real space. The resolution of the method approaches the size of an atom which is a major advantage over, for example, optical methods. The STM images are used to identify atomic structure and electronic properties of 2D materials and surfaces. In the present work, several point defects were identified by comparing experimental and simulated STM images. Following is a brief introduction into the method.

The key object in STM is the metallic tip scanning the surface of a material. The tip can move in the surface plane (an angstrom-scale displacement is typically done by piezoelectric crystals) and adjusts its height according to the underlying surface structure. This is possible via the feedback mechanism provided by the tunneling current value depends exponentially on the tip vertical coordinate. The characteristic length is of the order of an interatomic distance and

is defined by the work function of an electron ϕ

$$\lambda = \frac{\hbar}{8m\phi} \sim 1\text{\AA}, \quad (2.102)$$

where m is the electron mass.

The practical realization of an STM microscope is rather simple and can be done with a reasonable effort from commonly available electronic components. The main idea is to supply the voltage bias between the sample and an atomically sharp tip, measure the small tunneling current I and to displace the tip by adjusting the voltage bias to piezoelectric crystals V_{piezo} . By keeping I constant one recovers V_{piezo} as a function of the spacial position of the tip which gives a topographic image of the surface in the “constant current” mode.

To simulate STM images by *ab-initio* methods one essentially needs to perform a transport simulation of the tunneling current. However, since the tip and the sample are only weakly coupled it is possible to perform the perturbation theory with a small sample-tip coupling operator \mathbf{M} , the Tersoff-Hamann approach[61]:

$$I = \frac{2\pi e}{\hbar} \sum_{\mu,\nu} f(E_\mu - E_F) (1 - f(E_\nu + eV - E_F)) |\langle \mu | \mathbf{M} | \nu \rangle|^2 \delta(E_\mu - E_\nu), \quad (2.103)$$

where V is the voltage applied, E_F is the Fermi level, f is Fermi distribution function and the sum is taken over tip states μ and sample states ν . As a further assumption, one sets $\langle \mu | \mathbf{M} = \langle r |$ where the right-hand-side is the eigenstate of a coordinate operator (i.e. delta-function in real space). This is approximately valid for tips with a single atom and a single s orbital at the Fermi level. The resulting expression at zero temperature becomes proportional to the local density of states integrated over the voltage bias

$$I \sim \int_{E_F - eV}^{E_F} dE \sum_{\nu} |\langle r | \nu \rangle|^2 \delta(E_\nu - E). \quad (2.104)$$

Calculation of the above quantity is typically implemented in modern DFT codes as a summation in the reciprocal space where the Hamiltonian is diagonalized on the k -point grid, and states which match the energy region are added to the total weight. This method usually provides a reasonable zeroth approximation and is commonly used in *ab-initio* studies solely or in comparison with experimental data. More advanced methods such as an aforementioned NEGF transport simulation provide quantitative improvements to the images simulated[62] at

2.3. Simulating scanning tunneling microscopy (STM) images

a considerably higher computational cost.

3 Spin and valley transport across regular line defects in semiconducting TMDs

As introduced previously, the monolayer 2H-TMDs (MX_2 , $M = \text{Mo, W}$, $X = \text{S, Se, Te}$) are 2D semiconducting materials for novel applications in electronics and beyond. So far these materials have been considered mostly in the context of conventional electronics[15, 14, 63] and photovoltaics[64, 20] where the electronic band gap 1 to 2 eV[12, 13, 65, 66] is exploited. However, more recent optical experiments[17, 18, 19] revealed that the low-energy charge carriers in these materials belong to one of the two degenerate valleys in the Brillouin zone: K and K'. By coupling to the circularly polarized light it becomes possible to excite the charge carriers from one of the valleys selectively while keeping the other one intact. This opened a new prospect for exploiting another degree of freedom of an electron which is the valley degree of freedom.

The valleys are specific to the electronic band structure of the material. Typically, the multivalley material has a pair of valence band maxima in the case of an insulator or a pair of electron/hole pockets in the case of a semimetal connected by a symmetry, such as time-reversal. The valley degree of freedom can be used to store information[67, 68] in a similar fashion to the electron spin in spintronics[69, 70, 71, 72]. Unlike spins-polarized electrons, however, electrons belonging to one of the valleys exist only in the valley-supporting material and once the charge carrier leaves the bulk of this material it loses this degree of freedom and becomes indistinguishable from the rest of charge carriers. This is not the case for the spin degree of freedom causing charge carriers to carry a magnetic moment regardless of the surrounding media. Thus, spintronics is more universal in terms of applications than valleytronics.

Having both valley *and* spin indexing for the charge carriers in material is beneficial for applications. Surprisingly, such scenario is realized in monolayer 2H-TMDs where the bands at K and K' valleys are spin-split and, thus, the spin and valley indexes are coupled[16]. The effect of the spin-orbit coupling, however, is much larger for holes: the charge carriers in a rather large energy region close to the valence band maximum prefer to align their spins perpendicular to the material plane either upwards or downwards depending on the valley. Thus, any kind of discrimination with respect to the charge carrier valley results in the spin

imbalance which can be used as a source of spin-polarized charge carriers.

Though several optical experiments[17, 18, 19] demonstrate selective population of valleys by the hole quasiparticles there is no direct evidence of spin polarization or magnetism induced in the material. Such evidence could be obtained in optical transport experiments where the charge carriers get excited by the light and eventually decay into the magnetic lead. Depending on the light polarization one expects different values of the charge carrier current due to magnetoresistive effects. It is more practically convenient, however, to perform transport experiments where the spin polarization of current is operated by all-electric means. Being the basic building blocks of a 2D device, the line defects are expected to discriminate charge carriers with respect to their valleys in graphene[73]. As we have shown in Ref. [74] a similar idea for monolayer 2H-TMDs results in spin- *and* valley-polarized currents. This chapter is dedicated to a more detailed discussion of the results presented previously.

3.1 Bulk properties of monolayer 2H-TMDs

As demonstrated in previous sections, understanding bulk properties of materials is the first step to study charge carrier transport phenomena. This section discusses key features of electronic structures of monolayer 2H-TMDs and differences between them.

The monolayer 2H-TMDs are semiconducting materials in the hexagonal lattice. The unit cell of monolayer 2H-TMDs is a rhombus and contains 3 atoms: one high-symmetry position is occupied by a metal and the other one hosts a pair chalcogens, see Fig. 3.1(a). The third high-symmetry position of the hexagonal lattice remains unoccupied. The metallic atoms are 6-coordinated to the nearest chalcogens while latter have 3 neighboring metals and one chalcogen. The plane hosting metallic atoms is symmetrically sandwiched between the two parallel atomic planes with chalcogen atoms. The largest inter-plane distance h indicated in Fig. 3.1(a) deviates slightly across the family of materials as summarized in the following table.

Table 3.1 – Equilibrium lattice parameters a and h of monolayer 2H-TMDs (PBE-DFT level of theory).

	MoS ₂	MoSe ₂	MoTe ₂	WS ₂	WSe ₂	WTe ₂
$a, \text{\AA}$	3.140	3.273	3.497	3.145	3.275	3.504
$h, \text{\AA}$	3.116	3.331	3.613	3.133	3.350	3.630

As one can see from the above table the lattice parameters and, especially, the lattice constant a are mainly influenced by the choice of the chalcogen rather than the metal.

The monolayer 2H-TMDs naturally exist in a 3D bulk form where 2D layers of these materials are weakly coupled by the van der Waals interaction. The crystalline phases are characterized by different stacking orders and periodicities, such as 2 layers per unit cell in the 2H phase and 3 layers per unit cell in the 3R phase[75]. The 2D layers of monolayer 2H-TMDs can be exfoliated similarly to other 2D materials such as graphene.

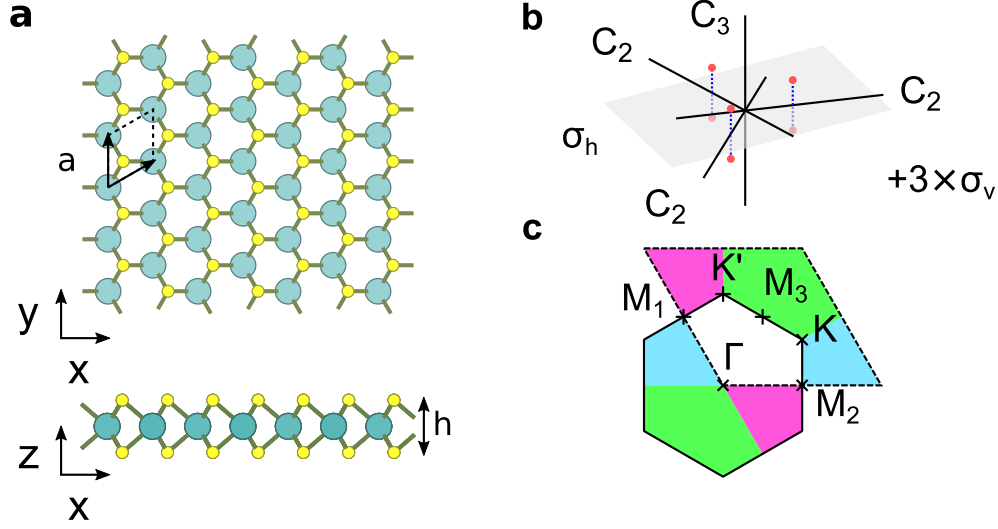


Figure 3.1 – The crystal structure and symmetries of monolayer 2H-TMDs. (a) Top and side views of monolayer 2H-TMDs. The unit cell is shown in bold. The 2 lattice parameters, a and h , are indicated. (b) The D_{3h} point group to which materials' atomic structure belongs to. There is a σ_h mirror symmetry plane (gray) and a three-fold rotational symmetry C_3 with an axis perpendicular to the plane. Other symmetries are 3 2-fold rotational symmetries C_2 and 3 mirror symmetry planes σ_v containing the C_3 axis. (c) The reciprocal unit cell (dashed rhombus) and the (first) Brillouin zone (hexagon). The same color is used for equivalent areas in the reciprocal space. The 6 high-symmetry points Γ , K , K' , $M_{1,2,3}$ are indicated.

The crystal structure of monolayer 2H-TMDs belongs to the D_{3h} point group displayed in Fig. 3.1(b). The relevant symmetries are the C_3 axis and the mirror symmetry in the material plane. There is no inversion symmetry in this material. Thus, monolayer 2H-TMDs are polar materials where the metallic atoms donate electrons to chalcogens. Correspondingly, the covalent bonds formed between neighboring metals and chalcogens have a slightly polar character.

The symmetries described are also relevant to the reciprocal space of the crystal lattice. The first Brillouin zone (BZ) displayed in Fig. 3.1(c) is a hexagon where the two non-equivalent K and K' points (valleys) are its vertices. The time-reversal symmetry in this family of materials protects the spin degeneracy of bands at time-reversal invariant points Γ and $M_{1,2,3}$ as well as all three $\Gamma - M$ lines[76]. In the rest of the BZ, the lack of inversion symmetry in the lattice yields a pronounced spin character of bands such that the K and K' valleys host charge carriers with opposite spins. The lattice mirror symmetry results in the spin polarization of states to be perpendicular to material's plane.

There is a large spin-orbit splitting in the valence band of these materials caused by relativistic effects induced by heavy atomic cores, see Fig. 3.2. The effect is most pronounced at the aforementioned K and K' valleys. There, tungsten-based compounds exhibit approximately twice larger band splitting ΔE_{SO} of valence bands compared to molybdenum-based compounds.

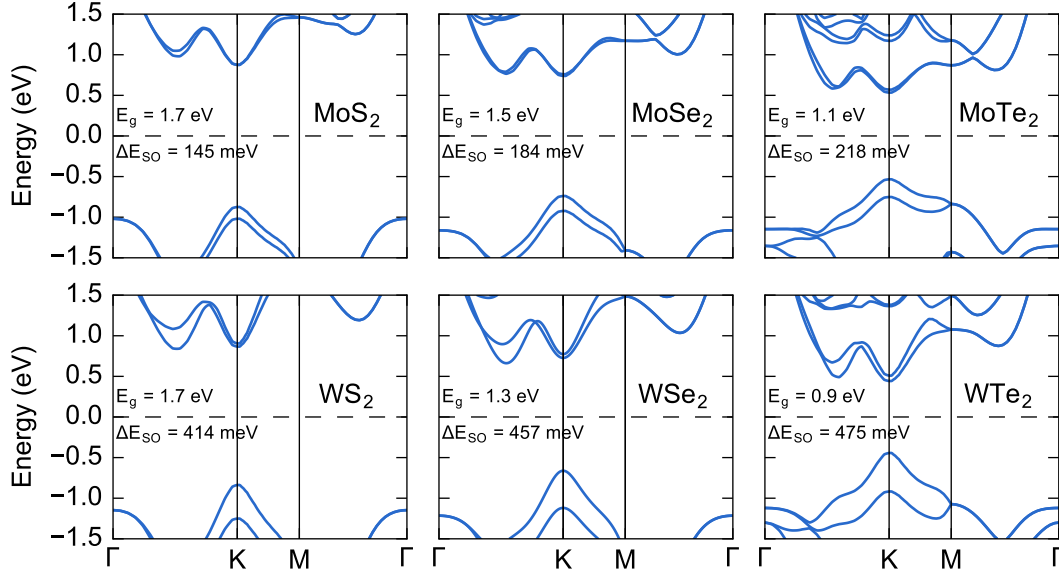


Figure 3.2 – Electronic band structures of 6 2D TMDs. The electronic band gap E_g and the largest spin-orbit splitting in the valence band Δ are indicated in each case.

The spin-orbit effects are not uniform across the band structure: while the hole charge carriers at K, K' points are split by hundreds of meV in energy, their electron counterparts exhibit a splitting less by an order of magnitude. There are also high-symmetry directions connecting Γ and M points in the reciprocal space where energy levels are spin-degenerate. Thus, all 3 M points are equivalent. As already outlined, it is not the case for K and K' points: while the band dispersion there is same, the spin textures of the bands are opposite.

Both p- and n-type doping is possible for monolayer 2H-TMDs. Chalcogen vacancies are typically identified under metal-rich conditions resulting in the positive doping. This effectively shifts the Fermi level into valence bands such that hole pockets appear at the K and K' points in the Brillouin zone, Fig. 3.3 (bottom row). Being a circle at low doping levels, the constant energy contours possess a 3-fold rotational symmetry and become triangular-warped deeper in the valence energy region. The electron pockets appearing at negative doping levels also exhibit a nearly circular shape, Fig. 3.3 (top row). Increased doping levels lead to rather hexagonal shape of Fermi surfaces which is also in agreement with the 3-fold symmetry. It is also possible to identify additional electron pockets at points with lower symmetry for $E_F = 200$ meV which are believed to be responsible for the charge density wave structural transitions in this family of materials[77].

Overall, monolayer 2H-TMDs are similar both in terms of atomic and electronic structures. There are quantitative differences in terms of lattice constants, the band gap magnitudes, spin-orbit splitting values, effective masses of charge carriers and the energy levels at Γ and K, K' valleys. The direct band gap in monolayer 2H-TMDs, however, is always found at K and K' high-symmetry points in the reciprocal space. Thus, a similar charge carrier transport

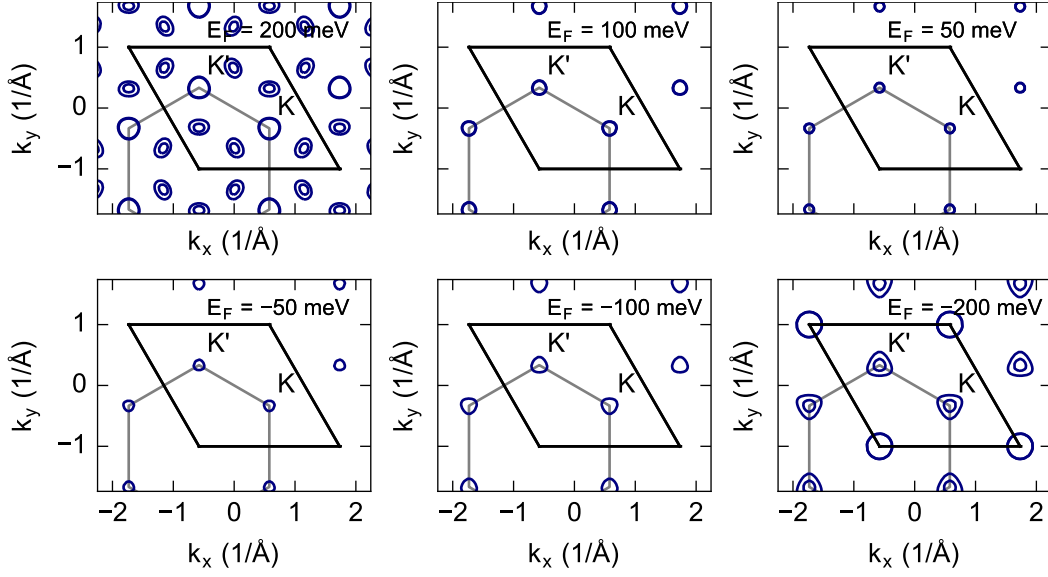


Figure 3.3 – Fermi surfaces in monolayer 2H-MoS₂ at different doping levels. The top row corresponds to the negatively doped material (the Fermi level is indicated with respect to the bottom of the conduction band) while the bottom row corresponds to the positive doping (valence band top is set as the origin for E_F). Both reciprocal unit cell (black) and the first Brillouin zone (grey) are shown.

behavior is expected in all materials.

3.2 Line defects in monolayer 2H-MoS₂ and other TMDs

Several kinds of line defects have been observed in monolayer 2H-TMDs [78, 40, 79, 80, 81]. For example, in a monolayer 2H-MoS₂ the line defects occur between domains with different orientations as shown in Fig. 1.8. Among them, the simplest ones are inversion domain boundaries with examples given in Fig. 3.4(c,d). Inversion domain boundaries occur between domains with opposite crystallographic orientations. It is not the case of a sulfur vacancy line defect presented in Ref. [78]. There, the defect was created within the same crystalline domain of a monolayer 2H-MoS₂ in a controlled manner using an electron beam.

The relaxed SVL, IDB1 and IDB2 defect structures presented in Fig. 3.4 are consistent with the corresponding microscopy images. Missing sulfur atoms in the SVL defect induce a tensile strain in the corresponding atomic layer and bend the material plane. The under-coordinated molybdenum atoms tend to form a covalent bond in this case reducing the interatomic distance from 3.2 Å to 2.9 Å. Unlike SVL, the IDB1 defect keeps the mirror symmetry in the material plane intact. There, the sulfur sublattice is effectively defect-free while molybdenum atoms occupy different high-symmetry positions at both sides of the defect and, thus, form the defect. The distance between Mo atoms at the defect is decreased down to 2.6 Å, thus, suggesting strain in the material plane. Otherwise, the coordination between molybdenum

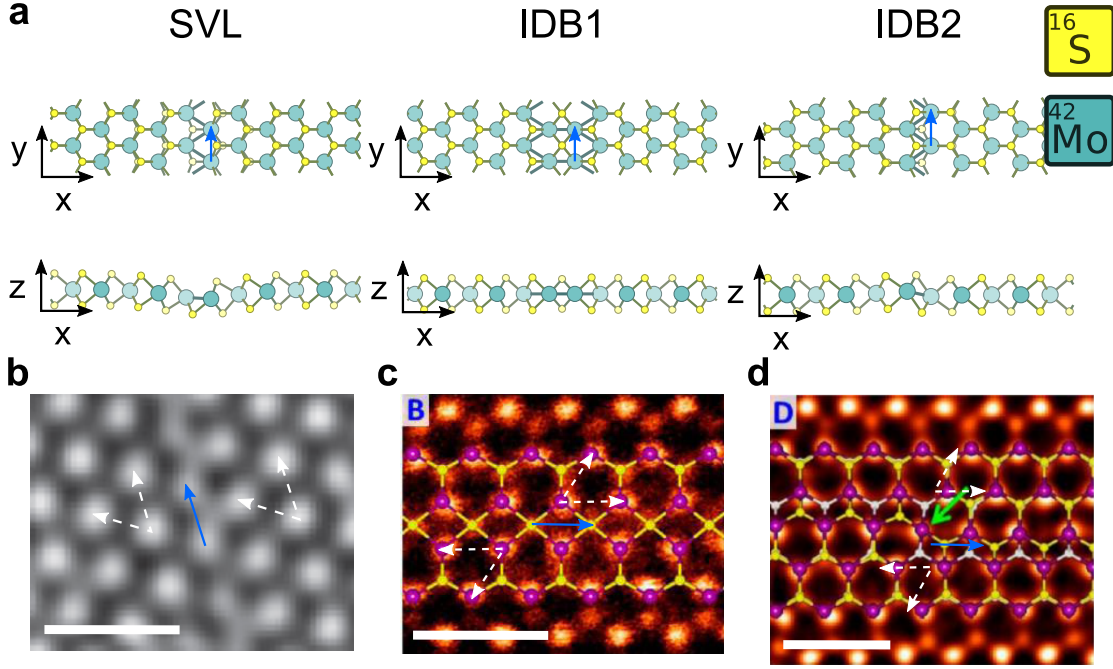


Figure 3.4 – Atomic structures of periodic line defects in monolayer 2H-MoS₂. (a) Models of the sulfur vacancy line (SVL) and inversion domain boundaries (IDB), top and side views. The models are periodic along the zigzag direction of the lattice (blue arrows). (b-d) Atomic microscopy images of the prototype defects. The periodicity vector (blue) together with bulk lattice vectors (white) are indicated. The scale bars are 1 nm. Parts of images are reproduced with permissions from Refs. [78, 40].

and sulfur atoms remains bulk-like for atoms close to the defect. However, it is not the case for the third defect, the IDB2, where the molybdenum atoms at the defect are under-coordinated compared to the bulk values. There is also a slight out-of-plane distortion of the atomic lattice in this case. Based on the coordination numbers, it is possible to deduce a Mo-rich local composition of all three defects.

All defect models considered are periodic along the defect line. The periodicity vector \vec{d} introduced in previous sections takes the smallest possible (1,0) value as shown in Fig. 3.4 (blue arrows). In real samples, however, the line defects are quasi-periodic: the regular defect pattern may be interrupted as in the case of an IDB2 defect shown in Fig. 3.4(d). This effectively causes violation of conservation laws (pseudomomentum and spin) in transport and will be discussed later.

A final remark is given on the robustness of domain boundaries against local changes in atomic structure. In particular, the relative angle between equivalent lattice vectors of monolayer 2H-MoS₂ domains plays a role of an invariant protecting the existence of the defect. Provided the angle is not a multiple of $2\pi/3$ the domains remain non-equivalent in terms of their

orientation. Thus, the corresponding inversion domain boundary is guaranteed to exist and the local changes of the atomic structure cannot terminate or eliminate the defect without destroying one of the bulk crystals completely. Such topological protection is the case for most of intrinsic line defects in monolayer 2H-MoS₂ and inversion domain boundaries in particular. In contrast, a pristine monolayer 2H-MoS₂ flake can be recovered from the SVL model by simply donating the missing sulfur atoms.

3.3 Ballistic transport across periodic line defects in a monolayer 2H-MoS₂

The ballistic transport in monolayer 2H-TMDs is particularly interesting from the point of view of interplay between conservation laws (energy, pseudomomentum, spin), the spin texture of bulk bands and the spin-valley coupling. The simulations show that all (1,0) defects presented in Fig. 3.4 are non-magnetic, thus, the whole setup is spin-neutral. This eliminates several spin relaxation channels (spin waves, relaxation on local magnetic moments) suggesting a larger spin lifetime in monolayer 2H-TMDs. On the other hand, the periodicity of defects imposes certain conditions on the charge carrier pseudomomentum and, thus the valley index. Finally, the whole picture is complemented by the spin-valley coupling discussed previously. The excess of conditions to be satisfied may prohibit the charge carrier transmission at the level of symmetries and may cause a transport gap.

3.3.1 The transport gap

To understand the role of the conservation laws in the charge carrier ballistic transport consider 2 cases schematically illustrated in Fig. 3.5(a,b). The first case corresponds to, for example, the SVL defect where the leads have a matching crystallographic orientation. There, the ballistic transport channels connect bulk wavefunctions with exactly the same spatial and spin character. In particular, the transport channels corresponding to the K and K' points of the BZ transmit charge carriers without changing spin. However, provided the drain lead is rotated with respect to the charge carrier source, the endpoint of the transmission channel is changed. This generally reduces the transmission probability: naively, the overlap between incoming and transmitted states becomes non-unity. In the case of IDBs, however, the reduction of transmission probability is exaggerated up to no charge carrier transmission at all because the single-particle bulk states corresponding the channel are orthogonal in the spin space. This is schematically illustrated in Fig. 3.5(b) where the same channel connects bulk states with different spin and valley character. An alternative point of view on this process is following: the rotation of one of the leads in real space causes rotation of the corresponding BZ such that the K and K' points are swapped. The charge carriers, however, tend to conserve their spin and, thus the valley due to the spin-valley coupling. The conflict between these two processes prohibits charge carrier transport.

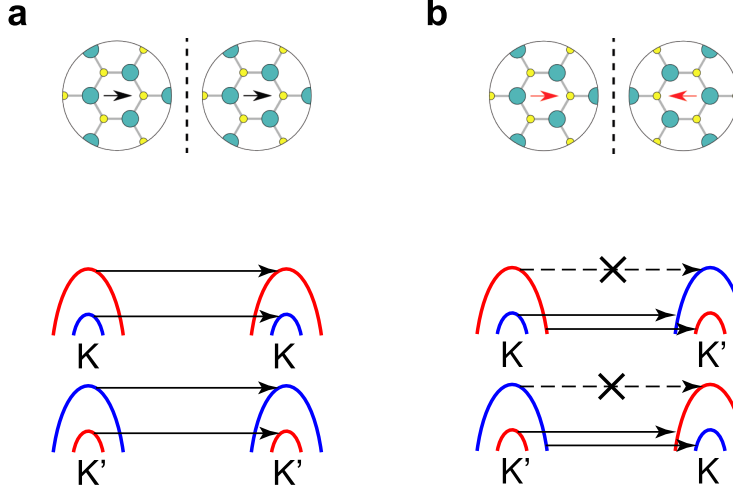


Figure 3.5 – The transport gap for charge carriers travelling across line defects. (a) A schematic illustration of a non-topological line defect (top) and the corresponding band diagram of the charge carrier transmission (bottom). The matching colors in the bottom panel indicate the value of spin polarization of the two topmost valence bands in leads. The arrows indicate allowed charge carrier transport channels. (b) The topological line defect case. The opposite orientations of bulk lattices in the top panel cause mismatch of spin in transport indicated with colors in the bottom panel. The crossed arrows indicate closed ballistic transport channels.

The above transport gap argument can be summarized in the following picture of the electronic band structure of a defect. Consider a defect with a periodicity vector \vec{d} . This vector can be expressed as a sum of bulk unit vectors \vec{a} , \vec{b} with integer pre-factors n, m for both left (L) and right (R) leads:

$$\vec{d} = n_L \vec{a}_L + m_L \vec{b}_L = n_R \vec{a}_R + m_R \vec{b}_R. \quad (3.1)$$

The periodicity vector \vec{d} in the real space defines the 1D Brillouin zone of the defect. The only coordinate of the reciprocal space of the defect is the aforementioned projection of the pseudomomentum $k_{||}$. To discover the spin-conserving and spin-flip channels one projects the leads' modes onto the 1D BZ, see Appendix A.5 for the details. Examples of such projection for both leads are demonstrated in Fig. 3.6. While the Γ point can be projected onto $k_{||} = 0$ only, there are several possibilities for other high-symmetry points K and K'. They can be projected

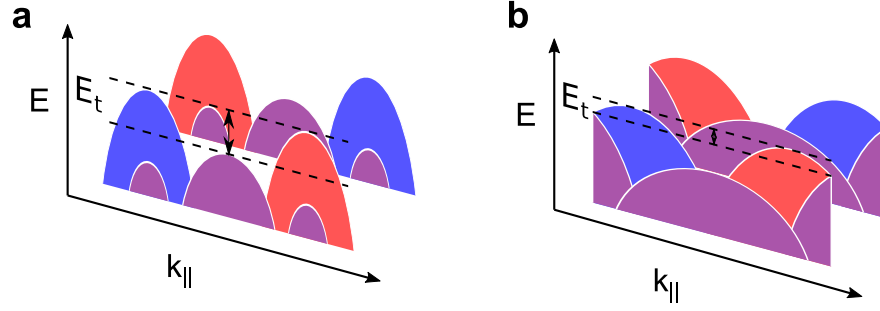


Figure 3.6 – A schematic illustration of bulk states of a monolayer 2H-MoS₂ in the leads projected onto the 1D BZ of the defect. The color indicates spin polarization of states at a given E , $k_{||}$: red and blue are spin-up and spin-down states only while magenta indicates that states with both spin polarization are available. (a) The case of a small defect periodicity vector with a large 1D BZ. (b) The case of a large defect periodicity vector with a small 1D BZ. The transport gap E_t is indicated in both cases.

either onto $\pm \frac{4\pi}{3d}$ or onto Γ , depending on n and m ($d = |\vec{d}|$):

$$\begin{aligned} (n-m) \bmod 3 = 0: & \quad k_{||}(\text{K}) = k_{||}(\Gamma) = 0; \\ (n-m) \bmod 3 = 1: & \quad k_{||}(\text{K}) = \frac{2\pi}{3d}; \\ (n-m) \bmod 3 = -1: & \quad k_{||}(\text{K}) = -\frac{2\pi}{3d}. \end{aligned} \quad (3.2)$$

The transport gap occurs if

$$(n_L - m_L) \bmod 3 \neq (n_R - m_R) \bmod 3, \quad (3.3)$$

i.e. if K valleys hosting spin-up states from different leads are projected differently. The resulting magnitude of the transport gap E_t is defined as the maximum possible energy where the charge carrier transmission is restored:

$$E_t = \min \left[\Delta E_{\text{SO}}, \Delta E_{\text{K}-\Gamma}, \frac{h^2}{72m^*a^2} \frac{a}{d} \right], \quad (3.4)$$

where the effective mass of charge carriers m^* , the lattice constant a and the Planck constant h are included. The details of the above expression can also be found in Appendix A.5.

The Eq. 3.4 claims the transport gap to be inversely proportional to the defect periodicity d .

Chapter 3. Spin and valley transport across regular line defects in semiconducting TMDs

This is a formal illustration of the fact that in the limit of a non-periodic line defect when $d \rightarrow +\infty$ the pseudomomentum is not conserved, thus, the charge carriers are always allowed to scatter to the preferred valley hosting bulk states with the spin required. The intermediate case of a large but finite d is illustrated in Fig. 3.6(b). There, the BZ gets smaller while the valleys effectively overlap more allowing an intra-valley scattering at energies close to the Fermi level.

Another remark is related to the Γ valley where bulk states are spin-degenerate. As illustrated in Fig. 3.6(a) the highest-energy states at the Γ valley set the lower limit for the transport gap, though, according to band structures presented in Fig. 3.2 it is not a relevant factor in both selenides and tellurides where $\Delta E_{\text{SO}} < \Delta E_{\text{K}-\Gamma}$.

The discussion above is based on the fact that the non-magnetic defects do conserve spin of charge carriers. This is not exactly true: there is an out-of-plane easy axis for charge carrier spins in monolayer 2H-TMDs. If the defect is bent, the axis is changed accordingly to match the local effective plane of a monolayer material. For example, both SVL and IDB2 defects in Fig. 3.4 are subjects to out-of-plane deformations. Thus, a charge carrier approaching these defects with an out-of-plane spin will form a non-zero overlap with charge carriers from the opposite valley with an opposite spin due to spin precession around a local easy axis. The non-zero overlap between spin states assists charge carrier transmission via a spin-flip channel which is otherwise closed. The *ab-initio* simulations presented further provide a qualitative measure to this effect.

3.3.2 Transport simulations and the spin polarization of charge carrier current

As outlined in the beginning of this chapter, the valley and, thus, spin polarization of charge carriers in monolayer 2H-MoS₂ can be induced by light. Another opportunity to induce the valley polarization using transport across line defects was suggested for graphene[73]. There, otherwise equivalent valleys are discriminated by allowing ballistic currents to cross the periodic line defect at oblique angles. This results in the valley polarization of the current flowing across the defect. In monolayer 2H-TMDs, the valley polarization of hole charge carriers is equivalent to the spin polarization due to the spin-valley coupling. Thus, a similar setup in monolayer 2H-TMDs is expected to give rise to spin currents (the physical background of the original proposal and its relevance to monolayer 2H-TMDs are given in Appendix A.2). The argument is supported by the results of *ab-initio* transport simulations presented in this section.

In particular, three defects from Fig. 3.4 were considered. Each defect was relaxed following the NEGF¹ transport simulations described in the previous chapter. Other details of simulations are given in Appendix A.3.

¹While the NEGF abbreviation stands for the non-equilibrium Green's function the actual calculations were carried out under zero voltage bias which may be viewed as an equilibrium setup.

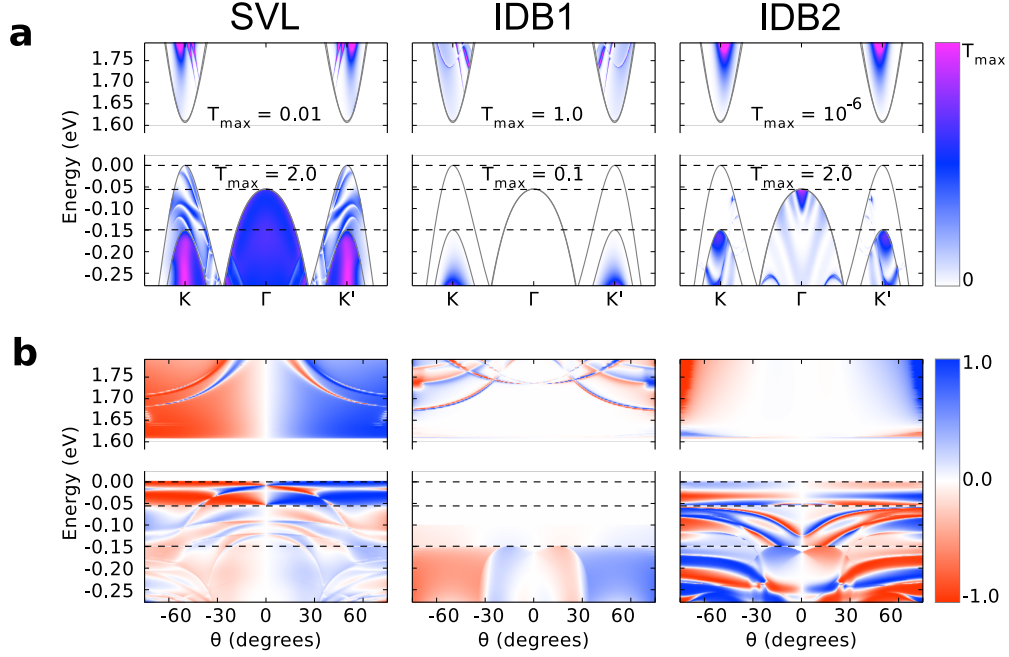


Figure 3.7 – Transport properties across line defects in monolayer 2H-MoS₂ from Fig. 3.4. (a) The k_{\parallel} and energy-resolved transmission function of corresponding line defects. The color represents values of transmission ranging from 0 to T_{\max} with individual values of T_{\max} for holes and electrons indicated on the plots. The contour lines indicate band edges while the horizontal dashed lines indicate band energy extrema. (b) The value of the spin polarization of transmitted charge carriers as a function of energy and the charge carrier incidence angle θ defined in Eq. 3.5. The white color indicates equal contributions of spin-up and spin-down charge carriers to the total transmission. The valence band maximum is placed at zero.

Fig. 3.7 summarizes the results of ballistic transport simulations. There, for each line defect from Fig. 3.4 the transmission function calculated using Eq. 2.75 is presented in panel (a) and the mean spin polarization of transmitted charge carriers is presented in panel (b). The latter is defined as

$$P_{\sigma} = \frac{\sum_i T_i \sigma_i}{\sum_i T_i}, \quad (3.5)$$

where σ_i is the out-of-plane spin polarization of the bulk outward state i and T_i is the cumulative transmission probability into the state i . In bulk 2H TMDs $\sigma_i = \pm 1$ though this is not required for the actual formalism, see Appendix A.4 for details.

In terms of the leads' bulk properties, the SVL defect corresponds to the case (a) in Fig. 3.5. Thus, one expects a non-zero transverse transmission probability for this defect provided the existence of bulk states at a given (k_{\parallel}, E) . The argument is in agreement with the calculated

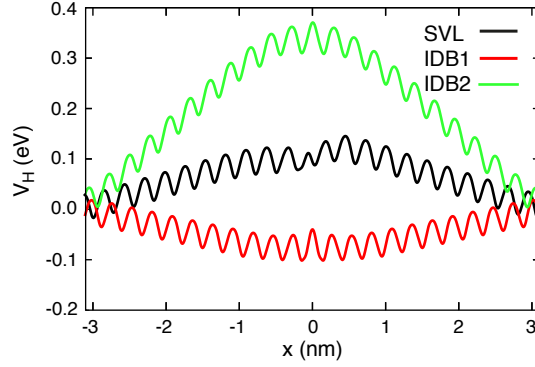


Figure 3.8 – The single-particle Hartree potential of monolayer 2H-MoS₂ defects presented in Fig. 3.4. The horizontal axis corresponds to the distance to the line defect in the transport direction. The potential is averaged in parallel planes.

transmission function presented in Fig. 3.7(a) and bounded by the bulk monolayer 2H-MoS₂ bands. The defect is transparent for holes $E < 0$ with the total transmission $T_{\max} = 2$ approaching the maximum possible value equal to the bulk band degeneracy at these energies. The charge carrier transmission function at the Γ valley $k_{\parallel} \approx 0$ is very uniform and does not depend significantly on parameters (E, k_{\parallel}) in contrast to transmission probabilities at K and K' valleys.

Unlike the hole charge carriers, the transmission function for electrons is significantly lower. The transmission function close to the bottom of valence bands barely reaches 10^{-2} . It can be explained by considering classical particles in a bending electrostatic potential: provided SVL is a negatively charged defect, holes are effectively attracted by the defect while electrons get reflected from it. An effective single-particle potential plotted in Fig. 3.8 for all defects confirms the argument. There, depending on the effective charge, the potential bends upwards or downwards resulting in a better transparency either for holes or for electrons.

The values of the spin polarization of transmission P_{σ} presented in Fig. 3.7(b) indicate a strong discrimination of charge carriers with respect to their spin and incidence angle. The fact that spin-up charge carriers prefer positive incidence angles while spin-down charge carriers transmit better in the mirror-symmetric direction,

$$T_{\sigma}(\theta) = T_{-\sigma}(-\theta), \quad (3.6)$$

is consistent with a similar conclusion for graphene [73]. However, the resonant features in the transmission function cause a non-uniform behavior of the spin polarization value at a given angle: depending on the charge carrier energy, the spin polarization may vanish (white regions close to the Fermi level) or even change its sign. The value of $|P_{\sigma}|$ is almost saturated at the value of 0.99 indicating the fact that the SVL defect can be used as a spin polarizing device. In particular, the spin filtering is possible if a small bias not exceeding 50 mV is applied to the device based on a positively doped monolayer 2H-MoS₂. At larger voltages, the channels at the Γ valley may become open producing a large spin-degenerate charge carrier current and

3.4. Ballistic transport across inversion domain boundary in monolayer 2H-MoSe₂

resulting in a much lower value of $|P_\sigma|$. It is also possible to achieve significant values of P_σ for electron charge carriers though the transparency of the defect in this case is much lower.

Unlike the SVL defect, both IDBs satisfy Eq. 3.3 and, thus, correspond to the transport gap case schematically illustrated in Fig. 3.5. Thus, there is no transport of low-energy hole charge carriers in this case. The argument is in agreement with the corresponding simulation results presented in Fig. 3.7(a). Deeper in the valence energy region spin-conserving channels become available and the charge carrier transmission is restored there. The relevant channels releasing the ballistic transport regime are first found at the Γ valley for the IDB2 defect while in the case of IDB1 the transmission probabilities there are relatively low.

The aforementioned transport gap is reproduced perfectly for the IDB1 defect. Instead, the IDB2 case shows a small residual transmission in the energy gap region presented in Fig. 3.7(a). There, the spin-flip transmission channels are open. As discussed, both defects are non-magnetic, however, the IDB2 defect violates the out-of-plane direction as an easy spin axis due to bending of the defect structure. The bulk spin-up and spin-down states become coupled in this case.

One more feature related to the charge carrier transport is the fact that the IDB1 and the IDB2 defects accumulate opposite effective charges. The over-coordinated sulfur atoms in the first case gain an additional positive charge while under-coordinated molybdenum atoms in the second defect are charged negatively compared to their bulk counterparts. This is in agreement with the single-particle potential profiles presented in Fig. 3.8.

3.4 Ballistic transport across inversion domain boundary in monolayer 2H-MoSe₂

As a part of a joint project together with experimental groups of Ute Kaiser at the University of Ulm and Andras Kis at EPFL as well as the theoretical group of Arkady V. Krasheninnikov at the Aalto University the transport properties of an inversion domain boundary in monolayer 2H-MoSe₂ were studied. The defective material exhibited crystalline monolayer 2H-MoSe₂ flakes with various orientations separated by ordered line defects as shown in the microscopy images in Fig. 3.9. Among the line defects observed are the simplest (1,0) inversion domain boundary shown in Fig. 3.9(b) and small-angle domain boundaries presented in the original work[80]. The inversion domain boundary is similar to the IDB1 defect considered in the previous section for a monolayer 2H-MoS₂. Thus, similar transport properties are expected. To verify this, the NEGF calculations have been carried out of the relaxed defect model.

The resulting transmission function, Fig. 3.10(a), and the potential profile, Fig. 3.10(b) strongly resemble those of the monolayer 2H-MoS₂ IDB1 model presented in Figs. 3.7(a), 3.8. The atomic structure of the defect presented in Fig. 3.10(b) does not show any new qualitative features either. Both defects are charged positively resulting in a better transmission probability for electrons. Similarly to the defect in monolayer 2H-MoS₂, transmission probabilities at the

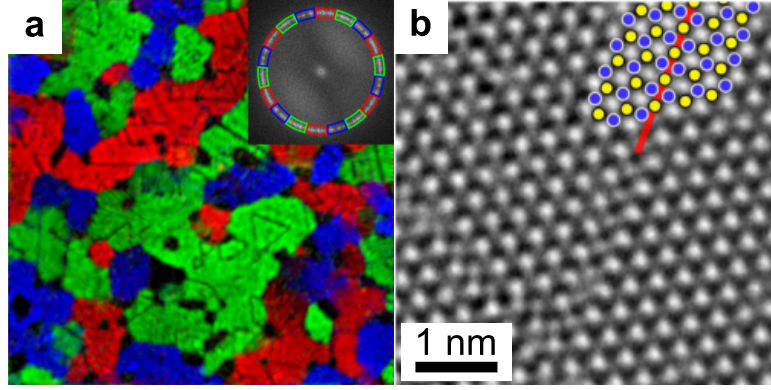


Figure 3.9 – Atomic microscopy images of defective monolayer 2H-MoSe₂ showing polycrystalline structure of the sample. (a) A large-scale microscopy image of monolayer 2H-MoSe₂. The different colors correspond to different crystallographic orientations of monolayer 2H-MoSe₂ grains. (b) Inversion domain boundary in monolayer 2H-MoSe₂ imaged. A schematic atomic structure is overlaid.

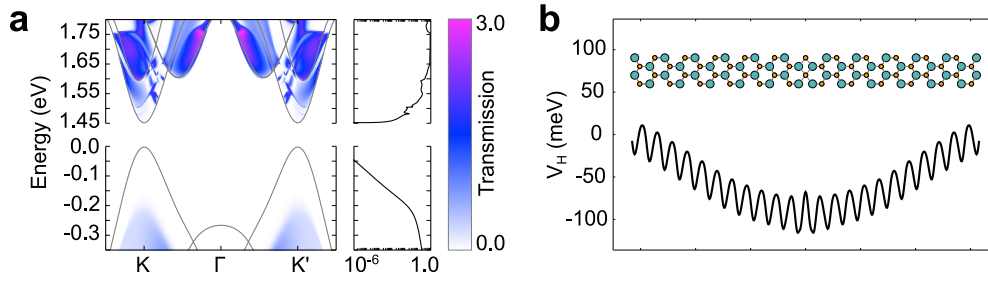


Figure 3.10 – Electronic and transport properties of an inversion domain boundary in MoSe₂. (a) $k_{||}$ -resolved transmission function values (left) and the integrated transmission (right) as a function of a charge carrier energy E . (b) The single-particle Hartree potential profile across the inversion domain boundary averaged over planes. The top view of the relaxed atomic structure is also shown.

Γ valley for the monolayer 2H-MoSe₂ model are rather small. The expected transport gap in these calculations that did not focus on spin- and valley-polarized transport is not captured by the model: the spin degree of freedom for the Kohn-Sham wavefunction was ignored in favor of simplicity of the description. According to Eq. 3.4 as well as the bulk band structure data presented in Fig. 3.2 the magnitude of the transport gap expected in monolayer MoSe₂ is rather defined by the spin-orbit splitting value $\Delta E_{SO} = 184$ meV being smaller than the value of $\Delta E_{K-\Gamma}$ for this material.

To summarize, the inversion domain boundary defects in monolayer monolayer 2H-MoS₂ and MoSe₂ are very similar from the point of view of electronic and transport properties. The simulations do not show any qualitative differences between the defect models despite being done at a slightly different methodological level. Nevertheless, the transport gap in a monolayer 2H-MoSe₂ is expected to be substantially larger compared to the one in monolayer

2H-MoS₂ due to lower energies of holes at the Γ valley. This also suggests better spin filtering capabilities of a monolayer 2H-MoSe₂ where the spin-degenerate ballistic charge carrier current originating from the Γ valley is irrelevant.

3.5 Conclusions

As demonstrated, the ballistic charge carrier transport across periodic line defects in a monolayer 2H-MoS₂ is governed by several conservation laws. The conservation of spin together with the spin-valley coupling cause charge carrier transport properties to be strongly discriminated with respect to the spin value. For non-topological defects, high spin polarization of charge carrier currents are predicted. For inversion domain boundaries, the conservation of spin causes suppression of spin-flip channels resulting in a transport gap extended into the valence energy region. The defect orientation and periodicity plays a defining role in this process. The electric charge accumulated on line defects causes discrimination of transmitted charge carriers with respect to their energy. The conclusions are also applicable to other monolayer 2H-TMDs with qualitatively same structural and electronic properties. The transmission probabilities obtained for an inversion domain boundary in monolayer 2H-MoSe₂ show a qualitatively same picture. Overall, the phenomena discussed may find applications in 2D electronics and spintronics where line defects could constitute a lateral device.

4 Electronic properties of the distorted 1T structural phase in monolayer TMDs

The 2H structural phase is the thermodynamically stable phase of monolayer MoS₂, MoSe₂, MoTe₂, WS₂, WSe₂. However, monolayer WTe₂ as well as other monolayer TMDs such as ReS₂ realize a different atomic structure. There, one of the chalcogen atoms shifts inside the unit cell parallel to the material plane resulting in the 1T lattice structure presented in Fig. 4.1. However, monolayer 1T-TMDs are usually not stable. They are subjects to a spontaneous breaking of the translation symmetry accompanied by the formation of metallic zigzag chains and a slight change of unit cell vectors. The resulting 1T' lattice structure is illustrated in Fig. 4.1.

The spontaneous breaking of the translation symmetry leading to the 1T' phase may occur along one of the three equivalent crystallographic directions of the hexagonal lattice. The resulting 1T' unit cell contains six atoms compared to three atoms in the unit cell of the 1T phase. The ratio between 1T' lattice constants a and b shown in Fig. 4.1 resembles the original hexagonal symmetry: $a/b \approx \sqrt{3}$. Unlike the original 2H lattice, both 1T and 1T' lattice structures contain inversion centers indicated in Fig. 4.1. Combined with the time reversal symmetry preserved by the material, the inversion symmetry results in the two-fold spin degeneracy of all bulk states in monolayer 1T'-TMDs.

Among the monolayer TMDs being discussed, the 1T' phase is a ground state phase for WTe₂ only, however, other TMDs can be stabilized in this phase by n -doping the material via lithium or sodium intercalation[82, 83, 84, 85]. Depending on the details of an experimental realization, the undistorted 1T phase was also reported in observations[79, 86].

The monolayer 1T' phase is widely discussed in terms of its electronic properties. Having the same chemical composition, monolayer 1T' TMDs make a good lateral contact with the semiconducting monolayer 2H phase[87]: the low Schottky barrier at the interface results in a high transparency of the junction to transverse charge carriers. A non-trivial band ordering of the monolayer 1T' phase[88] attracts interest in the topological insulator community. The quantum spin Hall (QSH) phase predicted for the family of materials may find applications provided the bulk band gap of the monolayer 1T' phase is large enough. By the time of

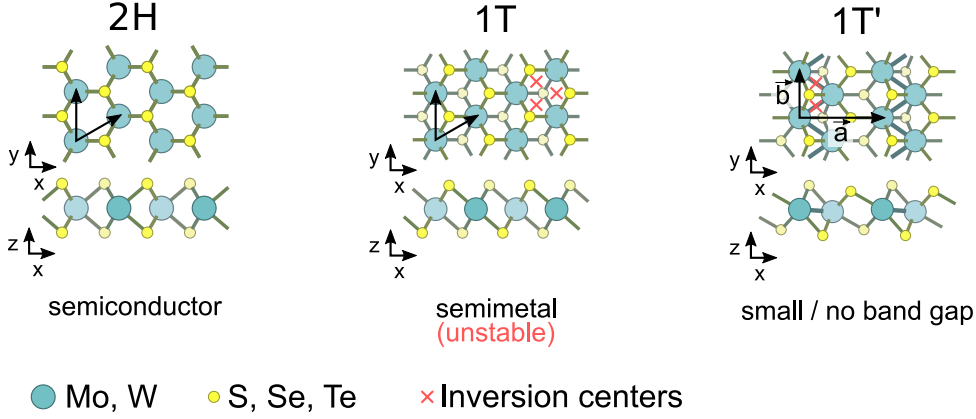


Figure 4.1 – Structural phases of 2D TMDs: 2H, 1T and 1T', top and side views. The lattice unit vectors are indicated.

writing the thesis no experimental confirmations of the topological insulator phase have been published.

4.1 Bulk properties of the monolayer 1T' phase

While the atomic structures of monolayer 2H- and 1T'-TMDs are closely related, there are substantial differences in their electronic properties. Unlike the semiconducting monolayer 2H phase, the 1T' phase is a semimetal or a semiconductor with a ten meV-order band gap with corresponding electronic band structures presented in Fig. 4.2. DFT calculations predict the largest band gap at equilibrium lattice constants in the monolayer 1T'-MoS₂: 48 meV. Apart from MoS₂, the selenides MoSe₂, WSe₂ exhibit a slightly smaller electronic band gap while WS₂, MoTe₂ and WTe₂ are semimetals.

The band gap in monolayer 1T'-TMDs is opened by the spin-orbit interaction. The spin-orbit interaction in tungsten is larger, however, in terms of the band gap magnitude there is an opposite trend: tungsten-based materials demonstrate a smaller band gap compared to molybdenum compounds. This indicates the fact that the formation of the band gap is a complex process with several factors such as the band shape affecting the band gap magnitude. According to the DFT simulation results, the maxima of valence bands (VBM) and minima of conduction bands (CBM) are different across the family of materials and can be found at various locations in the BZ as summarized in Table 4.1.

Most of the band extrema occur at the Γ point or along the high-symmetry $\Gamma - Y$ direction ($k_x = 0$) in the BZ. The only exception is the CBM in WS₂ which is away from high-symmetry directions. This was overlooked in previous studies and may be the reason why WS₂ was predicted to have a positive band gap[88] while, by fact, DFT predicts a semimetallic band structure.

4.1. Bulk properties of the monolayer 1T' phase

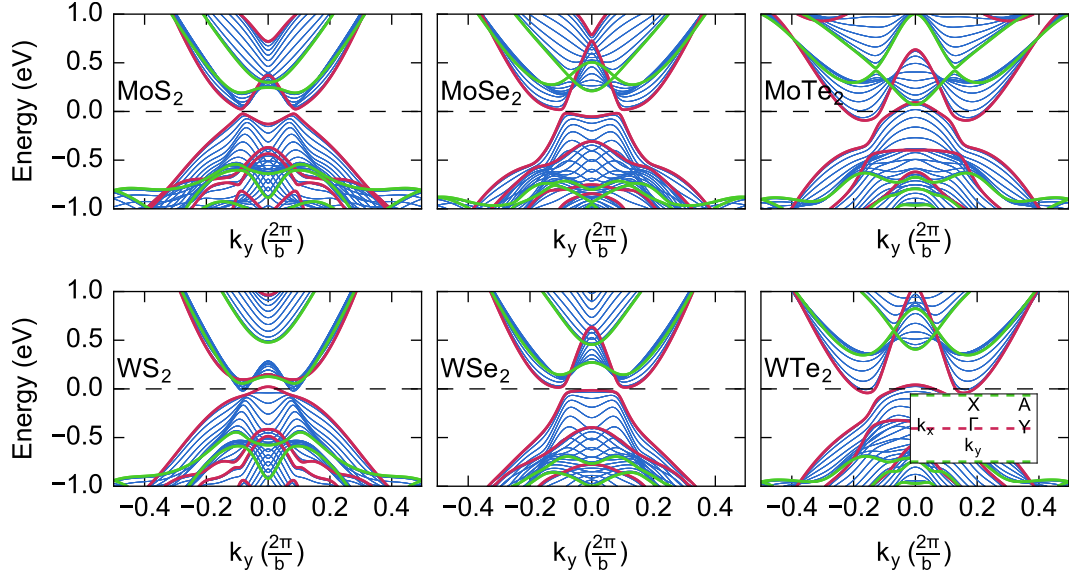


Figure 4.2 – Electronic band structures of monolayer 1T'-TMDs projected onto the largest reciprocal vector k_y . Colors are used to indicate high-symmetry paths Y – Γ – Y (red) and A – X – A (green) shown on the inset illustrating the rectangular BZ.

Table 4.1 – Properties of a band gap in monolayer 1T'-TMDs: locations of band extrema (VBM,CBM), magnitudes of the band gap E_g and magnitudes of the band gap at the Γ point Δ_Γ .

	MoS ₂	MoSe ₂	MoTe ₂	WS ₂	WSe ₂	WTe ₂
CBM	$\Gamma - Y$	$\Gamma - Y$	$\Gamma - Y$	elsewhere	$\Gamma - Y$	$\Gamma - Y$
VBM	$\Gamma - Y$	$\Gamma - Y$	Γ	Γ	Γ (flat band)	Γ
insulator	✓	✓	✗	✗	✓	✗
E_g (meV)	48	35	-184	-44	29	-84
Δ_Γ (meV)	500	780	543	125	649	1017

In semimetals, the band extrema correspond to the location of hole and electron pockets in the 2D BZ shown in Fig. 4.3. There, WS₂ indeed shows 4 relatively small symmetric electron pockets and a single hole pocket at the Γ point. Two larger electron pockets are predicted for MoTe₂ and WTe₂ showing similar behavior in terms of electronic band structures.

Semiconducting monolayer 1T'-TMDs were predicted to be topological insulators[88] in the non-trivial QSH phase. The corresponding topological invariant classifies band insulators under the time-reversal symmetry and takes two possible values $\nu = \pm 1$ depending on whether the band order is vacuum-like, $\nu = 1$, or not, $\nu = -1$. The bulk-boundary correspondence discussed previously induces at least two gapless modes at the edge of a topological insulator or wherever the topological phase changes. The edge modes of the QSH phase are time-reversal-symmetric and usually have opposite spins. This causes various phenomena specific to the boundary of the QSH phase such as the spin-momentum locking or Majorana fermion

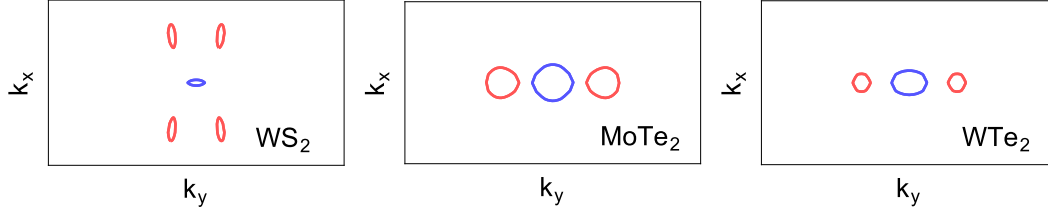


Figure 4.3 – Electron (red) and hole (blue) pockets in semimetallic monolayer 1T'-TMDs. The plot box corresponds to the Brillouin zone dimensions.

quasiparticles. For actual applications, it is better to have edge states decoupled from the bulk ones in the energy domain. This fact stimulates the search of robust QSH insulators with a large band gap.

In monolayer 1T'-TMDs, the QSH phase is caused by multiple inversions of chalcogen p and metallic d states in the energy domain[89]. The \mathbb{Z}_2 topological invariant for inversion-symmetric materials is a product of parities of Bloch states calculated at time reversal-invariant momentum (TRIM) points in the BZ: points Γ , X, Y and A. For monolayer 1T'-TMDs the parity product calculated at the Γ point has a different sign compared to the rest of parities. This intuitively suggests that the relevant band inversions occur at the Γ point. Thus, the value of the band gap at the Γ point Δ_Γ can be used as a measure of the robustness of the QSH phase. The calculated values of the Δ_Γ presented in Table 4.1 indicate that the band inversion is robust in all materials except WS_2 where $\Delta_\Gamma = 125$ meV.

4.1.1 Electronic structure properties of monolayer 1T'-WSe₂

Different levels of theory do not agree on the band gap magnitude in monolayer 1T'-TMDs as, for example, reported for monolayer 1T'-MoTe₂. The standard DFT simulations of the bulk material presented in Ref. [88] as well as in Fig. 4.1 predict the material to be a semimetal. In contrast, simulations with a hybrid exchange-correlation functional yield a band gap as large as 70 meV[90].

We collaborated with the group of Michael Crommie at University of California, Berkeley to investigate the properties of the 1T' monolayer phase in WSe₂. Specifically, our colleagues provided an experimental spectroscopic evidence of the band gap in monolayer 1T'-WSe₂. First of all, the zigzag distortion of monolayer 1T'-WSe₂ was confirmed by the STM experiment, Fig. 4.4(a). There, the pattern formed by parallel lines of the topmost selenium atoms provides a clear signature of the zigzag distortion specific to the monolayer 1T' phase. Second, the electronic structure of the monolayer material was probed by the angle-resolved photoemission spectroscopy (ARPES), Fig. 4.4(b), as well as by scanning tunneling spectroscopy (STS), Fig. 4.4(c). ARPES, generally, does not capture conduction electronic states, thus, the presence

of the band gap cannot be deduced from Fig. 4.4(b) directly. Instead, the STS data clearly shows a deep depression close to the Fermi level in Fig. 4.4(c).

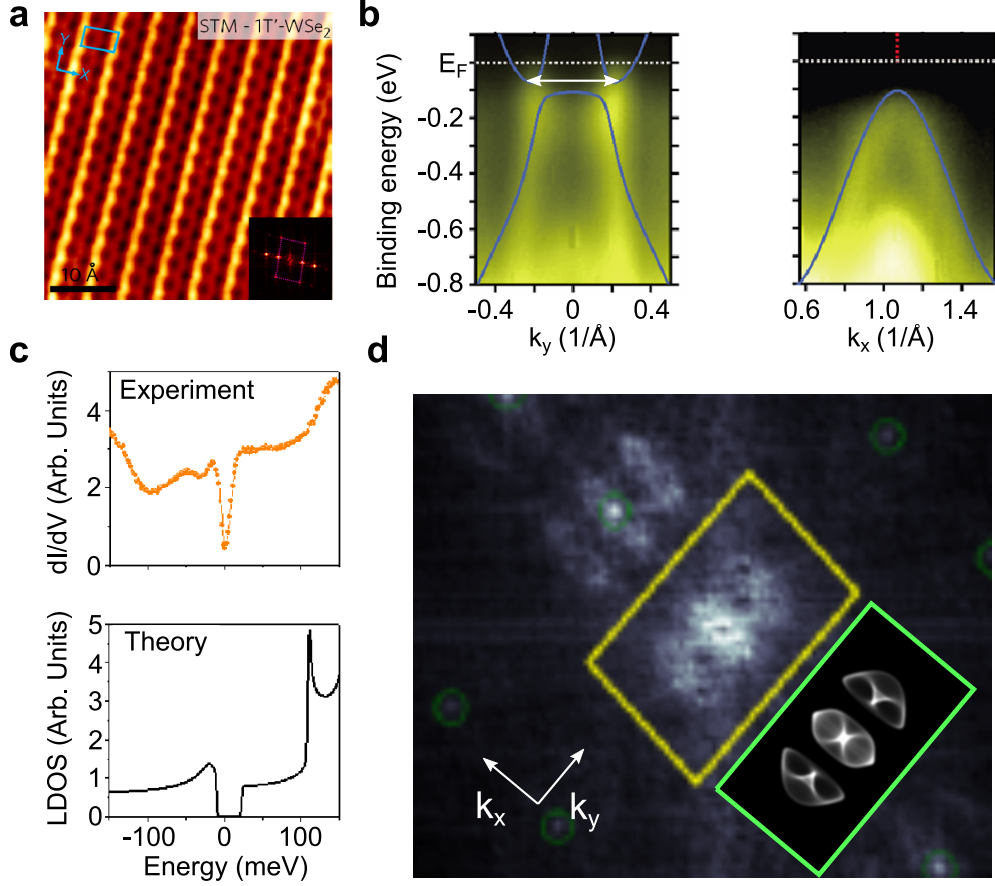


Figure 4.4 – Experimental observation of the monolayer 1T' phase in WSe₂. (a) STM image of the monolayer 1T'-WSe₂. The high-contrast regions correspond to the topmost chains of selenium atoms. (b) Angle-resolved photoemission spectroscopy (ARPES) data of the monolayer 1T'-WSe₂ electronic structure in the valence energy region. The corresponding calculated bulk bands are overlaid. The white arrow indicated two minima of conduction bands (two electron pockets in experiment) connected with a nesting vector. (c) The scanning tunneling spectroscopy (STS) data of the monolayer material (experiment) compared to the calculated density of states (theory). (d) The quasiparticle interference pattern measured for the monolayer 1T'-WSe₂ at energies 100 meV above the top of the valence bands. The Brillouin zone is marked by a yellow frame. The corresponding simulated interference signal is shown in the green frame.

To support the experimental observations, I performed calculations of electronic band structure properties of the monolayer 1T'-WSe₂ using DFT. Specifically, the electronic band structure, the density of electronic states and the autocorrelation function of the band structure in k -space were computed to compare to the experimental data.

Chapter 4. Electronic properties of the distorted 1T structural phase in monolayer TMDs

As introduced in the previous section, the monolayer 1T'-WSe₂ is a semiconductor with a 30 meV band gap also present in the DOS plot in Fig. 4.4(c). The electronic band structure showing the band gap location agrees well with the ARPES data, Fig. 4.4(b). The quasiparticle interference (QPI) pattern gives an information on possible nesting vectors in the reciprocal space of monolayer 1T'-WSe₂. It provides an important information about the dispersion of the conduction band. Practically, the QPI signal is as simple as a Fourier transform of the STS data at a given energy. Thus, the corresponding theoretical analogue can be obtained directly from the calculated band structure as, for example, described in Ref. [91]. The QPI pattern for monolayer 1T'-WSe₂ is presented in Fig. 4.4(d). It strongly resembles the corresponding simulated image (green frame) with 3 similar regions of a large signal displaced along the k_y reciprocal vector. The displacement roughly corresponds to the length of the reciprocal vector connecting electron pockets shown in Fig. 4.4(b).

The combination of experimental and theoretical evidences allows one to conclude that monolayer 1T'-WSe₂ is indeed a semiconducting material in the QSH phase. The presence of the band inversion at the Γ point is confirmed by the ARPES data being in agreement with the theoretical predictions. During the theoretical *ab-initio* investigation of its properties, however, it was found that the band gap obtained in the relaxed material is highly sensitive to the level of methodology similar to the aforementioned issue of monolayer 1T'-MoTe₂. The closing of the band gap, however, may destroy the topological phase in the family of materials. Thus, it is important to study possible mechanisms of the band gap closing and to investigate inconsistencies between different methodologies.

Specifically, the variations of materials' lattice parameters were found to have a major impact on the presence and the magnitude of the band gap. The following section discusses the electronic properties of monolayer 1T'-TMDs under strain from the theoretical perspective. The study is also presented in Ref. [92].

4.1.2 Properties of monolayer 1T'-TMDs under strain

The monolayer 1T'-WSe₂ discussed previously is a semiconductor under the DFT-PBE (Perdew-Burke-Ernzerhof[93]) approach. The LDA exchange-correlation functional[94], however, results in a semimetallic band structure for this material. The major difference between simulated electronic band structures may be due to the smaller unit cell predicted under the local density approximation. This hypothesis was verified by performing simulations of electronic properties of the four monolayer 1T'-TMDs: MoS₂, MoSe₂, WS₂, WSe₂ across the range of lattice constants.

A series of DFT electronic structure simulations of monolayer 1T'-TMDs has been performed with varying bulk lattice constants. The maximum deviation of lattice constants was set to 5% of the equilibrium values predicted at the PBE level of theory. The whole range of lattice constants was sampled on a 19x19 mesh. At each point of the lattice parameter space, atomic structures of bulk materials were relaxed and electronic band structures were calculated on a

60x90 k-point grid to capture the band gap location and magnitude accurately. Additionally, equilibrium structural and electronic properties were calculated for both LDA and PBEsol[95] exchange-correlation functionals. The latter is commonly used for a more accurate description of structural and electronic properties of 3D materials' surfaces and 2D materials.

The calculated magnitude of the band gap is presented in Fig. 4.5(a-d). The former is found to be sensitive to lattice constants in all four materials. The semiconducting phase spans an island-like region in the lattice parameter space. Thus, a relatively small deformation may close the band gap in monolayer 1T'-TMDs. The required deviations from equilibrium PBE lattice constants may be as small as 0.5% in the case of monolayer 1T'-WSe₂ or as large as 4% in the case of monolayer 1T'-MoS₂.

The difference in predicted lattice constants between methodologies, however, is larger, as indicated in Fig. 4.5(a-d). This results in the aforementioned inconsistency between predictions. Specifically, the exchange-correlation functionals considered agree in terms of the band gap magnitude only for monolayer 1T'-WS₂ where semimetallicity is predicted. Otherwise LDA always predicts a material to be a semimetal while PBE claims semiconductivity. According to Fig. 4.5, the PBEsol exchange-correlation functional results in intermediate lattice constants corresponding to either a finite band gap or no band gap depending on the material. The problem of inconsistency between predictions of the band gap magnitude is resolved by calculating the electronic band structure in a fixed unit cell using all three exchange-correlation functionals. Such calculation yields surprisingly good agreement in terms of the band gap magnitude. This confirms our initial hypothesis that the difference in values of the band gap magnitude is mostly due to the difference between equilibrium lattice structures predicted by exchange-correlation functionals. Thus, for a proper comparison with experimental data experimental lattice structures should be used in DFT simulations.

For the possible applications of the QSH phase, one is interested in increasing the magnitude of the bulk band gap. According to Fig. 4.5, the bulk band gap can be increased by applying strain. A moderate strain along the largest lattice vector a may tune the band gap magnitude in monolayer 1T'-MoS₂ to slightly larger magnitudes up to 57 meV. Though the predicted band gap magnitude in non-strained monolayer 1T'-TMDs is maximal in MoS₂, other materials of the family exhibit larger band gap magnitudes with the strain applied. According to Fig. 4.5(d) a band gap as large as 120 meV is found in strained monolayer 1T'-WSe₂. The maximal band gap encountered in monolayer 1T'-MoSe₂ is 30 meV smaller and requires larger deformations, though, this value is not saturated. To open the band gap in monolayer 1T'-WS₂ a compressive strain is required which may limit applications of the gapped phase in this material. Otherwise the maximal band gap magnitude in monolayer 1T'-WS₂, 63 meV, is comparable to the one in monolayer 1T'-MoS₂.

The mechanism of a semiconductor-semimetal transition in the materials depends on the direction of strain. Fig. 4.5(e) illustrates electronic band structures of monolayer 1T'-MoS₂ as an example. There, the band gap closing occurs at various points of the BZ. The monolayer

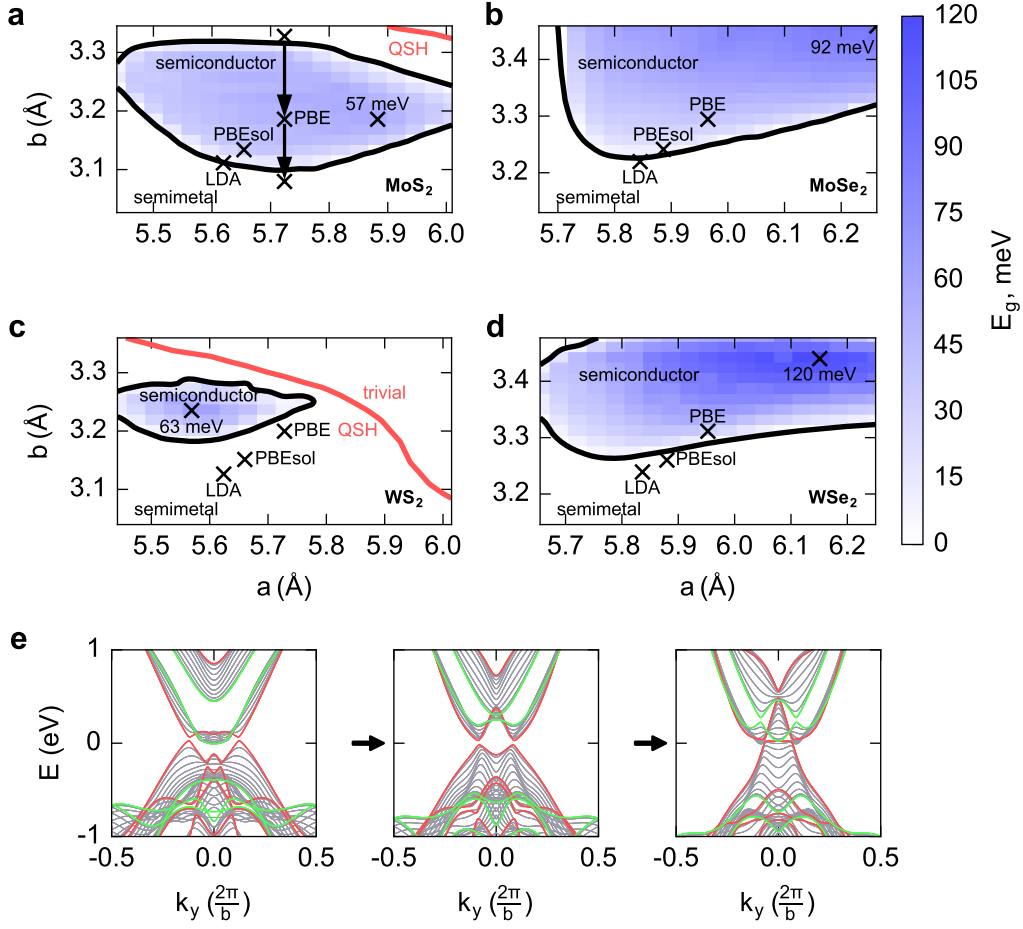


Figure 4.5 – Evolution of the electronic properties of monolayer 1T'-TMDs upon the change of lattice parameters a and b . (a-d) The magnitudes of electronic band gaps in monolayer 1T'-MoS₂, MoSe₂, WS₂ and WSe₂. The boundaries of the semiconducting and the quantum spin Hall phase in the parameter space are shown by black and red lines, respectively. Equilibrium lattice constants obtained using LDA, PBE and PBEsol exchange-correlation functionals are indicated together with the maximal band gap. (e) Electronic band structures of monolayer 1T'-MoS₂ undergoing the semimetallic-semiconducting-semimetallic transition. The corresponding path in the lattice parameter space is shown by arrows in subplot (a). The red and green bands stand for high-symmetry paths in the BZ, $Y-\Gamma-Y$ and $A-X-A$, respectively.

1T'-MoS₂ at around 4% tensile strain has its conduction band crossing the Fermi level at the X point of the Brillouin zone while the band gap closing at 3% compressive strain is different: instead of forming an electron pocket at the X point four symmetric electron pockets emerge similar to the ones in monolayer 1T'-WS₂ shown in Fig. 4.3. This leads to an observation of the fact that not only the magnitude of the band gap but also its location is sensitive to materials' lattice constants. The simulations show that the maximum of valence bands is always located along the $Y-\Gamma-Y$ path. In contrast, the minimum of conduction bands is found at various locations in the BZ. The most symmetric location of the CBM is the X point of the BZ while

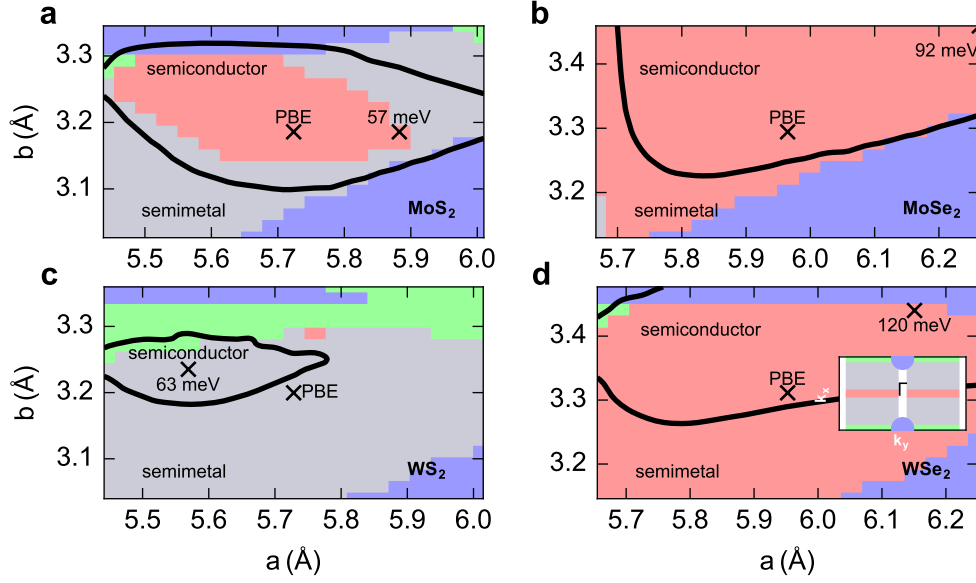


Figure 4.6 – The location of the conduction band minimum (CBM) in the Brillouin zone of monolayer 1T'-TMDs as a function of lattice parameters a and b . The color represents high-symmetry directions where the CBM is located: the red color corresponds to the $\Gamma - Y$ direction ($k_x = 0, k_y \neq \{0, \pi/b\}$), the green color corresponds to the $A - X$ direction ($k_x = \pi/a, k_y \neq \{0, \pi/b\}$) and the blue color is the high-symmetry X point ($k_x = \pi/a, k_y = 0$). The grey color corresponds to the rest of the BZ as shown in the inset. Equilibrium lattice constants, semiconducting regions and the maximum band gap values are indicated.

other locations include the $Y - \Gamma - Y$ path (except both Γ and Y) and the $A - X - A$ path (except A and X) encoded with colors in Fig. 4.6. All semiconducting monolayer 1T'-TMDs except 1T'-WS₂ have their CBM located mostly along the $Y - \Gamma - Y$ path. The semiconducting monolayer 1T'-WSe₂ has its conduction bands lowered at the X point when deformed along lattice vector b . The location of the CBM of monolayer 1T'-MoS₂ is found away from the $Y - \Gamma - Y$ path regardless of the strain direction. The location of the CBM in this material may be switched multiple times before closing the band gap completely. The monolayer 1T'-WS₂ is the most uncharacteristic material in the family. There, high-symmetry points and directions are the least preferred ones for the CBM location. The monolayer 1T'-WS₂, strained or unstrained, is a semimetal with 4 electron pockets in most of the cases.

Robustness of the QSH phase in strained monolayer 1T'-TMDs

The semiconducting regions in Fig. 4.5 host the QSH phase which is supported by calculations of the topological invariant in Ref. [88]. The topological insulator phase cannot be changed without closing the band gap. However, the closing of the band gap does not necessarily change the topological invariant. Specifically, the topological invariant persists as long as

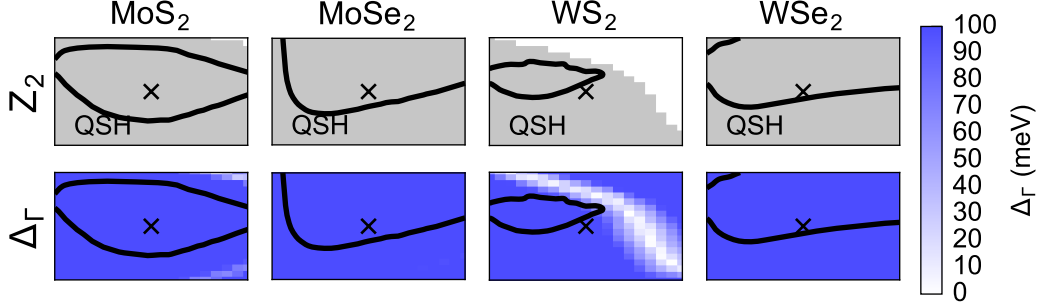


Figure 4.7 – The topological invariant phase in strained monolayer 1T'-TMDs. Top row: the Z_2 invariant calculated for valence bands as a function of lattice parameters in the 5% strain range. Grey color stands for the QSH phase. Bottom row: the magnitude of the band gap at Γ as a function of lattice parameters in the 5% strain range.

valence and conduction bands are isolated from each other:

$$E_i(k) \neq E_j(k), \forall k \in \text{BZ}, i \in \{V(\text{alence})\}, j \in \{C(\text{onduction})\}, \quad (4.1)$$

where $E_n(k)$ is the n -th Bloch band. The above condition guarantees a non-zero band gap at each point in the BZ, but not globally. Thus, some semimetallic systems may also be characterized by topological invariants.

Specifically, semimetallic monolayer 1T'-MoTe₂, WTe₂ as well as WS₂ were characterized in Ref. [88]. To complete the picture of the QSH phase in strained monolayer 1T'-TMDs an explicit calculation of the Z_2 invariant ν was performed using wavefunction parities[27] with the results presented in Fig. 4.7. The QSH phase in both monolayer 1T'-MoSe₂ and WSe₂ was found to be robust in the whole range of lattice parameters. The topological phase transition was found in monolayer 1T'-WS₂ and MoS₂ shown in Fig. 4.5. It occurs independently of the semiconductor-semimetallic phase transition and at larger strain values. However, the strain required to break the QSH phase in monolayer 1T'-WS₂ is relatively small due to the fact the band gap magnitude at Γ Δ_Γ is the smallest one in the family.

The relevance of the quantity Δ_Γ to the topological phase transition was confirmed by plotting it together with the value of the Z_2 invariant ν as a function of lattice parameters in Fig. 4.7. There, the change of the Z_2 invariant is always accompanied by vanishing $\Delta_\Gamma = 0$ while the opposite relation is, generally, not valid.

4.1.3 Summary

According to DFT predictions, monolayer 1T'-TMDs are prototypical two-dimensional topological insulators. The magnitude of the band gap in these materials is sensitive to lattice parameters: the small band gap in monolayer 1T'-TMDs is increased significantly with strain.

The largest magnitude of the band gap obtained occurs in selenides. It is also possible to close the band gap at various points in the BZ depending on the strain direction. The induced electron pockets appear either along high-symmetry directions in the BZ or away from them. The latter scenario was completely overlooked in previous studies where the band gap for both relaxed and strained materials was determined from electronic band structures along high-symmetry paths only. As a result, monolayer 1T'-WS₂ was claimed to be a semiconductor while, by fact, it is a semimetal. Moreover, the possibility for a strain-induced semiconducting phase is very limited in this material. The band inversion at the Γ point was found to be responsible for the QSH phase in all monolayer 1T'-TMDs. The observed topological strain-induced phase transition is accompanied by the closing of the band gap at the corresponding point.

4.2 Edges of monolayer 1T'-TMDs

The edges of a topologically non-trivial QSH phase in monolayer 1T'-TMDs may host topologically protected boundary modes. They are characterized by various unique properties such as protected charge carrier transport, the spin texture of states and Majorana fermions. The local conditions at the boundary play a crucial role in the above properties. For example, a termination carrying a non-zero magnetic moment breaks the topological protection and the underlying time-reversal symmetry. The edge mode may also cross the Fermi level more than once lifting protection of the charge carrier transport. Depending on the local atomic structure of a termination, various scenarios can be realized. Thus, the study of electronic properties of particular terminations is crucial for understanding how topological insulators can be used in practice.

The suggested edges to consider are periodic terminations along the shortest lattice vector in monolayer 1T'-TMDs: the zigzag edges. The latter include six different structures with a (1,0) periodicity corresponding to balanced, metal-rich and chalcogen-rich conditions and presented in Fig. 4.8(a). Within each pair, one of the structures is terminated closer to the zigzag chain while the other one includes an additional metallic atom. To investigate possible atomic reconstruction effects at the edges the structural relaxation calculations were carried out. A brief summary of simulation details are given in Appendix A.6.

The relaxed structures presented in Fig. 4.8(a) demonstrate only slight distortions compared to the bulk lattice. The most significant structural changes are found in balanced terminations (1) and (2) as well as in the chalcogen-rich termination (c1) where chalcogen atoms at the edge are undercoordinated. There is also a significant structural distortion at the metal-rich termination (m1) where the 3 rows of metallic atoms clusterize.

The six terminations considered differ in their formation energies E_b defined as

$$E_b = \frac{1}{2} (E_{\text{ribbon}} - N_M \mu_M - N_C \mu_C) , \quad (4.2)$$

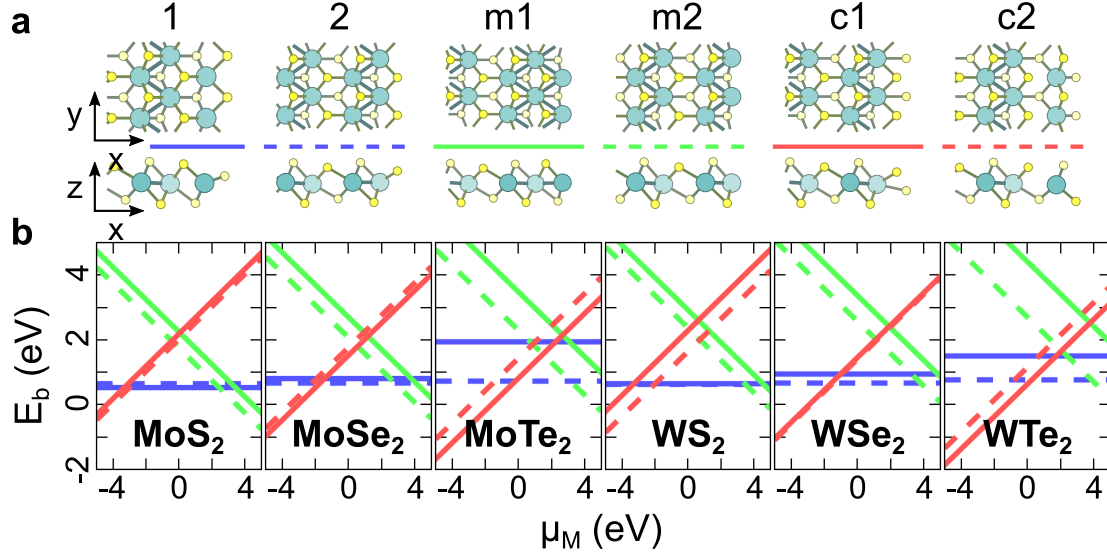


Figure 4.8 – Atomic structures of zigzag terminations in monolayer 1T'-TMDs and their formation energies. (a) Top and side views of atomic structures. (b) Formation energies of the boundary E_b as a function of a chemical potential of the metal atom μ_M for the six monolayer 1T'-TMDs considered. The colors of lines correspond to a particular defect in (a). The values the chemical potential μ_M are given with respect to the bulk bcc molybdenum for molybdenum-based compounds and with respect to bcc tungsten for tungsten-based ones.

where E_{ribbon} is the total energy of the nanoribbon with two equivalent edges, $N_{M,C}$ are numbers of metallic and chalcogen atoms in the model and $\mu_{M,C}$ are the corresponding chemical potentials. The chemical potentials are constrained by the formation energy of the corresponding bulk containing six atoms per unit cell

$$2\mu_M + 4\mu_C = E_{\text{bulk}}. \quad (4.3)$$

The formation energy is presented as a function of the chemical potential of the metal μ_M in Fig. 4.8(b) where the reference of the chemical potential is taken from the corresponding bulk body-centered cubic (bcc) structure $\mu_M = E_{\text{bcc}}$. There, pairs of parallel lines indicate the fact that the corresponding two terminations have the same stoichiometry, however, one of them has a smaller formation energy compared to the other one. For example, among metal-rich terminations (m1) and (m2) the latter is always preferred from the point of view of the formation energy E_b . Thus, the aforementioned clusters of metallic atoms require additional energy. The chemically-balanced terminations (1) and (2) are almost equal in their formation energies for sulfides and selenides while tellurides clearly prefer the second structure. The preferred terminations under chalcogen-rich conditions primarily depend on chalcogens: tellurides prefer the first structure, (c1), sulfides prefer the second structure, (c2), while the difference in formation energies of the structures for selenides is much smaller.

The electronic structures of zigzag edges differ significantly as confirmed by simulations of the

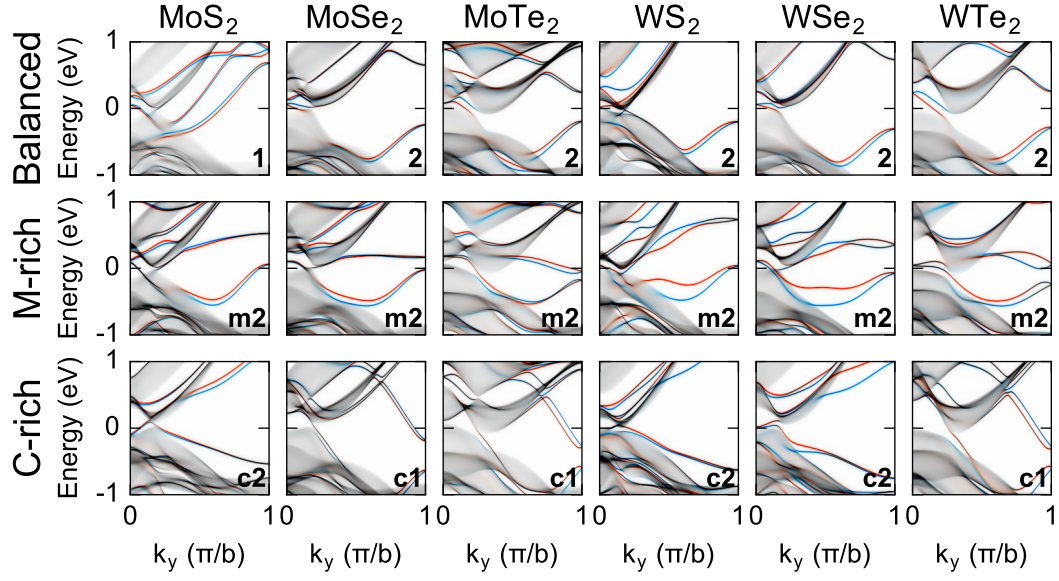


Figure 4.9 – The k -resolved density of states localized at the energetically preferred zigzag terminations of the six monolayer 1T'-TMDs presented in Fig. 4.8. The blue and red colors in each plot represent the contribution of out-of-plane spin-polarized states, spin-up and spin-down, to the total weight. The corresponding labels of atomic structures from Fig. 4.8 are indicated in each plot. The full range of plots including non-preferred terminations is presented in Appendix A.7.

local k -dependent density of electronic states presented in Fig. 4.9. The latter was calculated as an imaginary part of the Green's function trace from Eq. 2.67

$$n(E) = -\text{Im Tr } \mathbf{G}(E) \quad (4.4)$$

Up to eight spin-polarized modes are identified at the boundary. The character and the dispersion of edge modes depends on the termination structure. Thus, experimental observations of the local electronic structure at the boundary, such as STS, may be able to identify the kind of a boundary precisely. Specifically, chemically-balanced zigzag edges host only few modes mostly away from the Fermi level. Instead, metal-rich boundaries demonstrate a rather high density of electronic states close to the band gap. The electronic structure of a chalcogen-rich termination in monolayer 1T'-TMDs depends on the kind of preferred termination: while the (c1) termination hosts a pair of bands crossing the Fermi level, it is not the case for the (c2) termination. Thus, the choice of a material also influences the electronic structure of a boundary by means of the structure preferred. Provided the same atomic structure of the edge, however, the electronic structures of different materials presented in Fig. 4.9 (see also Fig. A.3) are very similar.

Most of the edge states are spin-polarized out of the material plane as indicated by color in Fig. 4.9. The spin polarization is usually preserved along a particular band selected. Both observations, however, are not the case for metal-rich termination (m2) especially in tungsten-

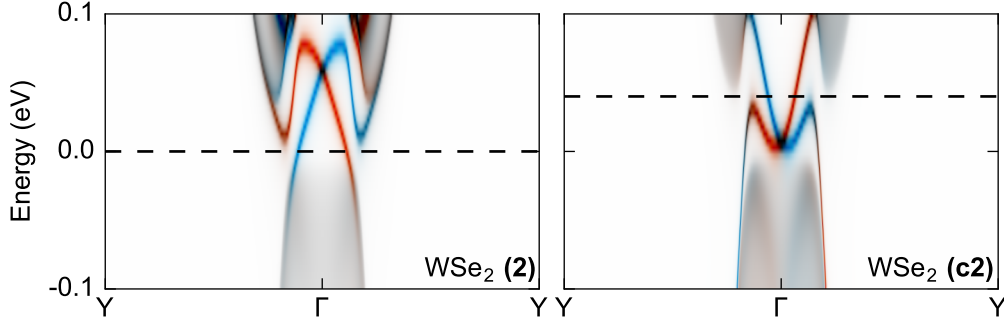


Figure 4.10 – Momentum-resolved localized density of electronic states of zigzag terminations suitable for the protected charge carrier ballistic transport experiment. The corresponding zigzag termination structure label is indicated in both plots. The horizontal lines are examples of energies at which the ballistic charge carriers are protected from backscattering.

based compounds. There, pairs of bands in the conduction energy region become spin-hybridized resulting in a non-uniform spin character of the band. The easy spin axis for hybridized edge states is away from the normal direction.

The topologically protected spin modes are identified for all boundaries by the odd number of Fermi level crossings. It is in agreement with the bulk-boundary correspondence of the QSH phase. The time-reversal symmetry is preserved by all zigzag edges. Thus, no magnetic moments are present and the spin degeneracy at TRIM points Γ and Y remains protected. Depending on the particular dispersion of the edge modes, the edge may support protected charge carrier ballistic transport. From this point of view, the most promising zigzag edges are those of monolayer 1T'-WSe₂ where two counter-propagating spin modes are present in the bulk band gap energy region as shown in Fig. 4.10. For both chemically balanced and chalcogen-rich terminations there exist ballistic charge carriers which are protected from backscattering. To identify them, one has to choose the energy of charge carriers carefully as, for example, illustrated by horizontal lines in Fig. 4.10. At the energies indicated, there exist only two quasiparticles with opposite spins and group velocities. Spin-neutral perturbations (such as local non-magnetic impurities, for example) do not couple these states. This, in turn, results in a completely suppressed back-scattering of the edge charge carriers and the protected charge carrier transport phenomena.

4.2.1 Summary

Periodic zigzag edges of monolayer 1T'-TMDs have been characterized in terms of structure, formation energy and electronic properties. For each material, among six terminations considered, three have a lower formation energy. These edges host localized gapless modes protected by the topologically non-trivial QSH phase and the underlying time-reversal symmetry. The spin texture of the corresponding modes as well as the odd number of Fermi level crossings

confirm that the states observed have a topological origin. As such, the protected charge carrier transport becomes possible provided the material and the edge are chosen carefully. Specifically, the two suggested zigzag edges in monolayer 1T'-WSe₂ are prototypical ideal nanowires where the charge carrier back-scattering is suppressed in a rather narrow energy region inside the band gap.

4.3 Electronic properties of structural phase boundaries in monolayer WSe₂

The topologically protected modes at the zigzag edges of monolayer 1T'-TMDs discussed in the previous section indicate the change of the topological invariant when leaving a 2D material bulk towards vacuum. The latter plays a role of a trivial insulating medium, however, it can be replaced by any topologically trivial insulating material with a finite band gap. The topologically protected edge states should persist as long as the trivial insulating material respects the symmetries of the corresponding topological classification. For example, the 2H structural phase of monolayer TMDs is in a trivial insulating QSH state under time-reversal symmetry and can complement the 1T' phase to induce topologically protected edge states.

The phase boundary between monolayer 2H- and 1T-TMDs prefers zigzag directions of the crystal lattice according to several experimental studies[87, 79, 86]. Also, recently, multiple 2H-1T' phase boundaries were observed in monolayer MoS₂ separating strips of the two phases parallel to the zigzag direction in the 2H phase[96]. The above studies mostly focus on transverse transport properties of a 2D metal-insulator interface. A relatively low Schottky potential barrier developed at the boundary allows an efficient injection of charge carriers into the semiconducting 2H phase of the material compared to more common contacts to gold or other bulk metals. The “patterning” of the metallic phase from the semiconducting 2H phase in TMDs is a practical way to build a lateral 2D device which is a major advantage over other materials.

The topological aspects of the phase boundary, however, have not yet been discussed. This section is dedicated to electronic structure properties of 2H-1T' interfaces in WSe₂ – a representative material where the band gap of the QSH phase can be tuned towards the largest values in the family.

As discussed, the 1T' phase of monolayer TMDs is formed from the stable 2H phase by shifting one of the chalcogen planes towards the previously unoccupied high-symmetry position in the hexagonal lattice. Thus, it is reasonable to expect that the lateral junction of the phases involves only a minor distortion of the other two atomic planes. There are only several configurations of a periodic phase boundary along the zigzag direction summarized in Fig. 4.11 where eight possible relaxed phase boundary structures are presented. Among them, four structures contain a 7-coordinated metal atom at the boundary (chalcogen-rich conditions) and four other structures contain a 5-coordinated tungsten atom (metal-rich conditions). Another

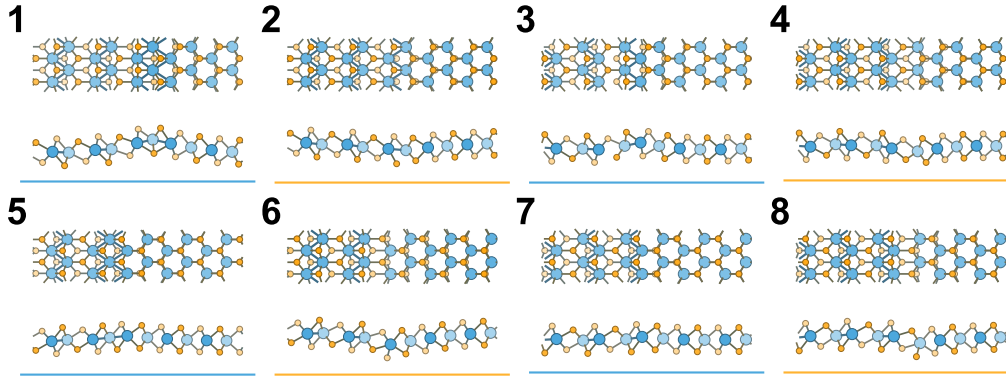


Figure 4.11 – Atomic structures of the 2H-1T' phase boundaries along the zigzag direction of monolayer WSe₂: top and side views. The colored line indicated tungsten-rich (blue) or selenium-rich (yellow) conditions.

degree of freedom to consider is the possibility to choose the crystallographic orientation of the polar monolayer 2H-TMD: panels (1-4) in Fig. 4.11 contain atomic structures with the same orientation of the monolayer 2H phase while panels (5-8) illustrate cases with the opposite orientation. Lastly, the boundary may or may not contain unpaired metal atoms which would otherwise form zigzag chains in the monolayer 1T'-phase¹.

The starting point for the description of electronic properties of the interface is the relative alignment of bulk bands presented in Fig. 4.12(a). In contrast to 3D materials, the band alignments in 2D do not generally depend on the interface structure. Thus, the relative alignment of bulk bands in 2D can be found by performing bulk calculations and matching the vacuum levels. In the case of WSe₂, this results in a type-III heterojunction: the small band gap of the 1T' phase remains at lower energies and does not overlap with the band gap of the 2H monolayer phase. The supercell configurations with a phase boundary, however, result in the Fermi level of the 1T' phase material² to be inside the band gap energy region of the 2H phase. The problem of the mismatch was previously reported for non-polar materials[97] and, essentially, is due to long-range electrostatic potentials spanning the supercell model. The weak logarithmic behavior of the potential prevents reasonably-sized supercell models to correctly reproduce the bulk band alignment. In experimental setups, however, the long-range potential is typically screened by localized charge carriers in the material or by the substrate.

The bulk states of both 2H and 1T' monolayer phases can also be identified in Fig. 4.12(b) where the local density of states at the phase boundary is presented. The overall picture of the electronic structure is quite complicated since spin-degenerate bulk states of the 1T' phase overlap with spin-polarized bulk states of the 2H phase together with several spin modes localized at the boundary. Compared to the “clean” bands presented in Fig. 4.10, neither of

¹This possibility, however, may effectively result in a strain applied across the phase boundary: for example, atomic and electronic structures 1 and 3, 6 and 8 presented in Figs. 4.11, 4.12(b) respectfully are very similar.

²The Fermi level is fixed to the middle of a small band gap in monolayer 1T'-WSe₂

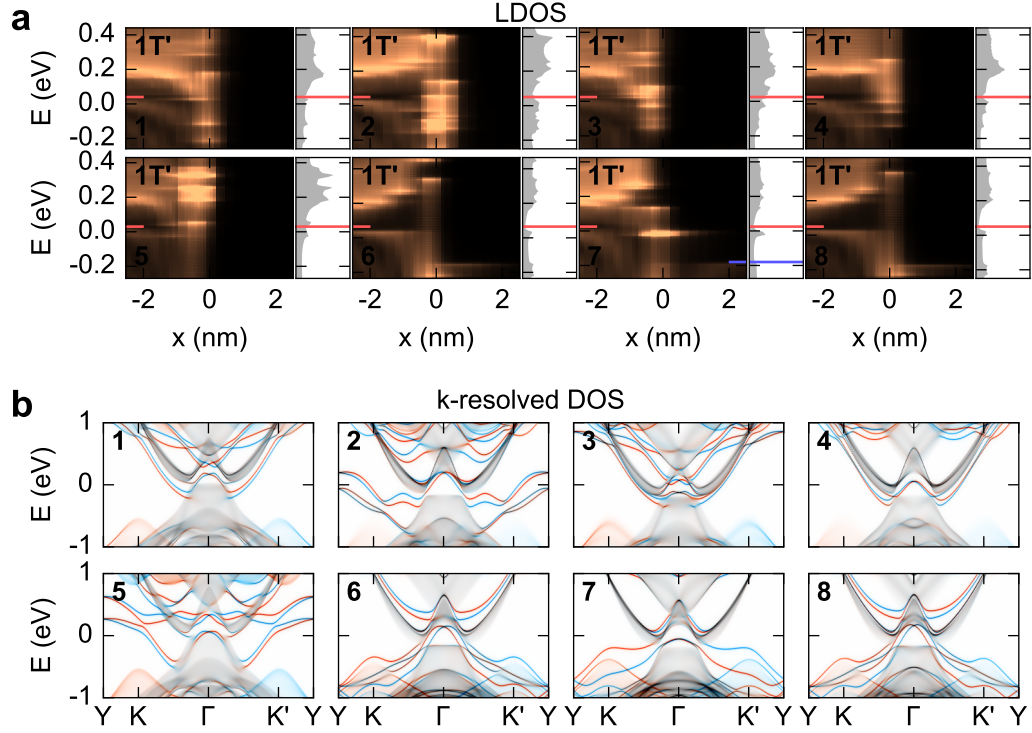


Figure 4.12 – Electronic structure of phase boundaries in monolayer WSe₂ displayed in Fig. 4.11. (a) Local densities of electronic states projected onto the direction perpendicular to the phase boundary. The DOS is presented in side plots. The Fermi level (red) of the 1T' phase as well as valence and conduction band edges of the 2H phase (blue) are indicated. (b) k -resolved DOS with the color (red,blue) indicating spin-up or spin-down character of the density.

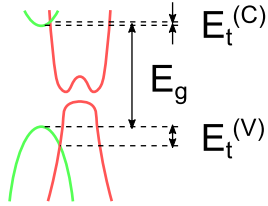
monolayer WSe₂ phase boundaries are suitable for charge carrier protected transport along the boundary. Nevertheless, all spin-polarized bands in Fig. 4.12(b) cross the Fermi level an odd number of times indicating the topological phase boundary. The spin character of boundary modes is not necessarily uniform and may change along the mode (see, for example, the second plot in Fig. 4.12(b)) similarly to edge modes of the 1T' phase discussed previously. Some of the spin modes presented in Fig. 4.12(b,6-8) originate from the bulk spin-polarized states belonging to K and K' valleys of monolayer 2H-WSe₂.

The ballistic transport properties of periodic phase boundaries are governed by energy and pseudomomentum conservation laws. The calculated transmission functions $T(E, k_{||})$ are presented in Fig. 4.13 together with bulk bands of both 2H and 1T' monolayer phases. As expected, the transmission function is non-zero only where bulk modes are available. In the case of the 2H monolayer phase, the bulk modes are mostly concentrated at K and K' valleys projected onto different points of the 1D BZ of a (1,0) phase boundary. Compared to the monolayer 2H-MoS₂ considered previously, the hole states originating from the Γ valley in monolayer 2H-WSe₂ are significantly lower in energy. The bulk modes of the 1T' monolayer

Chapter 4. Electronic properties of the distorted 1T structural phase in monolayer TMDs

phase reside at the Γ valley of the corresponding rectangular BZ. Thus, there is a mismatch of the projected pseudomomentum $k_{||}$ between leads' modes resulting in a non-zero transport gap E_t in addition to the bulk band gap of the 2H monolayer phase E_g . The latter in WSe₂ is as large as $E_g = 1.3$ eV. The magnitude of the transport gap depends on the relative band alignment of the phases, which, according to Fig. 4.12(a), depends on the actual atomic structure of the phase boundary. In all cases, the major contribution to the transport gap comes from the valence energy region while conduction bands contribute less. This results in a transport gap varying between 280 – 370 meV as summarized in the following table.

Table 4.2 – The magnitude of the transport gap E_t for charge carriers traveling across zigzag phase boundaries in monolayer WSe₂. The contributions to the transport gap in the valence energy region $E_t^{(V)}$ and in the conduction energy region $E_t^{(C)}$ of the monolayer 2H phase are indicated.



Structure	1	2	3	4	5	6	7	8
E_t , meV	280	340	350	340	280	350	370	360
$E_t^{(V)}$, meV	200	320	350	340	200	350	370	360
$E_t^{(C)}$, meV	80	20	0	0	80	0	0	0

The good transparencies of phase boundaries reported previously are in agreement with the ballistic transport simulation results presented. However, this statement does not directly follow from the plots presented in Fig. 4.13 where most transmission probabilities are exactly zero due to the absence of bulk states at a given $k_{||}$ and E . Thus, it is instructive to consider only those charge carriers which, according to the conservation laws, are able to transmit. Such charge carriers are found at the overlap between bulk bands presented in Fig. 4.13 where both 2H and 1T' bulk modes have the same $k_{||}$ and E . It is possible to assign the maximum possible value of the transmission function for these charge carriers defined as

$$T_{\max}(E) = \int dk_{||} \min [n_{2H}(E, k_{||}), n_{1T'}(E, k_{||})] , \quad (4.5)$$

where $n(E, k_{||})$ corresponds to the number of bulk modes of a specific phase at a given point in the parameter space. The ratio T/T_{\max} , $T = \int dk_{||} T(E, k_{||})$, may be viewed as a measure of the transparency of a non-periodic phase boundary. The calculated values of the above ratio are presented in Fig. 4.14 (blue lines). The ratio typically exceeds 0.1 indicating good transport properties of the phase boundaries considered. Close to band edges, however, the ratio may drop down to 10^{-2} or even below which is typical for modes with a small group velocity.

Finally, another indicative quantity is $T/T_{\max, 2H}$ with $T_{\max, 2H}$ defined as

$$T_{\max, 2H}(E) = \int dk_{||} n_{2H}(E, k_{||}) . \quad (4.6)$$

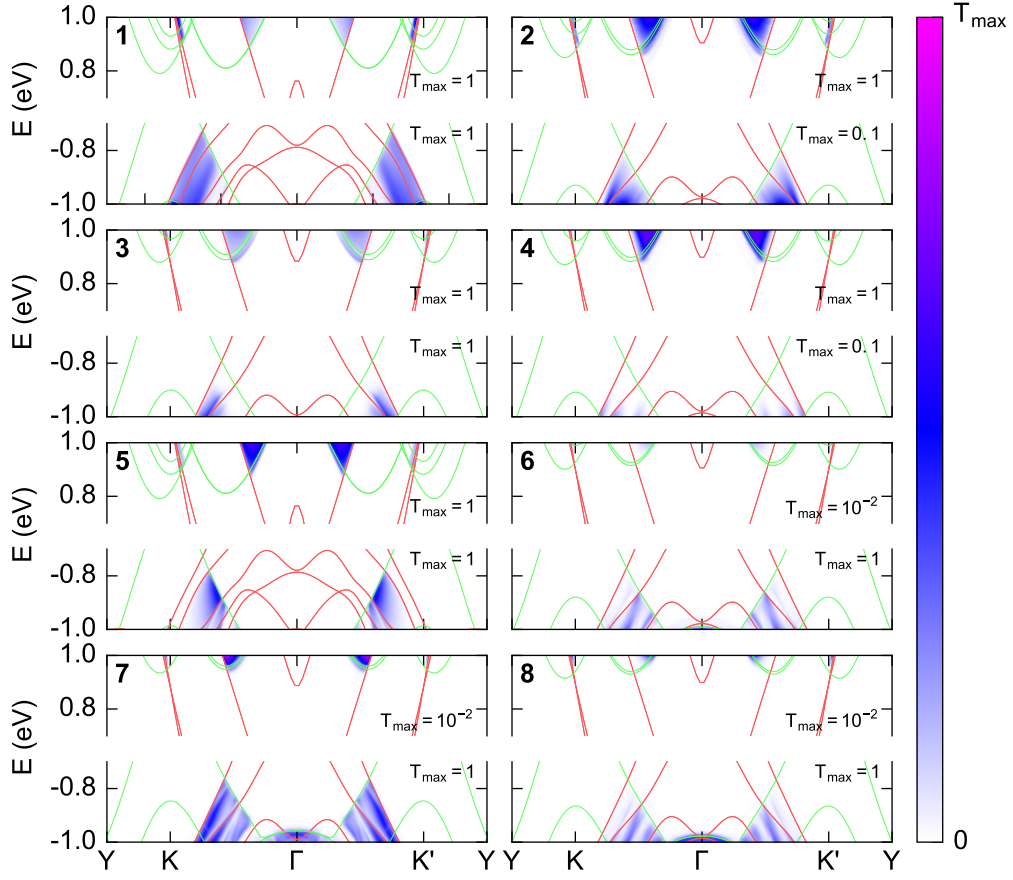


Figure 4.13 – Charge carrier transmission function of the 2H-1T' phase boundaries in monolayer WSe₂ displayed in Fig. 4.11. The color indicates the value of transmission normalized by the corresponding maximum indicated in each subplot. The contours of bulk 2H and 1T' monolayer phase bands are shown in each plot.

It is proportional to a maximum possible conductance in the 2H monolayer phase in the ballistic transport regime. Thus, the above ratio can be used to compare *different materials* in terms of their contact properties to the semiconducting 2H phase. The calculated ratio is presented in Fig. 4.14 as a function of the energy E using red lines. Obviously, $T/T_{\max,2H} < T/T_{\max}$ though both values are of the same magnitude. As a result, $T/T_{\max,2H}$ is typically between 10^{-1} and 10^{-2} , however, it may reach higher values away from the band gap region.

4.3.1 Summary

The zigzag boundaries between monolayer 2H and 1T' phases of WSe₂ were evaluated from the point of view of structural, electronic and transport properties. The topological character of the boundary is found be consistent with the number, spin character and energy dispersion

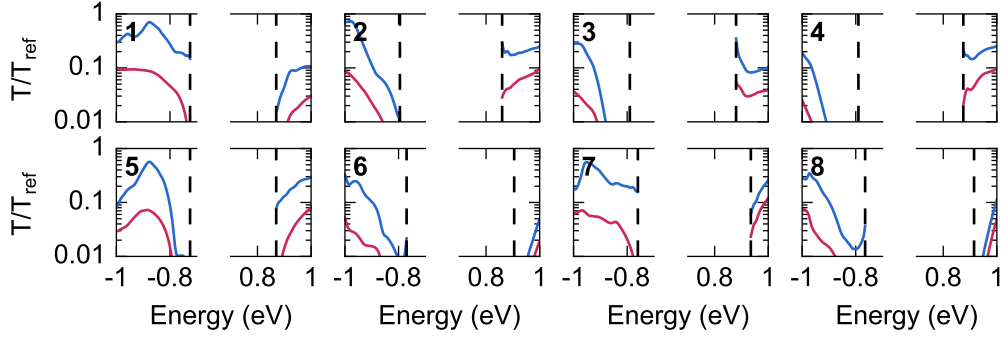


Figure 4.14 – Relative transmissions T/T_{ref} of the phase boundaries in WSe_2 displayed in Fig. 4.11. The blue plots compare the transmission function T to the maximum possible transmission T_{ref} via the open channels of a particular heterojunction. The red plots compare the transmission function T to the maximum possible transmission T_{ref} in the 2H phase of the monolayer WSe_2 . The edges of a transport gap are indicated by vertical lines.

of electronic bands at the boundary. The possibility of employing 2H-1T' phase boundaries for topologically protected charge carrier transport, however, is unclear since multiple in-gap states contribute to transport properties inside the bulk band gap of monolayer 1T'- WSe_2 . Otherwise the high transparency of boundaries for transverse charge carriers is confirmed by the transport calculations. The contribution to the transport gap of around 300 meV is found to be consistent with alignment of bulk bands of both monolayer phases in WSe_2 .

4.4 Electronic properties of dimerization defects in monolayer 1T'- WSe_2

Several previous sections were dedicated to line defects and domain boundaries in the 2H phase as well as phase boundaries between the 2H and 1T' phases of monolayer TMDs. To complete the family of line defects in monolayer TMDs, the dimerization defects in the 1T' phase have been studied.

Unlike the line defects considered, the dimerization defects in the monolayer 1T' phase are stoichiometric. Stoichiometric defects are characterized by lower formation energies and higher concentrations under thermodynamic equilibrium. In the context of the previous discussion, the semimetallic 1T' phase plays a role of a lateral contact in a semiconducting 2D device. Thus, the electronic properties of the 1T' monolayer phase are important. The high defect concentration may affect the properties of the monolayer 1T'-TMDs. From the point of view of applications, one would also expect a quasi-amorphous phase of the monolayer 1T' phase where the concentration of dimerization defects is maximal. Such phase may demonstrate completely different properties compared to the crystalline monolayer 1T'-TMD. This gives an additional degree of freedom when engineering a 2D device similar to crystalline

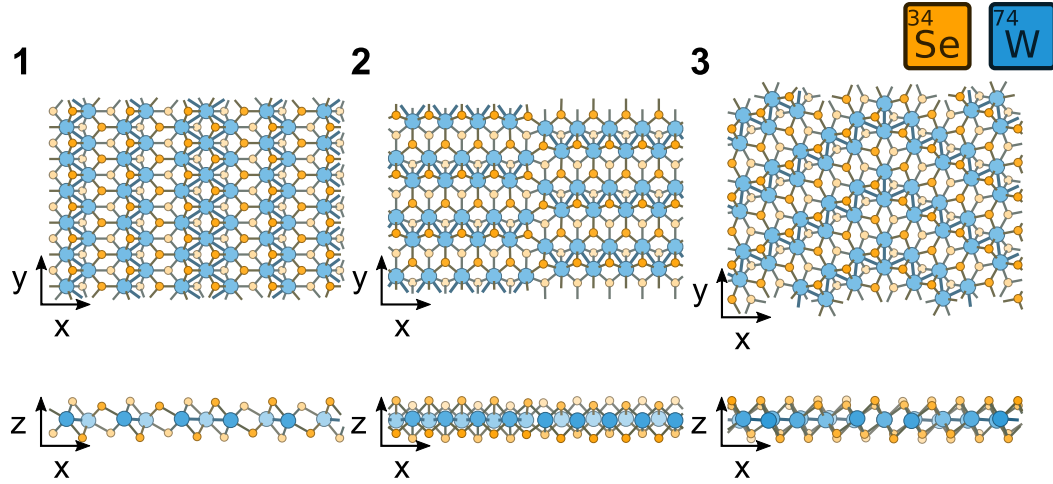


Figure 4.15 – Atomic structures of 1T' periodic dimerization defects in monolayer WSe₂: top and side views. (1) A dimerization defect along the shortest unit cell dimension (zigzag). (2) A dimerization defect along the longest unit cell dimension (armchair). (3) A 120° dimerization defect separating domains with different orientations of the monolayer 1T'-WSe₂ lattices.

and amorphous silicon currently used in nanoelectronics.

At the time of writing of this thesis, not much information exists on dimerization defects in the 1T' phase of monolayer TMDs. A quasi-crystalline phase of a sodium-intercalated multilayer 1T-MoS₂ observed in Ref. [84] provides a hint of how a 1T' dimerization defect could look like. In particular, the dimerization defect may join domains with different directions of the zigzag distortion as shown in Fig. 4.15(3). This case corresponds to approximately 120° rotation of corresponding crystallographic directions at both sides of the defect. Other possibilities include breaking of the zigzag distortion without rotating the lattice as illustrated in Fig. 4.15(1,2). There, periodic dimerization defects are parallel to the shortest or to the longest vector of a monolayer 1T'-TMD unit cell. All defects keep the underlying monolayer 1T phase intact, thus, the relaxed structures presented in Fig. 4.15 experience only slight structural distortions at the defect. For consistency with the previous section, the discussion further is constrained to monolayer 1T'-WSe₂ only.

The “zigzag” dimerization defect illustrated in Fig. 4.15(1) originates from a single unpaired line of tungsten atoms. The relaxed structure, however, prefers to form a triple metallic chain by merging the single and the bulk-like double chains. Thus, tungsten atoms in the middle become over-coordinated. The corresponding distance between tungsten atoms 3.04 Å slightly exceeds the corresponding bulk value of 2.81 Å but is still much smaller than the off-chain W-W distance in the bulk 4.05 Å.

The “armchair” dimerization defect illustrated in Fig. 4.15(2) breaks metallic chains and rejoins them in a zip-like manner. As introduced, the periodicity vector for the line defect is bigger in this case: it is equal to the largest dimension of the unit cell. Both zigzag and armchair defects

Chapter 4. Electronic properties of the distorted 1T structural phase in monolayer TMDs

Table 4.3 – Formation energies of dimerization defects in monolayer 1T'-WSe₂. The energies are given per unit length. Formation energies of chemically balanced zigzag edges of monolayer 1T'-WSe₂ from Fig. 4.8 are given for comparison purposes.

	Zigzag defect (1)	Armchair defect (2)	120° defect (3)	Edge 1	Edge 2
E_{form} , meV/Å	265	131	58	286	200

connect domains of monolayer 1T'-WSe₂ with the same crystallographic orientation. Thus, they can be avoided by a parallel shift of atoms at one side of the defect. It is not the case for the 120° dimerization defect, Fig. 4.15(3). Unlike the previous defects, it does not possess an inversion symmetry at the defect line: it joins two 2D crystals rotated with respect to each other by approximately 120°. As such, the directions of dimerizations in the two crystals are different in this case and require a rotation in real space to match.

The dimerization defects considered differ significantly in terms of their formation energies, E_{form} in Table 4.3. The most preferred defect is the 120° dimerization defect with the formation energy as low as 58 meV per angstrom. The armchair defect is more than two times expensive in energy while the zigzag defect requires four times more energy to form. This observation has two important consequences. First, the relatively low formation energy of the 120° dimerization defect may cause its high concentrations in real samples as argued in the beginning of this section. Second, the breaking of the zigzag dimerization of metallic atoms in the zigzag defect as well as in certain zigzag edges, Fig. 4.8(a), requires significantly more energy. Compared to chemically-balanced zigzag terminations, the dimerization defects break less chemical bonds, thus, are expectedly lower in their formation energies³.

All three periodic dimerization defects considered result in different 1D defect Brillouin zones both in terms of its size and orientation with respect to the leads. The largest BZ is for the zigzag defect while the smallest one is for the 120° dimerization defect. The high-symmetry points Γ , X, Y of the monolayer 1T' phase BZ are projected differently as indicated in respective panels in Fig. 4.16(a). There, either Γ and X or Γ and Y or X and Y are projected onto the same point of the 1D BZ. This fact prevents the direct comparison of electronic structure properties of the three defects.

Among the three dimerization defects, only the zigzag dimerization defect shows a clear presence of localized gapless modes shown in Fig. 4.16(a,1). In contrast, the dimerization defect along the armchair edge does not cause closing of the small band gap. In both cases, all localized states are spin-degenerate due to the presence of time-reversal and inversion symmetries. The 120° dimerization defect is different from this perspective: the states localized at the defect have a pronounced spin character as shown in the inset in Fig. 4.16(a,3). It is possible because of the lack of an inversion symmetry in the atomic structure. The band gap is closed or less than the imaginary part of the energy used in Green's function calculations, 5

³While the formation energy of the edge presented in Table 4.3 belongs to a single monolayer bulk phase of a 1T' TMD, the formation energies of dimerization defects are "split" between the two grains connected by the defect.

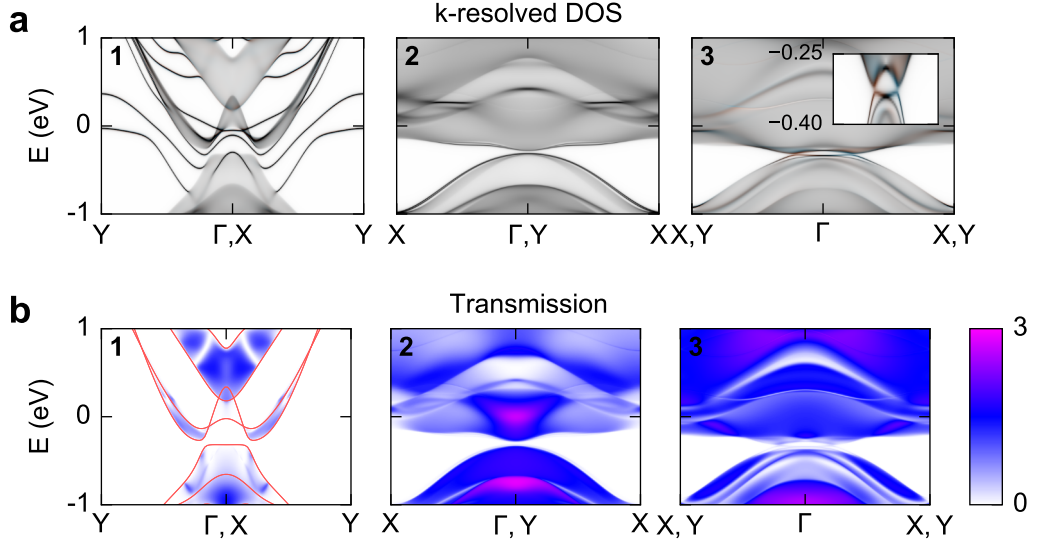


Figure 4.16 – Electronic structure properties of dimerization defects in monolayer 1T'-WSe₂ from Fig. 4.15. (a) The k -resolved density of electronic states. The blue and red colors on the third panel indicate the spin-up and spin-down character, respectively, of the density for the non-inversion-symmetric grain boundary. The inset shows density of states in the vicinity of the band gap. (b) The k -resolved charge carrier transmission functions T for charge carriers traveling across dimerization defects. The color indicates the value of transmission. The bulk bands plotted along high-symmetry directions are shown for the first defect.

meV in this case.

The calculated transmission functions for transverse charge carriers indicate a high transparency of all three defects, Fig. 4.16(b). This can be attributed to the fact that all 3 defects preserve the lattice structure and stoichiometry to a large extent. Moreover, unlike the monolayer 2H phase, the 1T' phase is non-polar and has a much smaller band gap, thus, the small charges accumulated at the defects are screened effectively. This reduces the effects of an electrostatic repulsion in the charge carrier transport. While, looking at Fig. 4.16(b), the transmission across the first defect is subjectively smaller, it effectively corresponds to the smallest period among all three defects. Thus, the pseudomomentum conservation law for this defect is pronounced most: there is a large region in the $(k_{||}, E)$ space bounded by the band edges (red lines in the figure) where no bulk modes are present and no charge carriers transmit.

4.4.1 Summary

The structure, electronic and charge carrier transport properties of simplest stoichiometric dimerization defects in the 1T' phase of monolayer WSe₂ were investigated. The relaxed structures of dimerization defects exhibit only moderate structural reconstruction such as the formation of a triple line of metallic atoms at the line defect along the shortest lattice vector.

Chapter 4. Electronic properties of the distorted 1T structural phase in monolayer TMDs

Otherwise local environments of atoms at the defects do not change. Nevertheless, a clear presence of localized modes at the zigzag defect was observed. In the case of an armchair defect, however, the modes do not close the band gap in the material. The absence of an inversion symmetry for the 120° dimerization defect lifts the spin degeneracy and causes localized modes to be spin-polarized. The charge carriers, both holes and electrons, exhibit high transmission probabilities across all defects considered. It is attributed to the fact that the monolayer 1T' phase is non-polar and has a small band gap causing additional charges accumulated at defects to be screened effectively.

4.5 Conclusions

The 1T' phase of monolayer TMDs attracts interest from various perspectives. On the one hand, being semimetallic, it complements the semiconducting 2H phase with applications in lateral 2D devices. On the other hand, it is a topologically non-trivial phase in the QSH regime with applications in spintronics and quantum computing. The studied sensitivity of the band gap and the band order in the 1T' phase to strain provides a way to both maximize the band gap and to close it, depending on application requirements. For gapped systems, the QSH phase was confirmed by studying edges of monolayer 1T'-TMDs. The spin-polarized edge modes were also confirmed for semimetallic tellurides as well as WS_2 which was previously considered to be a semiconductor. Specific edges of the monolayer 1T' phase were suggested for protected transport experiment making TMDs to be the first realistic QSH insulator.

The study of structural and electronic transport properties of phase boundaries between the 2H and 1T' monolayer phases as well as line defects in the 1T' phase complements the study of line defects in the 2H semiconducting materials presented in the previous chapter. The transparency of 2H-1T' boundaries for transverse ballistic charge carriers is affected by the transport gap caused by the difference between shapes of bands of the two phases. Both phase boundaries and line defects in the monolayer 1T' phase are transparent for charge carriers though the relative alignment of bands of the two phases does play a role in the transport process. The good transparency of defects is in agreement with previous experimental studies and the fact that the charges in narrow-band-gap materials are screened effectively.

5 Simulating STM images of point defects in spin-orbit systems

Scanning probe microscopies such as scanning tunneling microscopy (STM) provide an important insight into the surface structure and properties at the atomistic-scale level. As described in one of previous sections, such level of spatial resolution is possible with the help of an atomically sharp tip scanning the material and measuring tunneling conductance. As a result, a topographic image is recovered where individual atoms and molecules can be recognized.

An image generated by STM may still be a challenge to interpret due to the fact that a rather complicated process of electron tunneling is involved in its generation. For example, the same surface defect may have a qualitatively different contrast in images taken under different conditions of the STM setup. However, by combining different experimental and theoretical techniques it becomes possible to identify the defect atomic structure and its electronic properties.

This chapter describes results of research performed in a close collaboration with experimental groups towards identifying point defects in two systems: a surface of a Bi_2Te_3 topological insulator and a monolayer 2H-MoSe_2 .

5.1 Magnetic adatoms on the surface of Bi_2Te_3

As discussed in previous chapters, 3D TIs, such as Bi_2Te_3 , host topologically protected metallic states on the surface. However, if the time reversal symmetry is broken, the topological protection is lifted and the electronic band gap on the surface may be opened[98]. One of the ways to break the time-reversal symmetry is to introduce local magnetic moments. This can be done by depositing magnetic adatoms, such as Fe, on the surface of a 3D TI. The properties of such dopants motivated the joint research presented in Ref. [99] where I contributed the structural identification of dopants and calculations of their magnetic properties.

Two kinds of dopants were identified in the STM experiment. The dopants were observed as triangular and trefoil-shaped features, see Fig. 5.1. The underlying sublattice formed

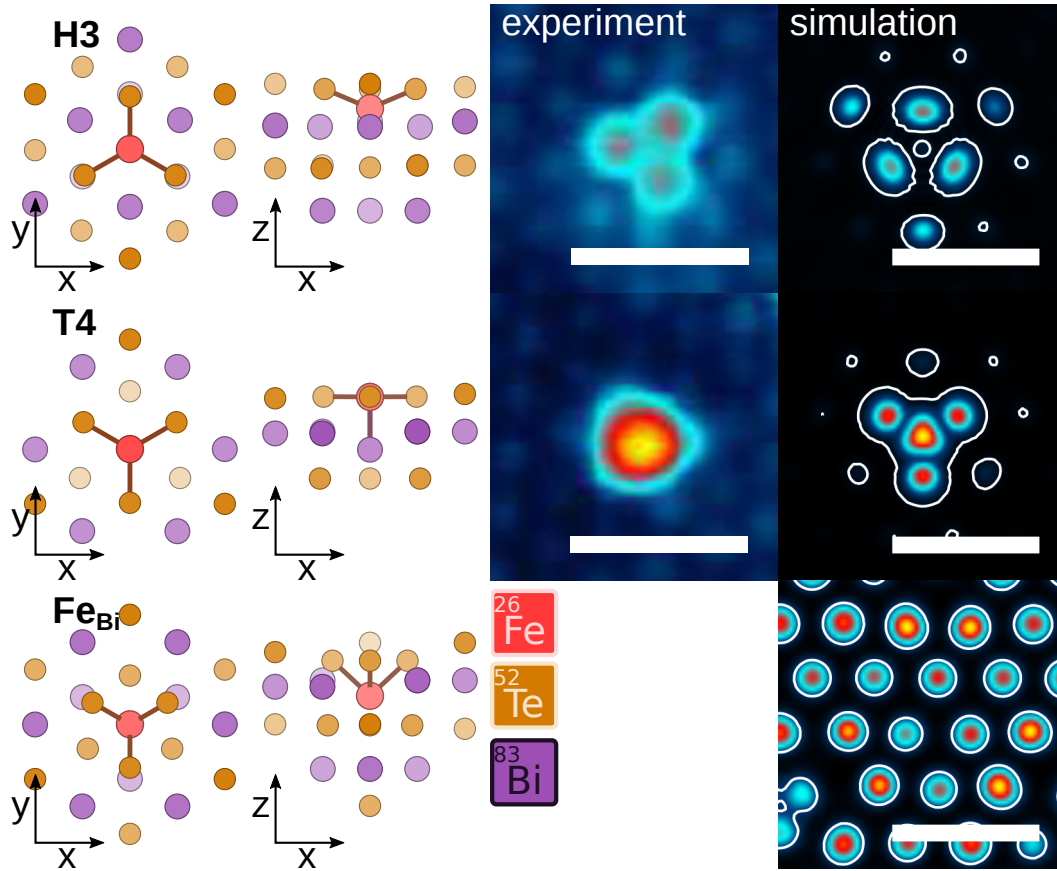


Figure 5.1 – Fe dopants on the surface of Bi_2Te_3 in 3 possible configurations: H3 (Fe above Te), T4 (Fe above Bi) and Fe_{Bi} (Fe substituting topmost Bi). The relaxed structures are presented on the left. The simulated STM images together with corresponding STM images observed in experiment are presented on the right. The STM bias voltage from experiment -0.4 V corresponds to the simulated local density of hole-like states. White scale bars are 1 nm.

by the topmost Te atoms is also visible in the experimental images. This allows assigning dopants to different high-symmetry positions of the lattice: H3 (on top of the tellurium atom in the third topmost layer) and T4 (on top of the bismuth atom in the second topmost layer). To identify which high-symmetry position corresponds to which STM image the electronic structure calculations and simulations of STM images have been performed. By comparing experimental and simulated images in Fig. 5.1 it is possible to assign the atomic structure of the H3 adatom to the trefoil-shaped signal and the one of the T4 structure to the triangular-shaped signal. As expected, the iron atom in the H3 configuration relaxes deeper into the surface of Bi_2Te_3 , thus, producing a less intense signal in the STM image. In contrast, the second topmost layer of Bi atoms in the T4 configuration prevents further depression of Fe into the material resulting in a bright spot in the image. To verify that the Fe adatom in the T4 configuration does not replace the underlying Bi we also performed simulations with the latter removed from the atomic structure. The resulting STM image, bottom row of Fig. 5.1, shows a very weak signal from the impurity which was not identified in the original experimental data.

5.1.1 Thermodynamical properties of adatoms

The adatoms deposited in the experiment were found to be immobile at cryogenic temperatures of $T = 10$ K. The concentration of Fe adatoms in the H3 atomic configuration, however, was found to be slightly larger. As reported in Ref. [99], the ratio between concentrations $\rho_{\text{H3}}/\rho_{\text{T4}} \approx 3/2$. These two facts suggest that the H3 configuration is thermodynamically more stable than the T4 configuration, while the potential barrier between the configurations is too large for thermally-activated transition between them.

To verify this hypothesis the total energy profile between the H3 and the T4 configurations was plotted using the nudged elastic band (NEB) method[100]. The calculation details are given in Appendix A.8. The resulting potential profile shown in Fig. 5.2(a) implies that the H3 configuration to be more energetically favorable. Depending on the inclusion of the on-site Coulomb repulsion term for the d -states of Fe[101] $U = 3$ eV, the energy difference between the configurations is 0.25 eV (without) or 0.37 eV (with the Coulomb repulsion). The energy barrier separating configurations is around 1 eV. The barrier is too high for the thermal diffusion at $T = 10$ K, thus, under experimental conditions the Fe atoms are immobile. The relative concentrations of the impurities are rather defined by the kinetic aspect of the deposition process and, in principle, are not related directly to the relative energies of the two configurations.

5.1.2 Electronic and magnetic properties of adatoms

As mentioned earlier, magnetic impurities may open a band gap¹ in the surface Dirac cone via exchange interaction with helical surface states[98, 35, 37] depending on the direction of the magnetic moment. The electronic structure results of the STS experiment did not show any evidence of coupling of helical spins and magnetic moments of Fe adatoms. On the other hand, the x-ray absorption spectroscopy and x-ray magnetic circular dichroism experiment results[99] show an out-of-plane magnetic anisotropy of Fe adatoms which, in principle, is expected to open the band gap in the Dirac cone. To provide an additional insight into the electronic properties of Fe adatoms on the surface of Bi₂Te₃ *ab-initio* DFT simulations were carried out.

The electronic band structures calculated for both H3 and T4 atomic configurations and presented in Fig. 5.2(c,d) do not allow any definitive conclusions with regard to the band gap since the Dirac cone at the Γ point is buried in a multitude of metallic states due to impurity. This is due to a relatively small 2x2 supercell employed in the calculations: the Fe adatom interacts with its images resulting in dispersive bands with a high weight of Fe orbitals shown in Fig. 5.2(c,d). Similarly, the densities of electronic states plotted in Fig. 5.2(b) do not exhibit any sharp peaks either.

To understand the magnetic properties of adatoms several DFT simulations were performed.

¹Provided the Fermi level is at the Dirac cone touching point

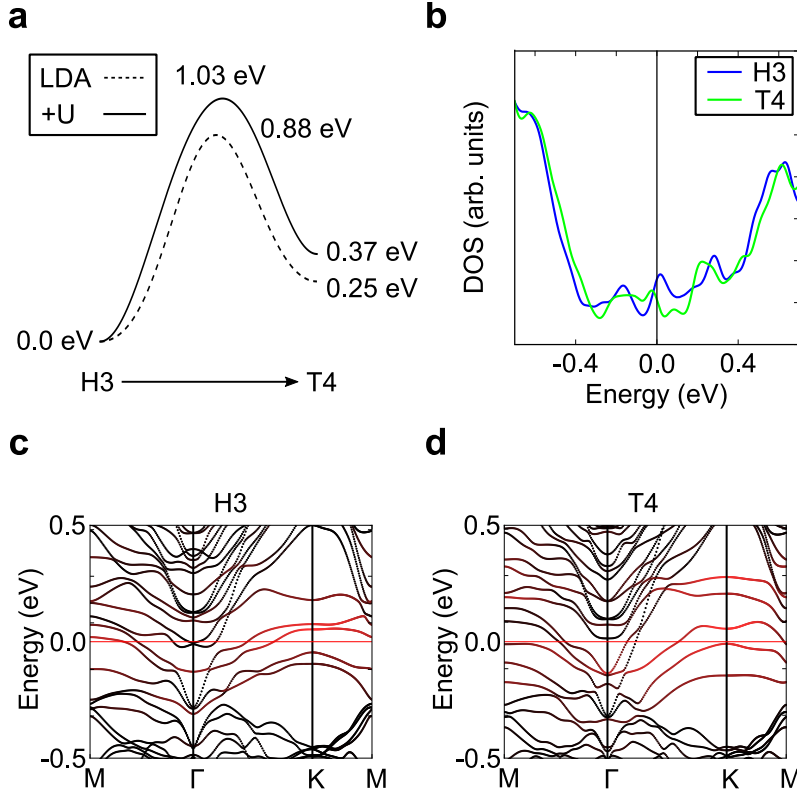


Figure 5.2 – Electronic properties of Fe adatoms on the surface of Bi_2Te_3 . (a) The energy profile between H3 and T4 configurations. The horizontal direction is a generalized coordinate. (b) Electronic densities of states near the Fermi level. (c,d) Electronic band structures of 3×3 supercell slab models with Fe adatoms. The red color corresponds to bands with a high contribution of Fe orbitals.

Specifically, the spin axis for Fe was constrained to in-plane and out-of-plane directions. Without inclusion of the Coulomb repulsion, the energy difference between the two magnetic configurations is rather small: of the order of μeV . However, the magnetic anisotropy of iron adatoms is usually underestimated by the conventional DFT and the inclusion of additional Coulomb repulsion terms is necessary. Thus, a series of LDA+U calculations was carried out. The results of the calculations show a clear trend for the magnetic moments to align out-of-plane: the in-plane configurations are higher in energy by 12.2 meV for the H3 site and 9 meV for the T4 site per Fe adatom (the magnetic anisotropy value K in Ref. [99]). This is in agreement with the experimental data, Fig. 3 of Ref. [99]. The orbital m^L and spin m^S out-of-plane magnetic moments calculated for Fe adatoms are summarized in the following table.

Table 5.1 – Magnetic properties of Fe adatoms on the surface of Bi₂Te₃: magnetic moments and anisotropies calculated by projecting occupied Bloch states onto atomic orbitals.

	$m^S (\mu_{\text{Bohr}})$	$m^L (\mu_{\text{Bohr}})$	$K (\text{meV})$
H3	2.7	0.7	12.2
T4	2.5	0.3	9

5.1.3 Conclusions

Results of our theoretical simulations of Fe impurities on the surface of Bi₂Te₃ are well in line with experiments. Simulations of STM images allowed us to assign unambiguously H3 and T4 atomic configurations of Fe adatoms to the corresponding experimental results. As confirmed by the NEB method, the large energy barrier separating two configurations allows simultaneous observation of both kinds of impurities at experimental conditions. While there is no conclusive agreement on electronic properties of Fe adatoms, their magnetic properties are in a good agreement between theory and experiment. The calculated orbital and spin magnetic moments suggest that Fe adatoms are in a high-spin state. The out-of-plane magnetic anisotropy of Fe observed in this work is also in agreement with previous predictions[102, 103] and observations[104].

5.2 Selenium vacancies in monolayer 2H-MoSe₂

As discussed in previous chapters, 2D materials are susceptible to various structural defects including line and point defects. Our experimental colleagues from Lawrence Berkeley National Laboratory observed several kinds of point defects in MoSe₂ with STM signal changing both qualitatively and quantitatively as a function of the voltage applied to the STM tip. Surprisingly, the defects did not show any sign of in-gap states in STS measurements. In contrast, all defects in a sister material MoS₂ are predicted to have in-gap states[105]. We attempted to perform a similar study for monolayer 2H-MoSe₂: to identify the defects and to calculate their electronic properties.

For 2D MoS₂, the most expected point defect predicted[105] is the sulfur vacancy V_S. Accordingly, the selenium vacancy V_{Se} is the most expected point defect in MoSe₂. Provided the stoichiometric balance between molybdenum and selenium atoms is shifted towards selenium-deficient conditions, one may also expect a defect configuration of a molybdenum atom substituting one Mo_{Se} or two Mo_{2Se} selenium atoms. I performed electronic structure calculations of the above defects in a supercell geometry (computational details are given in Appendix A.9) with results presented in Fig. 5.3.

As expected, all defects induce in-gap states localized at the defect, last column in Fig. 5.3. The defects induce several empty and occupied states in the band gap energy region as demonstrated in the corresponding DOS plots in Fig. 5.3. The simulated STM images also indicate the presence of defect states in all cases. The largest intensity obtained during

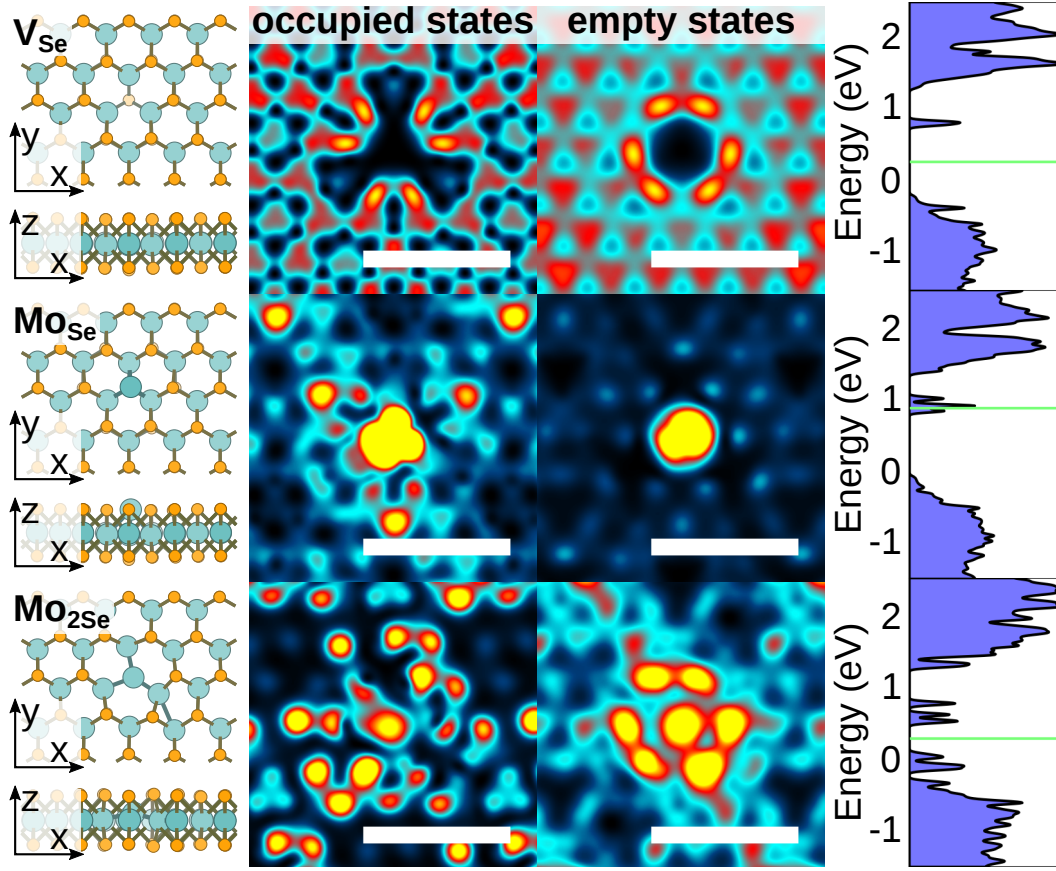


Figure 5.3 – Atomic structure and electronic properties of point defects in monolayer 2H-MoSe₂. For the three defects considered, V_{Se}, Mo_{Se} and Mo_{2Se}, top and side views of an atomic structure (left), simulated STM images (middle) and electronic densities of states (DOS) (right) are plotted. The turquoise color in images of the atomic structure corresponds to molybdenum atoms while orange circles are selenium atoms. The color scale across simulated STM images is different. The scale bar is 1 nm. Occupied and empty states correspond to integrated DOS 100 meV below the bulk valence bands maximum and 100 meV above the bulk conduction bands maximum respectively. The zero energy level in DOS plots is fixed to the top of valence bands of pristine monolayer 2H-MoSe₂. The horizontal green lines indicate Fermi levels of defective systems.

simulations corresponds to the Mo_{Se} defect where the Mo atom protrudes from the material plane significantly. The Mo_{2Se} defect induces significant distortion of electronic density on a larger length scale.

The defects observed in STM and atomic force microscopy (AFM) images preserve the 3-fold symmetry of the ideal MoSe₂ lattice. The simulations show that both atomic structure and the density of electronic states presented in Fig. 5.3 have the same symmetry only in the case of the selenium vacancy V_{Se}. This implies that all defects observed are Selenium vacancies located at one of the two chalcogen planes of monolayer 2H-MoSe₂. Correspondingly, two types of

intensity signatures corresponding to the V_{Se} defect are visible in STM: one corresponds to the vacancy just below the STM tip (the vacancy side) and the other one corresponds to the vacancy below the material plane (the back side).

5.2.1 Electronic properties of Se vacancies

To further understand electronic properties of Se vacancies in MoSe₂ additional electronic structure simulations were performed. Motivated by the STS data showing no in-gap states of the defect, the specific focus was made on defect electronic states. As shown in Fig. 5.3, a single selenium vacancy hosts localized electronic levels close to the edge of conduction band. For the charge-neutral system these states remain unoccupied. Upon adding electrons to the system these states start getting populated and the Fermi level of the system moves up in energy. To understand, whether this is the only effect on the electronic band structure, additional simulations were carried out.

To simulate a charged selenium vacancy two additional models were considered. The first model, $V_{Se} + e$, included an additional electron explicitly such that the total charge of the supercell model was equal to the electron charge $-e$. The second model, H_{Se} , realized another possibility of a hydrogen adatom absorbed by the defect. The latter donates an electron to the defect, thus, only minor change in electronic properties compared to the $V_{Se} + e$ case is expected. Both models were relaxed prior to calculating the density of states.

The calculated densities of electronic states presented in Fig. 5.4 show that the localized states are still present in the band gap energy region in all cases considered. As expected, the Fermi level shifts towards the conduction band. In the case of a hydrogen adatom, the spin degeneracy of states is lifted and the total magnetic moment of the model is equal to μ_{Bohr} . Four separate peaks corresponding to localized states at the defect are visible in Fig. 5.5. In either case, charging of defects does not explain the absence of in-gap states in experiment.

There is a good agreement between experimental and simulated STM images in Fig. 5.5. All vacancy-side images, experimental and simulated, exhibit a contrast depression corresponding to the defect center. The contrast peaks have the same symmetry when comparing the simulated and the experimental images. The agreement between the images corresponding to the back side of the defect, however, is not uniform. Specifically, the simulated signal depressions and peaks corresponding to the positive bias (empty states) are quite similar to those obtained in experiment. Instead, the images obtained at the negative tip bias (occupied states) disagree both in terms of location of signal peaks and their symmetry.

5.2.2 Conclusions

Though the results of experiments and theoretical simulations do not agree in terms of the presence of in-gap states, they do provide an insight into electronic properties of Se vacancies in MoSe₂. The Se vacancy can be identified unambiguously via the three-fold symmetry

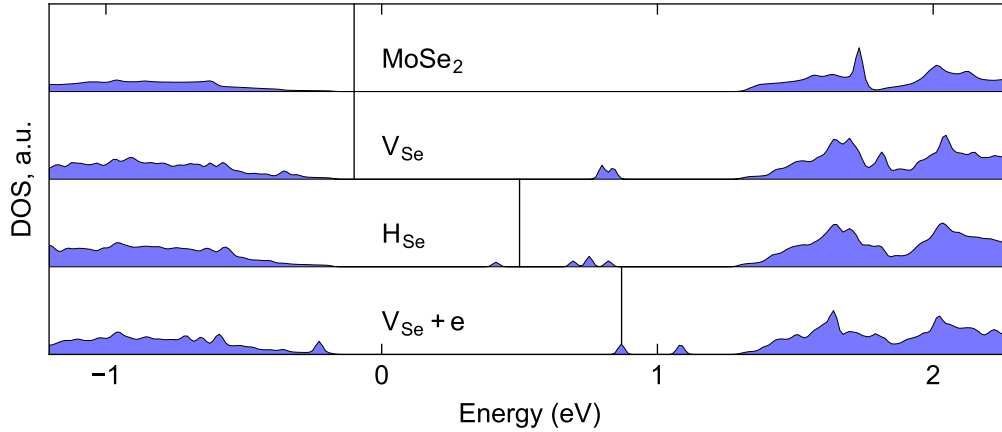


Figure 5.4 – Density of electronic states for the selenium vacancy defect in monolayer 2H-MoSe₂. The four plots correspond to pristine monolayer 2H-MoSe₂, the selenium vacancy model V_{Se}, the hydrogenated selenium vacancy H_{Se} and the negatively charged vacancy V_{Se} + e in a non-magnetic configuration. The Fermi level is indicated in each case.

preserved by the defect. The DFT predicts in-gap localized defect states regardless of defect kind and its charge state. However, no clue of localized in-gap states was observed in the experiment. One of the reasons for such behavior may be low tunneling rates between the defect state and bulk valence bands as explained in Ref. [106]: the charge carriers may prefer to tunnel directly into the bulk states while the charge carriers localized at the defect are, effectively, immobile. Further experiments as well as charge carrier tunneling simulations may provide additional understanding of the effect.

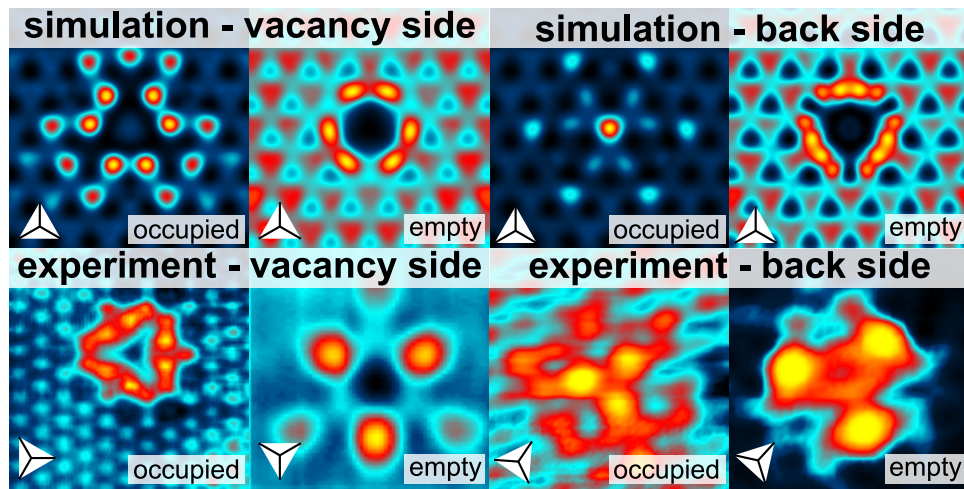


Figure 5.5 – Experimental and simulated STM images of the selenium vacancy in monolayer 2H-MoSe₂. Brighter colors correspond to larger signals.

6 Outlook

Though the 2D materials remain “hot” topic in a modern materials science, the attention to the first monolayer material, graphene, seems to saturate. From this perspective, the recently-discovered family of monolayer materials with a large enough band gap is a promising discovery with applications in the nanoscale electronics. The relatively short history of monolayer transition metal dichalcogenides (TMDs) partially resembles the one of graphene with a particular research focus on the most important properties for applications in electronics: structure, defects, transport properties. However, there are also structural, optical and spin phenomena which have not been observed in any other material making monolayer TMDs unique. Among such phenomena is the role of electron spin and the spin-orbit coupling in materials’ electronic and transport properties.

Each of the spin phenomena considered in the present study is related to a particular application, namely, the spin-valley coupling in monolayer 2H-TMDs provides a way to convert the charge carrier valley into its spin. The transport gap may be exploited in the engineering of a lateral semiconducting logic device where the domain boundaries either allow or prohibit charge carrier transport depending on symmetries of a line defect. The spin filtering of charge carriers is useful for spintronics: as demonstrated, the line defects in monolayer 2H-MoS₂ can be used to generate spin-polarized currents in a non-magnetic media by all-electric means. Thus, from the experimental perspective, it is of a primary importance to achieve high-quality material samples suitable for ballistic transport devices. On the theoretical side, the study of charge carrier scattering mechanisms in monolayer TMDs is required for a better understanding of the diffusive transport in these materials. In particular, the conservation laws being in the core of the phenomena studied (spin polarization of current, transport gap) have to be adjusted to the diffusive transport regime accessible experimentally. The methodological part could be extended towards a better description of ballistic transport properties in semiconducting materials. The existing density functional theory non-equilibrium Green’s function technique has to be extended towards a better description of transport properties of materials with a band gap. Specifically, the charge accumulation at the defect, the treatment of long-range electrostatic potentials and the incorrect band alignment of materials in contact

are known issues to overcome.

Another very popular topic in solid-state physics, the topology of electronic states, was also discussed in the thesis on the example of a metastable structural 1T' phase of monolayer TMDs. The electronic properties of the quantum spin Hall phase as well as the transport properties of phase boundaries presented are well in line with the experimental results. The study can be extended in several ways. First, the line defects presented are rather a “good guess” of what can be observed in experiment. Consecutively, a more complete study of possible line defects should be performed with a particular accent on the comparison with the future experiments. Second, the existence and the magnitude of the small band gap in monolayer 1T'-TMDs remains an open question. While a number of DFT, GW and hybrid functional studies of the monolayer 1T' phase are published, still no agreement is available. One of the possible sources of the disagreement was discussed in the thesis, namely, the sensitiveness of the band gap magnitude to the lattice constants. Further investigations, including the investigation of many-body effects in the electronic properties of monolayer 1T'-TMDs, are yet to be done.

A Appendix

A.1 On left and right eigenvalues

For a Hermitian matrix $\mathbf{H} = \mathbf{H}^\dagger$ the left and right eigenstates are simply connected via a Hermitian conjugation

$$\mathbf{H}\psi = E\psi \Rightarrow \psi^\dagger \mathbf{H} = \psi^\dagger E^* . \quad (\text{A.1})$$

This gives a well-known fact that a Hermitian matrix has real eigenvalues

$$E = \psi^\dagger E\psi = \psi^\dagger (\mathbf{H}\psi) = \psi^\dagger (\mathbf{H}\psi) = (\psi^\dagger \mathbf{H})\psi = \psi^\dagger E^* \psi = E^* . \quad (\text{A.2})$$

As a consequence of the above, the eigenvalues of left eigenstates E^* are the same as eigenvalues of right eigenstates E .

The above proof does not hold for non-Hermitian matrices $\mathbf{A} \neq \mathbf{A}^\dagger$. As a result, the left and right eigenstates of non-Hermitian matrices are different. Does this also mean that “left” and “right” eigenvalues are different as well? The answer is no, however, it is impossible to show it in a matrix-only way: a determinant property is used. Specifically,

$$\mathbf{A}\psi = \lambda\psi \Leftrightarrow (\mathbf{A} - \lambda)\psi = 0 \Leftrightarrow \det(\mathbf{A} - \lambda) = 0 . \quad (\text{A.3})$$

Left equation similarly leads to

$$\psi\mathbf{A} = \psi\lambda \Leftrightarrow \psi(\mathbf{A} - \lambda) = 0 \Leftrightarrow \det([\mathbf{A} - \lambda]^T) = 0 . \quad (\text{A.4})$$

The determinant of a matrix and the one of its transpose are exactly equivalent, thus, the above polynomial equations are exactly the same. Their roots are the same as well, thus, the sets of left eigenvalues and right eigenvalues are equal. Importantly, this holds for an arbitrary kind of an eigenvalue equations

$$\mathbf{F}(\lambda)\psi = 0, \quad \psi\mathbf{F}(\lambda) = 0 \quad (\text{A.5})$$

including generalized eigenvalue problem

$$\mathbf{A}\psi = \lambda\mathbf{B}\psi \Leftrightarrow \mathbf{F} = \lambda\mathbf{B} - \mathbf{A} \quad (\text{A.6})$$

and higher-order eigenvalue equations

$$\mathbf{A}\psi + \lambda\mathbf{B}\psi + \lambda^2\mathbf{C}\psi = 0 \Leftrightarrow \mathbf{F} = \mathbf{A} + \lambda\mathbf{B} + \lambda^2\mathbf{C} . \quad (\text{A.7})$$

For this reason there is no need in “left” and “right” eigenvalues: they are the same.

A.2 Valley filtering with line defects

In the original work[73] of Daniel Gunlycke and Carter White the valley-polarized charge carrier transport across a line defect in graphene was predicted. Since the idea of spin-polarized transport in TMDs is based on similar concepts I will briefly review the results of their study.

Consider a mirror-symmetric line defect in graphene such as the one in Fig A.1. How does the symmetry affect the eigenstates in this system? To answer this question the authors propose to split the entire lattice into two sublattices colored by blue and gray¹ in Fig. A.1. There are two possible ways to do it as illustrated on the left-hand side and on the right-hand side of the figure. Because of the mirror symmetry, however, these color schemes are equivalent. Thus, an operator cross-mapping the sublattices in graphene commutes with the single-particle Hamiltonian of the entire system. Such operator is presented by the Pauli matrix σ_x coupling sublattices A and B in the original study. For more complete description it is possible introduce the following operator

$$\mathbf{M} = \begin{bmatrix} \mathbf{0} & \mathbf{1} & \mathbf{0} \\ \mathbf{1} & \mathbf{0} & \mathbf{0} \\ \mathbf{0} & \mathbf{0} & \mathbf{1} \end{bmatrix} , \quad (\text{A.8})$$

where $\mathbf{M}_{1,2} = \mathbf{M}_{2,1} = \mathbf{1}$ cross-maps blue A and gray B sublattices and $\mathbf{M}_{3,3} = \mathbf{1}$ maps graphene atoms M in the middle (black in Fig. A.1) onto themselves. By above symmetry arguments, this operator commutes with the Hamiltonian. Thus, both can be diagonalized with the same set of eigenstates. There are two families of eigenstates of \mathbf{M} corresponding to eigenvalues $m = \pm 1$. They can be expressed as

$$\psi_{m=1} = c_1 (|A\rangle + |B\rangle) + c_2 |M\rangle , \quad \psi_{m=-1} = \frac{1}{\sqrt{2}} (|A\rangle - |B\rangle) , \quad (\text{A.9})$$

¹Note that the coloring is not mirror-symmetric

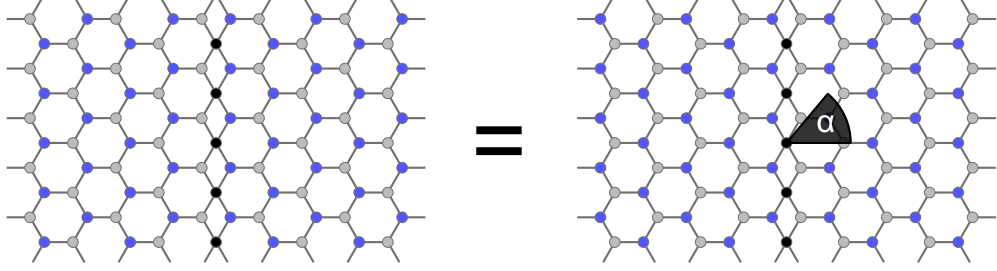


Figure A.1 – A mirror-symmetric line defect in graphene. The two graphene sublattices are colored by blue and gray colors. The right image is an equivalent mirror-symmetric version of the left image. The black atoms correspond to the symmetry line.

where $|A\rangle$, $|B\rangle$ and $|M\rangle$ are wavefunctions with non-zero amplitudes at the A , B and M sublattices respectively and c are complex numbers. The main feature of the second wavefunction in the above equation is that it has zero amplitudes on the M sites. In the nearest-neighbor tight binding limit, such states do not contribute to the transport because the transmission of charge carriers is impossible without hopping onto M sites. Thus, the focus is made on the wavefunctions of the first type which are symmetric with respect to sublattices A and B .

The second important step performed by the authors is to consider low-energy eigenstates in the bulk graphene located at K and K' valleys

$$|v, \theta\rangle = \frac{1}{\sqrt{2}} \left(|A\rangle + i e^{-i v \theta} |B\rangle \right), \quad (\text{A.10})$$

where $v = \pm 1$ is the valley index and θ refers to the direction of the group velocity of the charge carrier: it is the angle between the velocity vector and the armchair direction, see Fig. A.1. The defect-symmetric and the defect-antisymmetric parts of the above wavefunction are

$$|v, \theta\rangle = \frac{1 + i e^{-i v \theta}}{2} \frac{|A\rangle + |B\rangle}{\sqrt{2}} + \frac{1 - i e^{-i v \theta}}{2} \frac{|A\rangle - |B\rangle}{\sqrt{2}}. \quad (\text{A.11})$$

As it was noted above, the second part does not contribute to the transmission. The easiest way to understand it is to consider the limiting case $i e^{-i v \theta} = -1$ where only antisymmetric part survives. The amplitude of the scattering state at M sites vanishes exactly and there is no transmission across the defect. In the intermediate case $i e^{-i v \theta} \neq -1$ an upper estimate of the charge carrier transmission probability can be written as the amplitude of the first term in

Eq. A.11 squared². It is, essentially, the main result of Ref. [73]

$$T(v, \theta) < T_{\max} = \left| \frac{1 + ie^{-iv\theta}}{2} \right|^2 = \frac{1 + \sin v\theta}{2}. \quad (\text{A.12})$$

To emphasize the upper estimate the "<" sign is used: the transmission probability can be lower and, in principle, vanish completely in a rather artificial case where left and right parts of the system are spatially decoupled. Provided, however, a good transparency of the defect $T \approx T_{\max}$ it is possible to estimate the "valley polarization" of transmission as

$$P_v(\theta) = \frac{T(1, \theta) - T(-1, \theta)}{T(1, \theta) + T(-1, \theta)} = \sin \theta. \quad (\text{A.13})$$

The latter is symmetric about the origin $\theta = 0$. The ansatz is summarized with the following statement: the charge carriers originating from one of the valleys prefer to transmit in one of the directions while the charge carriers from the other valley prefer a mirror-symmetric direction.

Unfortunately, these results cannot be applied directly to line defects in 2D TMDs. The operator of mapping demonstrated in Fig. A.1 for graphene does not commute with the Hamiltonian of a mirror-symmetric line defect in a monolayer 2H-TMD (such as an inversion domain boundary) because the sublattices there are not equivalent. For example, in MoS₂, such mapping would swap Mo and S atoms producing a different kind of an inversion domain boundary. However, since MoS₂ and other TMDs have a lower symmetry compared to graphene there is no additional symmetry argument to constrain $P_v(\theta) \equiv 1$. Thus, one expects valley and spin polarization of charge carriers traveling across line defects in these materials.

A.3 Simulation details: charge carrier transport in monolayer 2H-MoS₂

The DFT simulations of ballistic charge carrier transport across line defects in MoS₂ have been performed in several steps:

1. Determine equilibrium atomic and electronic structures of the bulk. This step was done using the Quantum ESPRESSO distribution[107] with ultrasoft pseudopotentials from Ref. [49]. Other most important parameters of calculations are following:

²Because $\frac{|A\rangle+|B\rangle}{\sqrt{2}}$ and $\frac{|A\rangle-|B\rangle}{\sqrt{2}}$ form an orthonormal basis.

A.4. Simulation details: spin polarization of the transmission probability in monolayer 2H-MoS₂

wavefunction cutoff	80 Ry
density cutoff	1000 Ry
k grid	18x18
energy convergence criterion	10 ⁻⁶ Ry
force convergence criterion	10 ⁻⁵ $\frac{\text{Ry}}{a_{\text{Bohr}}}$
pressure convergence criterion	1 bar
size of the unit cell in the vacuum direction	2 nm

2. Determine the equilibrium atomic structure of the defect. The structural optimization calculations were done in supercell configurations where the line defects were separated by at least 1.5 nm in the transport direction, see the atomic structure presentid in Fig. 2.7 for an example.
3. Determine transport properties using NEGF technique. The last step was performed using the OpenMX code[108]. The size of the unit cell in the vacuum direction was increased to 10 nm for the correct description of electrostatic effects. The localized basis set Mo:s2p2d2f1 S:s2p3d1 was found to correctly reproduce the bulk band structure obtained previously. The scattering regions where deviations from the bulk charge density and potential are allowed were 3-5 nm large along the transport direction. The electrostatic potential obtained in the Dirichlet boundary conditions was used to obtain transport properties including transmission. The leads' bulk states were perfectly aligned in energy: the voltage bias was assumed to be zero.

A.4 Simulation details: spin polarization of the transmission probability in monolayer 2H-MoS₂

In 2D systems with a 1D defect, the total transmission function value T defined by the Caroli expression, Eq. 2.75, is a function of the pseudomomentum projection $k_{||}$. In Lanauer-Buttiker formula, Eq. 2.29, this dependence was omitted. To include it, one typically assumes the contacts to be much larger than the size of the device and takes the transmission function average

$$T(E) = \int_{k_{||}=-0.5}^{0.5} dk_{||} T(E, k_{||}) , \quad (\text{A.14})$$

where $k_{||}$ is a coordinate in the BZ expressed in reciprocal lattice units.

However, to be able to generate spin-polarized currents using line defects in MoS₂ one has to break the $k_{||} - (-k_{||})$ symmetry because otherwise

$$P_{\sigma}(E) = \int_{k_{||}=-0.5}^{0.5} dk_{||} P_{\sigma}(E, k_{||}) = 0 , \quad (\text{A.15})$$

Appendix A. Appendix

where $P_\sigma(E, k_{||})$ is defined in Eq. 3.5. This is done by considering an opposite limiting case where contacts' size is much smaller than the distance between them. This allows to force the ballistic current to propagate along some well-defined direction θ within small angle $d\theta$. The corresponding Lanauer-Buttiker formula is

$$dI = d\theta \cdot \frac{e}{h} \int dE \cdot \tau(E, \theta) f'(E) , \quad (\text{A.16})$$

where the angle θ is calculated for a given lead mode

$$\theta = \arctan \frac{v_{||}}{v_{tr}} = \arctan \frac{\partial E / \partial k_{||}}{\partial E / \partial k_{tr}} , \quad (\text{A.17})$$

where $E(\vec{k})$ is a dispersion of the energy band the state belongs to and k_{tr} is a projection of the pseudomomentum along the transport direction. The τ function resembles the total transmission for a given angle θ . For consistency, after integrating Eq. A.16 the original current value should be recovered

$$I = \frac{e}{h} \int d\theta \int dE \cdot \tau(E, \theta) f'(E) . \quad (\text{A.18})$$

The above expression is very similar to the original Eq. 2.29 with Eq. A.14 substituted

$$I = \frac{e}{h} \int dk_{||} \int dE \cdot T(E, k_{||}) f'(E) . \quad (\text{A.19})$$

Thus, it should be possible to define τ by corresponding the above two equations using the Dirac δ -function. The problem, however, is that neither map $k_{||} \rightarrow \theta$ nor $\theta \rightarrow k_{||}$ exist as a function. Thus, one has to split integration into branches shown as colored arcs in Fig. A.2. Within each branch, the bulk states can be parametrized by both $k_{||}$ and, more importantly, θ . Eqs. A.18, A.19 can be written as

$$I = \frac{e}{h} \int dE f'(E) \sum_{b \in \{\text{branches}\}} \int_{\theta=\theta_b^{\min}}^{\theta_b^{\max}} d\theta \cdot \tau_b(E, \theta) \quad (\text{A.20})$$

and

$$I = \frac{e}{h} \int dE f'(E) \sum_{b \in \{\text{branches}\}} \int_{k_{||}=k_b^{\min}}^{k_b^{\max}} dk_{||} \cdot T_b(E, k_{||}) . \quad (\text{A.21})$$

The above equations are satisfied, for example, if

$$\tau_b(E, \theta) = \frac{\partial k_{||}(\theta)}{\partial \theta} T_b(E, k_{||}(\theta)) . \quad (\text{A.22})$$

By taking the sum over specific branches, see Fig. A.2(c), the angle-dependent transmission is

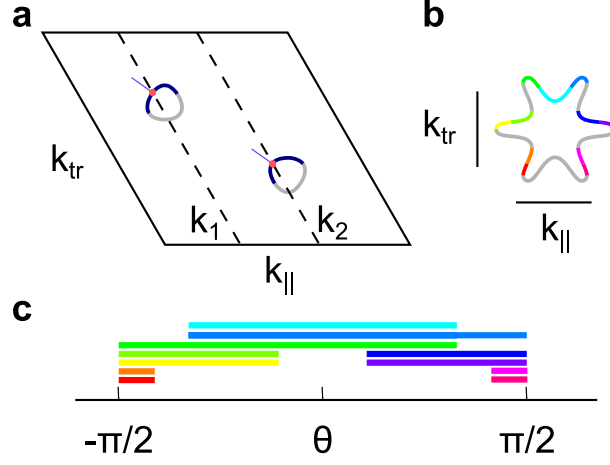


Figure A.2 – An illustration of Fermi surfaces, branches and bulk states used in the calculation of angle-dependent properties. (a) Valence states of monolayer 2H-MoS₂ participating in transport close to the top of the valence bands. The blue arcs correspond to branches of outgoing modes in the drain lead while the gray arcs correspond to incoming modes. The two modes corresponding to different branches with same group velocity direction (light blue arrows) are indicated by red dots. The corresponding pseudomomentum projections of states $k_{1,2}$ are indicated. (b) A more complex case of a Fermi surface having a hexagonal symmetry. There, a single band produces 11 branches with outgoing states marked with color. The gray color corresponds to incoming states. (c) A schematic illustration of angles covered by each branch in (b). Depending on θ , three or five branches out of 11 contribute to angle-dependent properties.

defined

$$\tau(E, \theta) = \sum_{b \in \{\text{branches}(\theta)\}} \frac{\partial k_{||}(\theta)}{\partial \theta} T_b(E, k_{||}(\theta)) . \quad (\text{A.23})$$

For the simplicity of description, however, an assumption $\frac{\partial k_{||}(\theta)}{\partial \theta} = 1$ has been made for Eq. 3.5 as well as the results presented in Fig. 3.7. The resulting workflow for determining the angle-dependent spin polarization is

1. Determine the transmission probabilities $t_{n \rightarrow m}(E, k_{||})$ on a $k_{||} - E$ grid using Eq. 2.81;
2. Sum transmission probabilities belonging to the same outgoing mode $t_m(E, k_{||}) = \sum_n t_{n \rightarrow m}(E, k_{||})$;
3. Determine $\theta_m(E, k_{||})$ for each outgoing mode using Eq. A.17;
4. Determine branches $b_m(E, k_{||})$ based on such criteria as:
 - overlap of lead modes belonging to neighboring $k_{||}$;
 - closeness of k_{tr} for modes with neighboring $k_{||}$;

- smoothness and extreme points of function $\theta(k_{||})$;

This step requires a heuristic analysis on a fine enough grid of $k_{||}$;

5. Combine above quantities into $\theta_b(E, k_{||})$ and $t_b(E, \theta)$. The latter should be interpolated on a grid of values of θ within an interval $[\theta_b^{\min}, \theta_b^{\max}]$. The quantities $\theta_b^{\min, \max}$ are either extreme points of $\theta(k_{||})$ or equal to $\pm\pi/2$;
6. Calculate $\frac{\partial k_{||}(\theta)}{\partial \theta}$ by inverting function $\theta_b(E, k_{||})$ or assume the former to be equal to one;
7. Calculate the total transmission using Eq. A.23 as well as the spin transmission using a modified expression

$$\tau_{\sigma}(E, \theta) = \sum_{b \in \{\text{branches}(\theta)\}} \frac{\partial k_{||}(\theta)}{\partial \theta} T_b(E, k_{||}(\theta)) \cdot \sigma_b(E, k_{||}(\theta)) . \quad (\text{A.24})$$

8. Calculate $P_{\sigma}(E, \theta) = \tau_{\sigma}(E, \theta) / \tau(E, \theta)$.

A.5 Projected³ band structure in monolayer 2H-MoS₂ and other 2D materials

To understand the charge carrier transmission across a periodic line defect one has to consider the interplay between bulk states of the leads. This is done by projecting the bulk band structure onto a 1D Brillouin zone of a line defect. In other words one has to map the 2D BZ $\vec{K} = (k_x, k_y)$ to the 1D BZ $k_{||}$. This is closely related to the “folding”⁴ of the band structure. A brief mathematical introduction is given further.

Consider a (crystal) basis \mathbf{A} such that the Cartesian coordinates \vec{R} are related to the crystal coordinates \vec{r} via the following matrix-vector product

$$\vec{R} = \mathbf{A} \vec{r} . \quad (\text{A.25})$$

The matrix \mathbf{A} has unit vectors of a crystal as its columns. Similarly, the corresponding reciprocal basis \mathbf{B} having reciprocal unit vectors as its columns connects Cartesian coordinates of a wave vector \vec{K} and its reciprocal crystal coordinates \vec{k}

$$\vec{K} = \mathbf{B} \vec{k} . \quad (\text{A.26})$$

The defining relation between the real and the reciprocal bases is the inverse-transpose operation (an optional 2π factor is omitted)

$$\mathbf{B} = (\mathbf{A}^{-1})^T . \quad (\text{A.27})$$

³Not to confuse with orbital-projected band structure

⁴The term “folding” rather means producing shifted replicas in the context of the discussion

Though the basis \mathbf{A} contains unit vectors it is possible to define another basis \mathbf{A}' to, for example, describe a supercell. The general relation between the basis and its alternate version is the matrix product

$$\mathbf{A}' = \mathbf{A}\mathbf{N}, \quad (\text{A.28})$$

where the square matrix \mathbf{N} contains integers similar to Eq. 2.6. The new basis \mathbf{A}' may describe a unit cell or a supercell, depending on available symmetries and values in \mathbf{N} . In either case its reciprocal counterpart is described by the matrix

$$\mathbf{B}' = \left(\mathbf{A}'^{-1}\right)^T. \quad (\text{A.29})$$

Provided \mathbf{A}' is a supercell basis, the electronic band structure of a material gets “folded” such that multiple points in the original BZ are projected onto the same point in the new BZ. Lets find the mapping. Consider $\vec{K} = (k_x, k_y)$ having the same reciprocal Cartesian coordinates in both basis sets

$$\vec{K} = \mathbf{B}\vec{k} = \mathbf{B}'\vec{k}'. \quad (\text{A.30})$$

The new reciprocal lattice coordinates \vec{k}' are simply

$$\vec{k}' = (\mathbf{B}')^{-1} \mathbf{B}\vec{k} = \mathbf{A}'^T \mathbf{B}\vec{k} = \mathbf{N}^T \mathbf{A}^T \mathbf{B}\vec{k} = \mathbf{N}^T \vec{k}. \quad (\text{A.31})$$

As a relevant example, consider the hexagonal lattice of monolayer 2H-TMDs. The lattice unit cell can be defined as

$$\mathbf{A} = (\vec{a}_1, \vec{a}_2) = \begin{bmatrix} a & a/2 \\ 0 & \frac{\sqrt{3}}{2}a \end{bmatrix}. \quad (\text{A.32})$$

The reciprocal unit cell demonstrated in Fig. 3.1(c) is

$$\mathbf{B} = (\mathbf{A}^{-1})^T = \begin{bmatrix} 1/a & 0 \\ -1/\sqrt{3}a & 2/\sqrt{3}a \end{bmatrix}. \quad (\text{A.33})$$

It is easy to identify the crystal coordinates of points K and K' to be

$$k(K) = \begin{bmatrix} 1/3 \\ 2/3 \end{bmatrix}, \quad k(K') = \begin{bmatrix} 2/3 \\ 1/3 \end{bmatrix}. \quad (\text{A.34})$$

The 1D Brillouin zone of a defect can be obtained in the limit when one of the supercell vectors approaches infinity. It can be written symbolically for the left lead as

$$\mathbf{A}' = \mathbf{A}\mathbf{N} = \mathbf{A} \begin{bmatrix} n_L & \infty \\ m_L & \infty \end{bmatrix}, \quad (\text{A.35})$$

where n_L, m_L are integer coordinates of the defect periodicity vector defined in Eq. 3.1. Using Eq. A.31 it is deduced that

$$\vec{k}'(\mathbf{K}) = \begin{bmatrix} k_{||}(\mathbf{K}) \\ \cdot \end{bmatrix} = \begin{bmatrix} n_L & m_L \\ \infty & \infty \end{bmatrix} \begin{bmatrix} 1/3 \\ 2/3 \end{bmatrix} = \begin{bmatrix} \frac{n_L+2m_L}{3} \\ \cdot \end{bmatrix}. \quad (\text{A.36})$$

Since the reciprocal lattice is periodic the reciprocal crystal coordinates are defined up to an arbitrary integer i

$$\{k_{||}(\mathbf{K})\} = \left\{ \frac{n_L+2m_L}{3} + i, i \in \mathbf{Z} \right\} = \left\{ \frac{(n_L-m_L) \bmod 3}{3} + i, i \in \mathbf{Z} \right\}. \quad (\text{A.37})$$

Similarly,

$$\{k_{||}(\mathbf{K}')\} = \left\{ \frac{(m_L-n_L) \bmod 3}{3} + i, i \in \mathbf{Z} \right\} = \{-k_{||}(\mathbf{K})\}. \quad (\text{A.38})$$

Above equation results in Eq. 3.2 up to a factor π .

Finally, the size of the transport gap is simply deduced by looking at Fig. 3.6. Under the first approximation, the quasi-free hole charge carriers at \mathbf{K} and \mathbf{K}' exhibit the following dispersion law

$$E = -\frac{\hbar^2 |\delta k|^2}{2m^*}, \quad (\text{A.39})$$

where m^* is the positive effective mass and δk is a small distance to \mathbf{K} or \mathbf{K}' in the reciprocal space. The spin-conserving channels are released either at the edges of a 1D BZ (if neither \mathbf{K}, \mathbf{K}' point is projected onto $k_{||} = 0$) or at $k_{||} = \frac{2\pi}{6d}$ (if one of the leads has its \mathbf{K}, \mathbf{K}' points projected onto $k_{||} = 0$). In either case the corresponding $\delta k = \frac{2\pi}{6d}$ which immediately yields expression in Eq. 3.4.

A.6 Simulation details: periodic zigzag terminations of monolayer 1T'-TMDs

The structures of zigzag terminations were obtained by relaxing inversion-symmetric zigzag nanoribbons of various widths up to 7 nm using the Quantum ESPRESSO distribution[107] with non-relativistic ultrasoft pseudopotentials from Ref. [49]. The nanoribbon images were decoupled by, at least, 1 nm in the material plane and by 2 nm away from it. Other most important parameters of simulations are following:

wavefunction cutoff	65 Ry
density cutoff	1000 Ry
k points	12
energy convergence criterion	10^{-6} Ry
force convergence criterion	$10^{-3} \frac{\text{Ry}}{a_{\text{Bohr}}}$ (default)

A.7. Local densities of states at the zigzag terminations of monolayer 1T'-TMDs

To calculate local densities of states presented in Fig.4.9 the nanoribbon Hamiltonian was expressed in the localized basis set by means of the OpenMX code[108]. Afterwards, one of the equivalent nanoribbon edges was replaced by a semi-infinite bulk material. The resulting structure was used to obtain the local density of states of the edge using the NEGF technique.

A.7 Local densities of states at the zigzag terminations of monolayer 1T'-TMDs

The local densities of electronic states of all zigzag terminations are presented in Fig. A.3.

A.8 Simulation details: Fe adatoms on the surface of Bi₂Te₃

The models of Fe adatoms on the surface of Bi₂Te₃ were relaxed in 2x2 supercells of Bi₂Te₃ slabs using the Quantum ESPRESSO distribution[107]. The slab contained 3 quintuple layers of Bi₂Te₃ resulting in 60 atoms per supercell plus one Fe adatom. Other most important parameters of simulations are the following

wavefunction cutoff	50 Ry
density cutoff	300 Ry
k grid	2x2
energy convergence criterion	10^{-4} Ry (default)
force convergence criterion	$10^{-3} \frac{\text{Ry}}{a_{\text{Bohr}}}$ (default)
size of the unit cell in the vacuum direction	2.5 nm
Hubbard U	3 eV

The nudged elastic band calculations were carried out with five images (one “climbing” image[109]).

A.9 Simulation details: point defects in MoSe₂

The models of point defects were relaxed in 5x5 supercells of monolayer 2H-MoSe₂ using the Quantum ESPRESSO distribution[107] with nonrelativistic ultrasoft pseudopotentials from Ref. [49]. The most important parameters of the simulations are the following

wavefunction cutoff	65 Ry
density cutoff	1000 Ry
k grid	3x3
energy convergence criterion	10^{-6} Ry
force convergence criterion	$10^{-3} \frac{\text{Ry}}{a_{\text{Bohr}}}$ (default)
size of the unit cell in the vacuum direction	2 nm

The simulated STM images presented in Fig. 5.3 were obtained by integrating the local

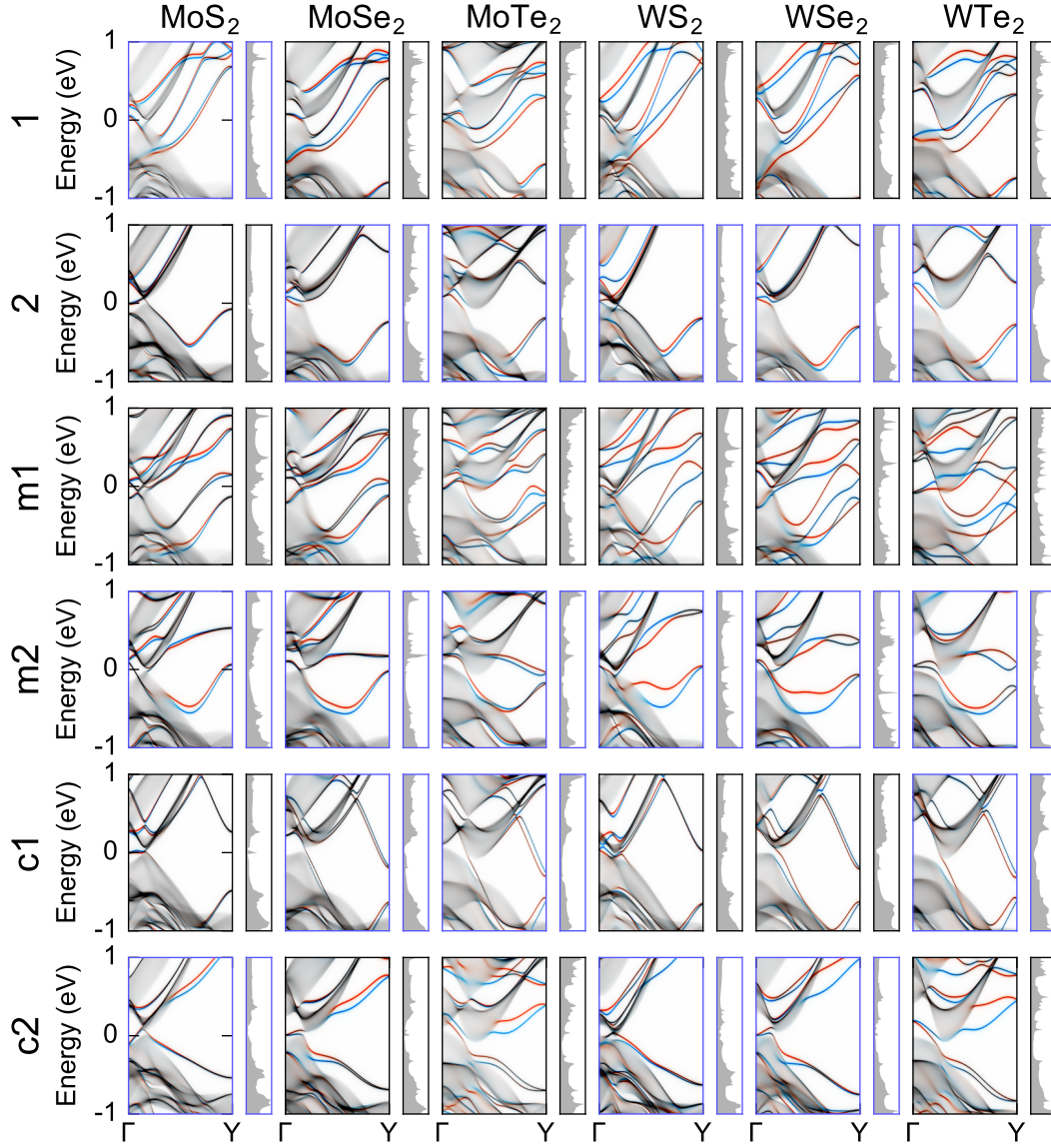


Figure A.3 – The local density of states of the six zigzag terminations presented in Fig. 4.8. The blue and red colors on each plot represent the contribution of the out-of-plane spin-up and spin-down polarized states to the total weight. Those plots already presented in Fig. 4.9 are marked by blue frames. Side plots present the density of states integrated over k .

(coordinate-dependent) density of states (LDOS) from the Fermi level to the two different values corresponding to 100 meV below the top of valence bands and 100 meV above the bottom of conduction bands. The images plotted correspond to the value of LDOS 1.5 Å above topmost atom in the corresponding atomic structure.

The densities of electronic states were obtained from band structure calculations on a fine 50x50 k -point grid using the OpenMX code[108] with the relaxed atomic coordinates.

Bibliography

- [1] Products (Formerly Skylake), 2016.
- [2] S. Lebègue and O. Eriksson. Electronic structure of two-dimensional crystals from \textit{ab initio} theory. *Physical Review B*, 79(11):115409, March 2009.
- [3] Ken Shirriff. Reverse-engineering the TL431: the most common chip you’ve never heard of, 2014.
- [4] J. Bardeen and W. H. Brattain. The Transistor, A Semi-Conductor Triode. *Physical Review*, 74(2):230–231, July 1948.
- [5] Eugen Merzbacher. *Quantum Mechanics*. Wiley, 3 edition, January 1998.
- [6] Paul Benioff. The computer as a physical system: A microscopic quantum mechanical Hamiltonian model of computers as represented by Turing machines. *Journal of Statistical Physics*, 22(5):563–591, May 1980.
- [7] P. Shor. Polynomial-Time Algorithms for Prime Factorization and Discrete Logarithms on a Quantum Computer. *SIAM Journal on Computing*, 26(5):1484–1509, October 1997.
- [8] Han Wang, Lili Yu, Yi-Hsien Lee, Yumeng Shi, Allen Hsu, Matthew L. Chin, Lain-Jong Li, Madan Dubey, Jing Kong, and Tomas Palacios. Integrated Circuits Based on Bilayer MoS2 Transistors. *Nano Letters*, 12(9):4674–4680, September 2012.
- [9] K. S. Novoselov, D. Jiang, F. Schedin, T. J. Booth, V. V. Khotkevich, S. V. Morozov, and A. K. Geim. Two-dimensional atomic crystals. *Proceedings of the National Academy of Sciences of the United States of America*, 102(30):10451–10453, July 2005.
- [10] K. S. Novoselov, A. K. Geim, S. V. Morozov, D. Jiang, Y. Zhang, S. V. Dubonos, I. V. Grigorieva, and A. A. Firsov. Electric Field Effect in Atomically Thin Carbon Films. *Science*, 306(5696):666–669, October 2004.
- [11] A. H. Castro Neto, F. Guinea, N. M. R. Peres, K. S. Novoselov, and A. K. Geim. The electronic properties of graphene. *Reviews of Modern Physics*, 81(1):109–162, January 2009.

Bibliography

- [12] Andrea Splendiani, Liang Sun, Yuanbo Zhang, Tianshu Li, Jonghwan Kim, Chi-Yung Chim, Giulia Galli, and Feng Wang. Emerging Photoluminescence in Monolayer MoS₂. *Nano Letters*, 10(4):1271–1275, 2010.
- [13] Kin Fai Mak, Changgu Lee, James Hone, Jie Shan, and Tony F. Heinz. Atomically Thin MoS₂: A New Direct-Gap Semiconductor. *Physical Review Letters*, 105(13):136805, September 2010.
- [14] Branimir Radisavljevic, Michael Brian Whitwick, and Andras Kis. Integrated Circuits and Logic Operations Based on Single-Layer MoS₂. *ACS Nano*, 5(12):9934–9938, December 2011.
- [15] B. Radisavljevic, A. Radenovic, J. Brivio, V. Giacometti, and A. Kis. Single-layer MoS₂ transistors. *Nature Nanotechnology*, 6(3):147–150, March 2011.
- [16] Di Xiao, Gui-Bin Liu, Wanxiang Feng, Xiaodong Xu, and Wang Yao. Coupled Spin and Valley Physics in Monolayers of MoS₂ and Other Group-VI Dichalcogenides. *Physical Review Letters*, 108(19):196802, May 2012.
- [17] Hualing Zeng, Junfeng Dai, Wang Yao, Di Xiao, and Xiaodong Cui. Valley polarization in MoS₂ monolayers by optical pumping. *Nature Nanotechnology*, 7(8):490–493, August 2012.
- [18] Kin Fai Mak, Keliang He, Jie Shan, and Tony F. Heinz. Control of valley polarization in monolayer MoS₂ by optical helicity. *Nature Nanotechnology*, 7(8):494–498, August 2012.
- [19] Ting Cao, Gang Wang, Wenpeng Han, Huiqi Ye, Chuanrui Zhu, Junren Shi, Qian Niu, Pingheng Tan, Enge Wang, Baoli Liu, and Ji Feng. Valley-selective circular dichroism of monolayer molybdenum disulphide. *Nature Communications*, 3:887, June 2012.
- [20] Zhaoqiang Zheng, Tanmei Zhang, Jiandong Yao, Yi Zhang, Jiarui Xu, and Guowei Yang. Flexible, transparent and ultra-broadband photodetector based on large-area WSe₂ film for wearable devices. *Nanotechnology*, 27(22):225501, 2016.
- [21] Li Tao, Eugenio Cinquanta, Daniele Chiappe, Carlo Grazianetti, Marco Fanciulli, Madan Dubey, Alessandro Molle, and Deji Akinwande. Silicene field-effect transistors operating at room temperature. *Nature Nanotechnology*, 10(3):227–231, March 2015.
- [22] Pere Miró, Martha Audiffred, and Thomas Heine. An atlas of two-dimensional materials. *Chemical Society Reviews*, 43(18):6537, May 2014.
- [23] C. L. Kane and E. J. Mele. \mathbb{Z}_2 Topological Order and the Quantum Spin Hall Effect. *Physical Review Letters*, 95(14):146802, September 2005.
- [24] B. Andrei Bernevig, Taylor L. Hughes, and Shou-Cheng Zhang. Quantum Spin Hall Effect and Topological Phase Transition in HgTe Quantum Wells. *Science*, 314(5806):1757–1761, December 2006.

-
- [25] B. Andrei Bernevig and Shou-Cheng Zhang. Quantum Spin Hall Effect. *Physical Review Letters*, 96(10):106802, March 2006.
 - [26] Markus König, Steffen Wiedmann, Christoph Brüne, Andreas Roth, Hartmut Buhmann, Laurens W. Molenkamp, Xiao-Liang Qi, and Shou-Cheng Zhang. Quantum Spin Hall Insulator State in HgTe Quantum Wells. *Science*, 318(5851):766–770, November 2007.
 - [27] Liang Fu and C. L. Kane. Topological insulators with inversion symmetry. *Physical Review B*, 76(4):045302, July 2007.
 - [28] Joel Moore. Topological insulators: The next generation. *Nature Physics*, 5(6):378–380, June 2009.
 - [29] M. Z. Hasan and C. L. Kane. Colloquium : Topological insulators. *Reviews of Modern Physics*, 82(4):3045–3067, November 2010.
 - [30] Xiao-Liang Qi and Shou-Cheng Zhang. Topological insulators and superconductors. *Reviews of Modern Physics*, 83(4):1057–1110, October 2011.
 - [31] Alexei Kitaev. Periodic table for topological insulators and superconductors. In *AIP Conference Proceedings*, volume 1134, pages 22–30. AIP Publishing, May 2009.
 - [32] Y. L. Chen, J. G. Analytis, J.-H. Chu, Z. K. Liu, S.-K. Mo, X. L. Qi, H. J. Zhang, D. H. Lu, X. Dai, Z. Fang, S. C. Zhang, I. R. Fisher, Z. Hussain, and Z.-X. Shen. Experimental Realization of a Three-Dimensional Topological Insulator, Bi₂Te₃. *Science*, 325(5937):178–181, July 2009.
 - [33] Y. Xia, D. Qian, D. Hsieh, L. Wray, A. Pal, H. Lin, A. Bansil, D. Grauer, Y. S. Hor, R. J. Cava, and M. Z. Hasan. Observation of a large-gap topological-insulator class with a single Dirac cone on the surface. *Nature Physics*, 5(6):398–402, June 2009.
 - [34] Haijun Zhang, Chao-Xing Liu, Xiao-Liang Qi, Xi Dai, Zhong Fang, and Shou-Cheng Zhang. Topological insulators in Bi₂Se₃, Bi₂Te₃ and Sb₂Te₃ with a single Dirac cone on the surface. *Nature Physics*, 5(6):438–442, 2009.
 - [35] Y. L. Chen, J.-H. Chu, J. G. Analytis, Z. K. Liu, K. Igarashi, H.-H. Kuo, X. L. Qi, S. K. Mo, R. G. Moore, D. H. Lu, M. Hashimoto, T. Sasagawa, S. C. Zhang, I. R. Fisher, Z. Hussain, and Z. X. Shen. Massive Dirac Fermion on the Surface of a Magnetically Doped Topological Insulator. *Science*, 329(5992):659–662, August 2010.
 - [36] James G. Analytis, Jiun-Haw Chu, Yulin Chen, Felipe Corredor, Ross D. McDonald, Z. X. Shen, and Ian R. Fisher. Bulk Fermi surface coexistence with Dirac surface state in Bi₂Se₃: A comparison of photoemission and Shubnikov-de Haas measurements. *Physical Review B*, 81(20):205407, May 2010.
 - [37] L. Andrew Wray, Su-Yang Xu, Yuqi Xia, David Hsieh, Alexei V. Fedorov, Yew San Hor, Robert J. Cava, Arun Bansil, Hsin Lin, and M. Zahid Hasan. A topological insulator

- surface under strong Coulomb, magnetic and disorder perturbations. *Nature Physics*, 7(1):32–37, January 2011.
- [38] Oleg V. Yazyev, Joel E. Moore, and Steven G. Louie. Spin Polarization and Transport of Surface States in the Topological Insulators Bi_2Se_3 and Bi_2Te_3 from First Principles. *Physical Review Letters*, 105(26):266806, December 2010.
- [39] S. B. Zhang and John E. Northrup. Chemical potential dependence of defect formation energies in GaAs: Application to Ga self-diffusion. *Physical Review Letters*, 67(17):2339–2342, October 1991.
- [40] Wu Zhou, Xiaolong Zou, Sina Najmaei, Zheng Liu, Yumeng Shi, Jing Kong, Jun Lou, Pulickel M. Ajayan, Boris I. Yakobson, and Juan-Carlos Idrobo. Intrinsic Structural Defects in Monolayer Molybdenum Disulfide. *Nano Letters*, 13(6):2615–2622, June 2013.
- [41] Sina Najmaei, Zheng Liu, Wu Zhou, Xiaolong Zou, Gang Shi, Sidong Lei, Boris I. Yakobson, Juan-Carlos Idrobo, Pulickel M. Ajayan, and Jun Lou. Vapour phase growth and grain boundary structure of molybdenum disulphide atomic layers. *Nature Materials*, 12(8):754–759, August 2013.
- [42] F. Schedin, A. K. Geim, S. V. Morozov, E. W. Hill, P. Blake, M. I. Katsnelson, and K. S. Novoselov. Detection of individual gas molecules adsorbed on graphene. *Nature Materials*, 6(9):652–655, September 2007.
- [43] Jesse D. Fowler, Matthew J. Allen, Vincent C. Tung, Yang Yang, Richard B. Kaner, and Bruce H. Weiller. Practical Chemical Sensors from Chemically Derived Graphene. *ACS Nano*, 3(2):301–306, February 2009.
- [44] K. S. Novoselov, Z. Jiang, Y. Zhang, S. V. Morozov, H. L. Stormer, U. Zeitler, J. C. Maan, G. S. Boebinger, P. Kim, and A. K. Geim. Room-Temperature Quantum Hall Effect in Graphene. *Science*, 315(5817):1379–1379, March 2007.
- [45] P. Hohenberg and W. Kohn. Inhomogeneous Electron Gas. *Physical Review*, 136(3B):B864–B871, November 1964.
- [46] W. Kohn and L. J. Sham. Self-Consistent Equations Including Exchange and Correlation Effects. *Physical Review*, 140(4A):A1133–A1138, 1965.
- [47] David C. Langreth and M. J. Mehl. Beyond the local-density approximation in calculations of ground-state electronic properties. *Physical Review B*, 28(4):1809–1834, August 1983.
- [48] Gábor I. Csonka, John P. Perdew, Adrienn Ruzsinszky, Pier H. T. Philipsen, Sébastien Lebègue, Joachim Paier, Oleg A. Vydrov, and János G. Ángyán. Assessing the performance of recent density functionals for bulk solids. *Physical Review B*, 79(15):155107, April 2009.

- [49] Kurt Lejaeghere, Gustav Bihlmayer, Torbjörn Björkman, Peter Blaha, Stefan Blügel, Volker Blum, Damien Caliste, Ivano E. Castelli, Stewart J. Clark, Andrea Dal Corso, Stefano de Gironcoli, Thierry Deutsch, John Kay Dewhurst, Igor Di Marco, Claudia Draxl, Marcin Dułak, Olle Eriksson, José A. Flores-Livas, Kevin F. Garrity, Luigi Genovese, Paolo Giannozzi, Matteo Giantomassi, Stefan Goedecker, Xavier Gonze, Oscar Grånäs, E. K. U. Gross, Andris Gulans, François Gygi, D. R. Hamann, Phil J. Hasnip, N. a. W. Holzwarth, Diana Iușan, Dominik B. Jochym, François Jollet, Daniel Jones, Georg Kresse, Klaus Koepernik, Emine Küçükbenli, Yaroslav O. Kvashnin, Inka L. M. Locht, Sven Lubeck, Martijn Marsman, Nicola Marzari, Ulrike Nitzsche, Lars Nordström, Taisuke Ozaki, Lorenzo Paulatto, Chris J. Pickard, Ward Poelmans, Matt I. J. Probert, Keith Refson, Manuel Richter, Gian-Marco Rignanese, Santanu Saha, Matthias Scheffler, Martin Schlipf, Karlheinz Schwarz, Sangeeta Sharma, Francesca Tavazza, Patrik Thunström, Alexandre Tkatchenko, Marc Torrent, David Vanderbilt, Michiel J. van Setten, Veronique Van Speybroeck, John M. Wills, Jonathan R. Yates, Guo-Xu Zhang, and Stefaan Cottenier. Reproducibility in density functional theory calculations of solids. *Science*, 351(6280):aad3000, March 2016.
- [50] Kurt Stokbro, Jeremy Taylor, Mads Brandbyge, and Pablo Ordejón. TranSIESTA: a spice for molecular electronics. *Annals of the New York Academy of Sciences*, 1006:212–226, December 2003.
- [51] Ivan Rungger and Stefano Sanvito. Algorithm for the construction of self-energies for electronic transport calculations based on singularity elimination and singular value decomposition. *Physical Review B*, 78(3):035407, July 2008.
- [52] Taisuke Ozaki, Kengo Nishio, and Hiori Kino. Efficient implementation of the nonequilibrium Green function method for electronic transport calculations. *Physical Review B*, 81(3):035116, January 2010.
- [53] P. A. Khomyakov, G. Brocks, V. Karpan, M. Zwierzycki, and P. J. Kelly. Conductance calculations for quantum wires and interfaces: Mode matching and Green’s functions. *Physical Review B*, 72(3):035450, July 2005.
- [54] LAPACK — Linear Algebra PACKage.
- [55] Luca Molinari. Transfer matrices and tridiagonal-block Hamiltonians with periodic and scattering boundary conditions. *Journal of Physics A: Mathematical and General*, 30(3):983, 1997.
- [56] C. Caroli, R. Combescot, P. Nozieres, and D. Saint-James. Direct calculation of the tunneling current. *Journal of Physics C: Solid State Physics*, 4(8):916, 1971.
- [57] C. Caroli, R. Combescot, P. Nozieres, and D. Saint-James. A direct calculation of the tunnelling current: IV. Electron-phonon interaction effects. *Journal of Physics C: Solid State Physics*, 5(1):21, 1972.

Bibliography

- [58] M. P. Lopez Sancho, J. M. Lopez Sancho, and J. Rubio. Quick iterative scheme for the calculation of transfer matrices: application to Mo (100). *Journal of Physics F: Metal Physics*, 14(5):1205, 1984.
- [59] M. P. Lopez Sancho, J. M. Lopez Sancho, and J. Rubio. A nonorthogonal-basis calculation of the spectral density of surface states for the (100) and (110) faces of tungsten. *Journal of Physics C: Solid State Physics*, 18(9):1803, 1985.
- [60] Nicola Marzari and David Vanderbilt. Maximally localized generalized Wannier functions for composite energy bands. *Physical Review B*, 56(20):12847–12865, November 1997.
- [61] J. Tersoff and D. R. Hamann. Theory of the scanning tunneling microscope. *Physical Review B*, 31(2):805–813, January 1985.
- [62] K. H. Bevan, F. Zahid, D. Kienle, and H. Guo. First-principles analysis of the STM image heights of styrene on Si(100). *Physical Review B*, 76(4):045325, July 2007.
- [63] Qing Hua Wang, Kourosh Kalantar-Zadeh, Andras Kis, Jonathan N. Coleman, and Michael S. Strano. Electronics and optoelectronics of two-dimensional transition metal dichalcogenides. *Nature Nanotechnology*, 7(11):699–712, November 2012.
- [64] Marco Bernardi, Maurizia Palummo, and Jeffrey C. Grossman. Extraordinary Sunlight Absorption and One Nanometer Thick Photovoltaics Using Two-Dimensional Monolayer Materials. *Nano Letters*, 13(8):3664–3670, August 2013.
- [65] Wencan Jin, Po-Chun Yeh, Nader Zaki, Datong Zhang, Jerzy T. Sadowski, Abdullah Al-Mahboob, Arend M. van der Zande, Daniel A. Chenet, Jerry I. Dadap, Irving P. Herman, Peter Sutter, James Hone, and Richard M. Osgood. Direct Measurement of the Thickness-Dependent Electronic Band Structure of MoS₂ Using Angle-Resolved Photoemission Spectroscopy. *Physical Review Letters*, 111(10):106801, September 2013.
- [66] Yi Zhang, Tay-Rong Chang, Bo Zhou, Yong-Tao Cui, Hao Yan, Zhongkai Liu, Felix Schmitt, James Lee, Rob Moore, Yulin Chen, Hsin Lin, Horng-Tay Jeng, Sung-Kwan Mo, Zahid Hussain, Arun Bansil, and Zhi-Xun Shen. Direct observation of the transition from indirect to direct bandgap in atomically thin epitaxial MoSe₂. *Nature Nanotechnology*, 9(2):111–115, February 2014.
- [67] A. Rycerz, J. Tworzydło, and C. W. J. Beenakker. Valley filter and valley valve in graphene. *Nature Physics*, 3(3):172–175, March 2007.
- [68] Di Xiao, Wang Yao, and Qian Niu. Valley-Contrasting Physics in Graphene: Magnetic Moment and Topological Transport. *Physical Review Letters*, 99(23):236809, December 2007.
- [69] S. A. Wolf, D. D. Awschalom, R. A. Buhrman, J. M. Daughton, S. von Molnár, M. L. Roukes, A. Y. Chtchelkanova, and D. M. Treger. Spintronics: A Spin-Based Electronics Vision for the Future. *Science*, 294(5546):1488–1495, November 2001.

-
- [70] Igor Žutić, Jaroslav Fabian, and S. Das Sarma. Spintronics: Fundamentals and applications. *Reviews of Modern Physics*, 76(2):323–410, April 2004.
- [71] Claude Chappert, Albert Fert, and Frédéric Nguyen Van Dau. The emergence of spin electronics in data storage. *Nature Materials*, 6(11):813–823, November 2007.
- [72] Albert Fert. Nobel Lecture: Origin, development, and future of spintronics. *Reviews of Modern Physics*, 80(4):1517–1530, December 2008.
- [73] D. Gunlycke and C. T. White. Graphene Valley Filter Using a Line Defect. *Physical Review Letters*, 106(13):136806, March 2011.
- [74] Artem Pulkin and Oleg V. Yazyev. Spin- and valley-polarized transport across line defects in monolayer MoS_2 . *Physical Review B*, 93(4):041419, January 2016.
- [75] Maria O’Brien, Niall McEvoy, Damien Hanlon, Toby Hallam, Jonathan N. Coleman, and Georg S. Duesberg. Mapping of Low-Frequency Raman Modes in CVD-Grown Transition Metal Dichalcogenides: Layer Number, Stacking Orientation and Resonant Effects. *Scientific Reports*, 6:19476, January 2016.
- [76] Z. Y. Zhu, Y. C. Cheng, and U. Schwingenschlögl. Giant spin-orbit-induced spin splitting in two-dimensional transition-metal dichalcogenide semiconductors. *Physical Review B*, 84(15):153402, October 2011.
- [77] D. S. Inosov, V. B. Zabolotnyy, D. V. Evtushinsky, A. A. Kordyuk, B. Büchner, R. Follath, H. Berger, and S. V. Borisenko. Fermi surface nesting in several transition metal dichalcogenides. *New Journal of Physics*, 10(12):125027, 2008.
- [78] Hannu-Pekka Komsa, Jani Kotakoski, Simon Kurasch, Ossi Lehtinen, Ute Kaiser, and Arkady V. Krasheninnikov. Two-Dimensional Transition Metal Dichalcogenides under Electron Irradiation: Defect Production and Doping. *Physical Review Letters*, 109(3):035503, July 2012.
- [79] Yung-Chang Lin, Dumitru O. Dumcenco, Ying-Sheng Huang, and Kazu Suenaga. Atomic mechanism of the semiconducting-to-metallic phase transition in single-layered MoS_2 . *Nature Nanotechnology*, advance online publication, April 2014.
- [80] Ossi Lehtinen, Hannu-Pekka Komsa, Artem Pulkin, Michael Brian Whitwick, Ming-Wei Chen, Tibor Lehnert, Michael J. Mohn, Oleg V. Yazyev, Andras Kis, Ute Kaiser, and Arkady V. Krasheninnikov. Atomic Scale Microstructure and Properties of Se-Deficient Two-Dimensional MoSe_2 . *ACS Nano*, 9(3):3274–3283, March 2015.
- [81] Junhao Lin, Sokrates T. Pantelides, and Wu Zhou. Vacancy-Induced Formation and Growth of Inversion Domains in Transition-Metal Dichalcogenide Monolayer. *ACS Nano*, 9(5):5189–5197, May 2015.

Bibliography

- [82] Goki Eda, Takeshi Fujita, Hisato Yamaguchi, Damien Voiry, Mingwei Chen, and Manish Chhowalla. Coherent Atomic and Electronic Heterostructures of Single-Layer MoS₂. *ACS Nano*, 6(8):7311–7317, 2012.
- [83] Stanley S. Chou, Yi-Kai Huang, Jaemyung Kim, Bryan Kaehr, Brian M. Foley, Ping Lu, Conner Dykstra, Patrick E. Hopkins, C. Jeffrey Brinker, Jiaying Huang, and Vinayak P. Dravid. Controlling the Metal to Semiconductor Transition of MoS₂ and WS₂ in Solution. *Journal of the American Chemical Society*, 2015.
- [84] Peng Gao, Liping Wang, Yuyang Zhang, Yuan Huang, and Kaihui Liu. Atomic-Scale Probing of the Dynamics of Sodium Transport and Intercalation-Induced Phase Transformations in MoS₂. *ACS Nano*, September 2015.
- [85] Jun Suk Kim, Jaesu Kim, Jiong Zhao, Sungho Kim, Jin Hee Lee, Youngjo Jin, Homin Choi, Byoung Hee Moon, Jung Jun Bae, Young Hee Lee, and Seong Chu Lim. Electrical Transport Properties of Polymorphic MoS₂. *ACS Nano*, 10(8):7500–7506, August 2016.
- [86] Xuefeng Wang, Xi Shen, Zhaoxiang Wang, Richeng Yu, and Liquan Chen. Atomic-Scale Clarification of Structural Transition of MoS₂ upon Sodium Intercalation. *ACS Nano*, 8(11):11394–11400, November 2014.
- [87] Rajesh Kappera, Damien Voiry, Sibel Ebru Yalcin, Brittany Branch, Gautam Gupta, Aditya D. Mohite, and Manish Chhowalla. Phase-engineered low-resistance contacts for ultrathin MoS₂ transistors. *Nature Materials*, 13(12):1128–1134, December 2014.
- [88] Xiaofeng Qian, Junwei Liu, Liang Fu, and Ju Li. Quantum spin Hall effect in two-dimensional transition metal dichalcogenides. *Science*, 346(6215):1344–1347, December 2014.
- [89] Duk-Hyun Choe, Ha-Jun Sung, and K. J. Chang. Understanding topological phase transition in monolayer transition metal dichalcogenides. *Physical Review B*, 93(12):125109, March 2016.
- [90] Dong Hoon Keum, Suyeon Cho, Jung Ho Kim, Duk-Hyun Choe, Ha-Jun Sung, Min Kan, Haeyong Kang, Jae-Yeol Hwang, Sung Wng Kim, Heejun Yang, K. J. Chang, and Young Hee Lee. Bandgap opening in few-layered monoclinic MoTe₂. *Nature Physics*, advance online publication, May 2015.
- [91] A. Akbari, J. Knolle, I. Eremin, and R. Moessner. Quasiparticle interference in iron-based superconductors. *Physical Review B*, 82(22):224506, December 2010.
- [92] Artem Pulkun and Oleg V. Yazyev. Robustness of the quantum spin Hall insulator phase in monolayer 1t' transition metal dichalcogenides. *Journal of Electron Spectroscopy and Related Phenomena*, 2016.
- [93] John P. Perdew, Kieron Burke, and Matthias Ernzerhof. Generalized Gradient Approximation Made Simple. *Physical Review Letters*, 77(18):3865–3868, October 1996.

-
- [94] J. P. Perdew and Alex Zunger. Self-interaction correction to density-functional approximations for many-electron systems. *Physical Review B*, 23(10):5048–5079, May 1981.
- [95] John P. Perdew, Adrienn Ruzsinszky, Gábor I. Csonka, Oleg A. Vydrov, Gustavo E. Scuseria, Lucian A. Constantin, Xiaolan Zhou, and Kieron Burke. Restoring the Density-Gradient Expansion for Exchange in Solids and Surfaces. *Physical Review Letters*, 100(13):136406, April 2008.
- [96] Amirhasan Nourbakhsh, Ahmad Zubair, Redwan N. Sajjad, Amir Tavakkoli K. G., Wei Chen, Shiang Fang, Xi Ling, Jing Kong, Mildred S. Dresselhaus, Efthimios Kaxiras, Karl K. Berggren, Dimitri Antoniadis, and Tomás Palacios. MoS₂ Field-Effect Transistor with Sub-10 nm Channel Length. *Nano Letters*, November 2016.
- [97] O. Leenaerts, S. Vercauteren, B. Schoeters, and B. Partoens. System-size dependent band alignment in lateral two-dimensional heterostructures. *2D Materials*, 3(2):025012, 2016.
- [98] Qin Liu, Chao-Xing Liu, Cenke Xu, Xiao-Liang Qi, and Shou-Cheng Zhang. Magnetic Impurities on the Surface of a Topological Insulator. *Physical Review Letters*, 102(15):156603, April 2009.
- [99] T. Eelbo, M. Waśniowska, M. Sikora, M. Dobrzański, A. Kozłowski, A. Pulkin, G. Autès, I. Miotkowski, O. V. Yazyev, and R. Wiesendanger. Strong out-of-plane magnetic anisotropy of Fe adatoms on Bi_2Te_3 . *Physical Review B*, 89(10):104424, March 2014.
- [100] Gregory Mills, Hannes Jónsson, and Gregory K. Schenter. Reversible work transition state theory: application to dissociative adsorption of hydrogen. *Surface Science*, 324(2):305–337, February 1995.
- [101] Matteo Cococcioni and Stefano de Gironcoli. Linear response approach to the calculation of the effective interaction parameters in the $\text{LDA}+\text{U}$ method. *Physical Review B*, 71(3):035105, January 2005.
- [102] D. A. Abanin and D. A. Pesin. Ordering of Magnetic Impurities and Tunable Electronic Properties of Topological Insulators. *Physical Review Letters*, 106(13):136802, March 2011.
- [103] A. S. Núñez and J. Fernández-Rossier. Colossal anisotropy in diluted magnetic topological insulators. *Solid State Communications*, 152(5):403–406, March 2012.
- [104] Su-Yang Xu, Madhab Neupane, Chang Liu, Duming Zhang, Anthony Richardella, L. Andrew Wray, Nasser Alidoust, Mats Leandersson, Thiagarajan Balasubramanian, Jaime Sánchez-Barriga, Oliver Rader, Gabriel Landolt, Bartosz Slomski, Jan Hugo Dil, Jürg Osterwalder, Tay-Rong Chang, Horng-Tay Jeng, Hsin Lin, Arun Bansil, Nitin Samarth, and M. Zahid Hasan. Hedgehog spin texture and Berry’s phase tuning in a magnetic topological insulator. *Nature Physics*, 8(8):616–622, August 2012.

Bibliography

- [105] Hannu-Pekka Komsa and Arkady V. Krasheninnikov. Native defects in bulk and monolayer MoS_2 from first principles. *Physical Review B*, 91(12):125304, March 2015.
- [106] X. de la Broïse, C. Delerue, M. Lannoo, B. Grandidier, and D. Stiévenard. Theory of scanning tunneling microscopy of defects on semiconductor surfaces. *Physical Review B*, 61(3):2138–2145, January 2000.
- [107] Paolo Giannozzi, Stefano Baroni, Nicola Bonini, Matteo Calandra, Roberto Car, Carlo Cavazzoni, Davide Ceresoli, Guido L. Chiarotti, Matteo Cococcioni, Ismaila Dabo, Andrea Dal Corso, Stefano de Gironcoli, Stefano Fabris, Guido Fratesi, Ralph Gebauer, Uwe Gerstmann, Christos Gougoussis, Anton Kokalj, Michele Lazzeri, Layla Martin-Samos, Nicola Marzari, Francesco Mauri, Riccardo Mazzarello, Stefano Paolini, Alfredo Pasquarello, Lorenzo Paulatto, Carlo Sbraccia, Sandro Scandolo, Gabriele Sclauzero, Ari P. Seitsonen, Alexander Smogunov, Paolo Umari, and Renata M. Wentzcovitch. QUANTUM ESPRESSO: a modular and open-source software project for quantum simulations of materials. *Journal of Physics: Condensed Matter*, 21(39):395502, September 2009.
- [108] T. Ozaki. Variationally optimized atomic orbitals for large-scale electronic structures. *Physical Review B*, 67(15):155108, April 2003.
- [109] Graeme Henkelman, Blas P. Uberuaga, and Hannes Jónsson. A climbing image nudged elastic band method for finding saddle points and minimum energy paths. *The Journal of Chemical Physics*, 113(22):9901–9904, November 2000.

Artem Pulkin

Av. Eglise-Anglaise 14, Lausanne 1006, Switzerland
Tel: +41787273308 E-mail artem.pulkin@epfl.ch
Born 3rd August 1989

Research interests

Electronic structure of materials for applications in electronics including 2D materials, layered compounds, spin-orbit materials, topological insulators; charge carrier transport and the role of electron spin in it; density functional theory and single-particle Hamiltonians.

Education

- Ph.D. in **Physics**, École polytechnique fédérale de Lausanne, **Switzerland** 2012-2016 (expected)
- M.Sc. in **Applied Physics**, Chalmers University of Technology, **Sweden** 2010-2012
GPA 4.9 / 5.0
- B.Sc. in **Physics**, Kharkiv V.N. Karazin's State University, **Ukraine** 2006-2010
GPA: 5.0 / 5.0

Research experience

With Prof. Oleg Yazyev (EPFL)

We studied the role of the spin-orbit coupling in several novel materials including 2D transition metal dichalcogenides (TMDs). We predicted that the spin-orbit induced energy level splitting in TMDs combined with a conservation of spin and charge carrier momentum causes spin polarization of charge carriers traveling across line defects in these materials. For that, we extended the Green's function method for a ballistic transport to take into account the spin of electrons.

With Prof. Robert Shekhter and Prof. Mats Jonson (Chalmers)

We predicted the discrimination of spin in a sequential tunneling of charge carriers through a Coulomb dot interacting with ferromagnetic leads by both elastic forces and exchange interactions. We studied how spin polarization of tunneling current depends on temperature, system parameters and applied voltage using a model system of a two-level Coulomb dot interacting with large reservoirs of electrons.

Skills

Electronic structure calculations

Quantum ESPRESSO, OpenMX. Tight-binding calculations. Some experience with VASP, ELK and (Tran)Siesta.

Programming

Python (including cython and python-c interfaces), C, Java; MPI, OpenMP, Lapack in C. Documenting with Sphinx. Some experience with C++, Fortran, web technologies and frameworks: django and js. Matlab. Debugging: gdb, various profilers. Version control: git. Github account: <https://github.com/pulkin>

Publications

- Anatoli M. Kadigrobov, Robert I. Shekhter, Igor Aronov, Sergeij I. Kulinich, Artem Pulkin, Mats Jonson, Microwave-induced spin-flip scattering of electrons in point contacts, *Low Temperature Physics/Fizika Nizkikh Temperatur*, **37** (11) 925
- Robert I. Shekhter, Artem Pulkin, Mats Jonson, Spintronic mechanics of a magnetic nanoshuttle, *Phys. Rev. B* **86**, 100404(R) (2012)
- T. Eelbo, M. Waśniowska, M. Sikora, M. Dobrzański, A. Kozłowski, A. Pulkin, G. Autès, I. Miotkowski, O. V. Yazyev, and R. Wiesendanger , Strong out-of-plane magnetic anisotropy of Fe adatoms on Bi₂Te₃, *Phys. Rev. B* **89** 104424 (2014)
- Ossi Lehtinen, Hannu-Pekka Komsa, Artem Pulkin, Michael Brian Whitwick, Ming-Wei Chen, Tibor Lehnert, Michael J. Mohn, Oleg V. Yazyev, Andras Kis, Ute Kaiser, and Arkady V. Krashenninnikov, Atomic scale microstructure and properties of Se-deficient two-dimensional MoSe₂, *ACS Nano* **9** (3) 3274–3283 (2015)
- A. Pulkin, and O. V. Yazyev, Spin- and valley-polarized transport across line defects in monolayer MoS₂, *Phys. Rev. B* **93** 041419 (2016)
- A. Pulkin, and O. V. Yazyev, Robustness of the quantum spin Hall insulator phase in monolayer 1T' transition metal dichalcogenides, *J. Electron Spectrosc. Relat. Phenom.* (2016)
Publications in preparation (updated on https://scholar.google.com/citations?user=YgtJ_ggAAAAJ)
- Miguel M. Ugeda, Artem Pulkin, Yi Zhang, Ana Martín-Recio, Hyejin Ryu, Yi Chen, Feng Wang, Sung-Kwan Mo, Zhi-Xu Shen, Oleg V. Yazyev, and Michael F. Crommie, Spectroscopic evidence of the quantum spin Hall phase in single-layer 1T' WSe₂, submitted to *Nature Nanotechnology*
- A. Pulkin and O. V. Yazyev, Topologically protected states at the zigzag edges of monolayer 1T' WSe₂, in preparation
- Point defects in MoSe₂, in preparation

Awards

2006-2010 (university)

- Olympiad in Physics for University Students (supported by Ukrainian government) – several diplomas including first prize
- Youth Physicists Tournament (supported by Ukrainian government, team competition) – several diplomas of the 3rd degree
- Open Olympiad in Applied Physics held in Chernogolovka, Moscow (supported by Russian government) – first prize
- Scholarship of the Kharkiv City Mayor
- Scholarship of the Kharkiv State Governor for Gifted Youth

2003-2006 (high school)

- Olympiad in Physics for High School Students (governmental) – several diplomas including first prize
- Olympiad in Programming for High School Students (governmental) – second prize in 2005
- Several awards in all-Ukraine private team tournaments
- Several scholarships from Kharkiv State Governor to Support Gifted Youth

During the entire Bachelor studies period I have received governmental scholarship for students with excellent study results.

Teaching experience

2013-2016	EPFL	Teaching assistant at Computational physics
2015	EPFL	Teaching assistant at General physics
2014	EPFL	Teaching assistant at Differential analysis
2013	EPFL	Teaching assistant at Physics workshop course
2007-2010	Kharkiv high school 45	Teacher at Advanced physics

Volunteer project

Environmental volunteer project Vichy, France 2010

References

Oleg V. Yazyev
EPFL SB ITP GR-YAZ
PH H2 482 (Bâtiment PH)
Station 3
CH-1015 Lausanne
Switzerland
+41 21 69 35485
oleg.yazyev@epfl.ch

Frederic Mila
EPFL SB IPHYS CTMC
BSP 715 (Cubotron UNIL)
Rte de la Sorge
CH-1015 Lausanne
Switzerland
+41 21 69 30511
frederic.mila@epfl.ch

Mats Jonson
Department of Physics,
University of Gothenburg
41296 Gothenburg
Sweden
+46 31 7869157
mats.jonson@physics.gu.se